THE UNIVERSITY *of* EDINBURGH

The Behaviour of Intermolecular Interactions at Extreme Pressures

Nico Giordano

A thesis submitted in fulfilment of the requirements for the degree of Doctor of Philosophy to the School of Chemistry,

University of Edinburgh

2019

Declaration

I declare that this thesis has been composed by myself and that the work has not been submitted for any other degree or professional qualification. I confirm that the work submitted is my own, except where work which has formed part of jointly-authored publications has been included. My contribution and those of the other authors to this work have been explicitly indicated below. I confirm that appropriate credit has been given within this thesis where reference has been made to the work of others. Some work presented in Chapter 1 was previously published in ref. 1, co-authored by Laura J. McCormick, Simon J. Teat and Christine M. Beavers. This study was conceived by all of the authors. I carried out reviews of the literature in conjunction with the other authors.

The work presented in Chapter 2 was previously published in ref. 2, co-authored by Christine M. Beavers, Konstantin V. Kamenev, William G. Marshall, Stephen A. Moggach, Simon D. Patterson, Simon J. Teat, John E. Warren, Peter A. Wood and Simon Parsons. I carried out recrystallisations and the single-crystal X-ray diffraction experiments; including all data processing and structural refinements. I performed the DFT, PIXEL and SAPT energy calculations. Powder neutron diffraction and 'low-pressure' X-ray diffraction measurements performed at the Synchrotron Radiation Source were done by previous group members Peter A. Wood and Simon Patterson. I was responsible for the analysis and interpretation of all the results presented.

The work presented in Chapter 3 was previously published as ref. 3, co-authored by Sergejs Afanasjevs, Christine M. Beavers, Claire L. Hobday, Konstantin V. Kamenev, Earl F. O'Bannon, Javier Ruiz-Fuertes, Simon J. Teat, Rafael Valiente and Simon Parsons. I carried out sample recrystallisations and all single-crystal X-ray diffraction experiments. I performed the DFT, PIXEL and SAPT energy calculations. UV-Vis spectroscopy and electrical resistance measurements were performed by Javier Ruiz-Fuertes and Sergejs Afanasjevs. Band structure calculations were performed by Claire L. Hobday. Raman

spectroscopic measurements were performed by Earl O'Bannon. I was responsible for the analysis and interpretation of all the results presented.

The work presented in Chapter 4 will be submitted for publication; co-authored by Christine M. Beavers, Branton J. Campbell, Václav Eigner, Eugene Gregoryanz, William G. Marshall, Miriam Peña Alvarez, Simon J. Teat, Cara E. Vennari and Simon Parsons. I carried out recrystallisations and the single-crystal X-ray diffraction experiments; including all data processing and structural refinements. I performed the DFT, PIXEL and SAPT energy calculations. Symmetry analysis was done by Branton J. Campbell. The recrystallisation from methanol was done by Václav Eigner. Neutron experiments were done by William G. Marshall and Simon Parsons. Raman measurements were done by Cara E. Vennari and Miriam Peña Alvarez. I was responsible for the analysis and interpretation of all the results presented.

The sample used for the work in Chapter 5 was prepared by James R. Pankhurst, but I was responsible for recrystallisations and all measurements, analysis and interpretation. When published the work will be co-authored with Christine M. Beavers, Jason B. Love, James R. Pankhurst, Simon J. Teat and Simon Parsons.

Nico Giordano

List of Publications

1. McCormick, L. J.; Giordano, N.; Teat, S. J.; Beavers, C. M., Chemical Crystallography at the Advanced Light Source. Crystals 2017, 7 (12), 382.

2. Giordano, N.; Beavers, C. M.; Kamenev, K. V.; Marshall, W. G.; Moggach, S. A.; Patterson, S. D.; Teat, S. J.; Warren, J. E.; Wood, P. A.; Parsons, S., High-pressure polymorphism in l-threonine between ambient pressure and 22 GPa. CrystEngComm 2019, **21** (30), 4444-4456.

3. Giordano, N.; Afanasjevs, S.; Beavers, C. M.; Hobday, C. L.; Kamenev, K. V.; O'Bannon, E. F.; Ruiz-Fuertes, J.; Teat, S. J.; Valiente, R.; Parsons, S., The Effect of Pressure on Halogen Bonding in 4-Iodobenzonitrile. Molecules 2019, 24 (10), 2018.

Abstract

In organic solids, pressures of only a few gigapascals modify and rearrange intermolecular contacts such as H-bonds and van der Waals contacts leading to extensive phase diversity. Applications in this rich area of research include searches for new phases and solvates of pharmaceutical materials; modelling of detonation mechanisms of energetic materials, and modelling of the driving forces of phase transitions. The overarching theme of this PhD thesis is to obtain new, often difficult to isolate, high-pressure polymorphs of small molecules and elucidate the role of intermolecular interactions in their phase stabilities.

The need to obtain precise structural information at atomic resolution demands the use of single crystal diffraction methods but scattering intensities are typically low, and the pressure apparatus used in these studies (the diamond anvil cell) results in incomplete data. This can make direct structure determinations for some materials difficult or even impossible. Third generation synchrotron X-ray sources are therefore used for their brightness, high energies, and small focused beams to extract as much structural information from samples as possible.

The amino acid L-threonine, characterised by its hydrogen bond network, has been structurally characterised at 22 GPa which is an unusually high-pressure for a complex organic molecule. L-threonine undergoes two isosymmetric phase transitions at *ca.* 2 and *ca.* 9 GPa, and a phase transition at *ca.* 18 GPa that results in a loss of crystal symmetry. Structures of L-threonine were determined by single-crystal X-ray diffraction to 22 GPa; which is the highest-pressure structure ever reported for an amino acid. High-pressure polymorphism in pyridine was studied extensively by single-crystal X-ray diffraction, Raman spectroscopy and neutron powder diffraction. Pyridine has at least three polymorphs in the narrow pressure range of *ca.* 1 to *ca.* 2 GPa but the sluggish nature of the phase transitions has made isolating and characterising one of the phases difficult, until now. Here, we used *in situ* crystal

growth in the diamond anvil cell to obtain a stable, diffraction quality single crystal of the elusive phase III and determined its crystal structure for the first time. A mechanism for the transformation is also proposed. The halogen bonded molecule, 4-iodobenzonitrile was studied experimentally by single-crystal X-ray diffraction and Raman spectroscopy up to 10 GPa. 4-iodobenzonitrile undergoes a reconstructive phase change above 5 GPa that results in crystals breaking apart, making it difficult to obtain meaningful diffraction data. Nevertheless, the structure of the new high-pressure phase was determined for the first time by rapidly pressurising a crystal grown *in situ* to 8 GPa. Crystal lattice and intermolecular PIXEL energy calculations have been validated for use with small organics to 22 GPa, as well as for halogen containing molecules at very high pressures; allowing the roles of stabilising, or destabilising, molecular interactions to be probed in high-pressure polymorphs for a range of organic molecules.

Finally, a neon co-crystal was obtained on compression of a Cu_2 Pacman complex. This single-crystal structure represents one of only a few published neon containing organometallic structures. Neon resides within the interstitial voids as a result of the Pacman complex reconfiguring to allow neon-uptake. The study shows the interplay between the pressure transmitting medium and crystal structure and we discuss the potential applications of pressure mediated guest-uptake in the Pacman complexes.

Lay Summary

In the solid state, molecules pack together in a highly ordered fashion to form crystals. These crystals are held together by intermolecular interactions. Ice for example is an agglomeration of water molecules held together by intermolecular interactions known as hydrogen bonds, which dictate physical properties such as boiling and melting points. The transformation from one phase *e.g.* liquid water to ice water is the manifestation of ordering of the molecules by hydrogen bonds at low temperatures or high pressures.

The idea of phase transitions can be further extended to just solids so that the arrangement of molecules in the crystal can change and a solid can exist in more than one solid form, a phenomenon that may have economical or safety implications. For example, an active pharmaceutical ingredient (API) may be beneficial in one crystal form but completely useless in another, or an explosive powder might transform to a much more sensitive form during storage and detonate.

The interactions that hold the crystal together dictate the structure stability and it is possible to alter these interactions by subjecting the crystal to high pressure and induce solid-solid phase transitions. We can study the phase transition in terms of the intermolecular interactions by crystallography and deduce structure-property relationships. The hydrogen bond can be found throughout nature *e.g.* in protein molecules and might be exploited in APIs to target specific cells in the treatment of diseases. The hydrogen bond interactions are well characterised within a limited pressure range, but at what point does the nature of the bonding change? We examine the hydrogen bond and other non-bonding interactions, as we seek to understand how intermolecular interactions change at pressure extremes with the aim of gaining insights into the mechanisms of phase transitions.

Acknowledgements

First, I would like to thank my supervisor, Professor Simon Parsons. Thank you for taking me on as a PhD student and allowing me all the incredible opportunities that go with it. Thank you for all your help and support over the course of my studies.

To everyone in Edinburgh, past and present, who has helped me along the way: Stephen, Claire, Charlie, Chris, Gary, Scott, Matt, Jonny, Jacob, Helen, Giulia, Václav, Ed and Yuka, thank you.

To everyone in California who made my time there so enjoyable and rewarding. Simon, thank you for having me on your beamline, you taught me a lot about crystallography and synchrotrons, but maybe even more about Pokémon. Christine, although not officially my supervisor, you took me under your high-pressure wing and mentored me through all aspects of beamtime and data-collection and everything else high-pressure science, thank you. To Camelia and Earl, thank you for your mentorship and friendship in and out of the lab. Thanks for the weekly dinners and catch-ups with the Vanderpumps. To everyone else at The Advanced Light Source, especially Laura, Andy and Martin for your help on the beamlines. And to everyone who made my downtime 'hella dope,' Cara, Rana, Teresa and the Berkeley Lab Postdoc Association. Thank you all for the great times.

To Jenny, thank you for everything cat and house related. Mum, Dad, Caterina and Maria, thank you for everything you have done to help me along the way.

Table of Contents

Chapter 1

Introduction

1.1. Introduction

1.1.1. High-Pressure Background

What constitutes 'extreme' or 'high' pressure is largely discipline dependent. In Geophysics, high-pressure refers to deep Earth conditions which range from tens of gigapascals (GPa) in Earth's lower mantle to *ca.* 360 GPa at the inner core.* These studies may be concerned with the formation of deep-Earth minerals or even water or carbon transport mechanisms.[1-2]

Conversely, high-pressure in Biology is typically in the order of 0.1 GPa, which is the highest known pressure at which living organisms, barophiles, have been observed in deep ocean trenches.[3] In fact, some organisms including the terrestrial tardigrade ("water bears") which are small animals, and *Artemia* cysts (dormant Brine Shrimp eggs) have even been shown to survive exposure to pressures up to 7.5 GPa in the laboratory, giving credence to the theory of interplanetary transport of organisms by meteors.[4]

In organic crystal structures, and the focus of this thesis, moderate pressures (< 10 GPa) are often suitable for investigating a plethora of exotic or interesting behaviour such as phase transitions, conformational changes; or changes in electrical, optical, or mechanical properties.[5] While structural studies of relatively complex organic molecules at higher-pressures (> 10 GPa), is still largely unexplored territory, which will be addressed in Chapter 2. Underpinning all high-pressure studies is the way in which strain is manifested in molecular packing, which can be used to elucidate structure-property relationships. This thesis aims to explore the role of different intermolecular interactions in determining structural stability under high-pressure conditions.[5-9]

*For scale, standard atmospheric pressure (1 atm) is equal to 101325 Pa, or roughly 1 bar, and 1 GPa = 10 kbar.

1.1.2. High-Pressure Polymorphism

Polymorphism refers to the ability of a compound to pack in different manners. The ways in which molecules pack can result in hugely different physical properties, *e.g*. the carbon allotropes, diamond and graphite completely differ in appearance and strength. The concept of polymorphism has far reaching consequences in a range of materials, for example; the explosive, ammonium nitrate transforms between forms IV and III at only 32 °C resulting in a more sensitive material that is prone to accidental detonation.[10] Inks and dyes may exhibit different colours,[11] or the electronic properties of organic semiconductors can be dramatically altered depending on the polymorph.[12] It is especially important in areas such as pharmaceutical science, where one form of an active pharmaceutical ingredient (API) is bioavailable and therapeutic, while another form may be less potent or non-effective. Ritonavir, a treatment for HIV/AIDS, is one famous example where the drug delivered to market transformed to a non-effective, more thermodynamically stable crystal form that had to be withdrawn at an estimated cost of $250 million to the manufacturer.[13] The need to understand polymorph behaviour and the driving forces of phase transformations then becomes apparent. Crystal packing in organic molecules has been the focus of much research in crystal engineering and crystal structure predictions over the past two decades as scientists across the disciplines seek to control or predict specific crystal forms with desirable properties.[14-15]

A crystal will undergo a phase transition to a more thermodynamically stable form when thermodynamic conditions are altered and a lower Gibbs free energy (G) is obtained. G is defined as:

$$G = U + PV - TS = H - TS \quad (1)$$

where H is the enthalpy, and T and S are the temperature and entropy of the system. The internal energy of the system is given by, U; and P and V are the pressure and volume. The free energies are difficult to calculate and it is typical to rely on calculated relative lattice enthalpies of polymorphs to rationalise phase transitions in thermodynamic terms.[16] In crystalline solids at high-pressure, the pressure-volume contributions dominate the free energy. A small increase in pressure can lead to a large change in the total energy. The pressure-volume contribution to the free energy can be estimated in units of kJ mol^{-1} by:

$$E_{PV} = 0.6 \cdot (P\Delta V) \qquad (2)$$

where pressure is in GPa, ΔV is the difference in unit cell volumes in Å^3 and the constant, 0.6, is derived from Avogadro's number. The $T\Delta S$ term is assumed to be negligible at high-pressure as the vibrational frequencies tend to shift to higher frequencies as atoms move into close proximity. However, it can still be the dominating term in determining polymorph stabilities, as in the case of the formation of salicylamide-II at 0.2 GPa. Where the $T\Delta S$ contribution is 3 kJ mol^{-1} *vs.* a 1 kJ mol^{-1} contribution from the $P\Delta V$ term.[17] The U term is the last of the contributions to Gibbs free energy and includes contributions from intermolecular interactions (intramolecular bond energies make up the rest of the contribution) and so, understanding the evolution of both volume and the cohesive forces to the total crystal lattice energies becomes apparent in elucidating phase behaviour. The difference in crystal lattice energies between most polymorphs is less than 2 kJ mol^{-1}. [18] It is unsurprising then, that even small perturbations induced by high-pressures are enough to cause phase transitions.

However, it should be noted that relying entirely on the thermodynamic model is not a reliable measure of phase behaviour at high-pressure as other factors such as, choice of hydrostatic medium, growth kinetics, and nucleation

need to be considered.[19] Differing compression rates of L-serine for example produces different polymorphs,[20] and decompression may lead to the formation of phases not encountered on compression, as seen in cysteine and ζ-glycine for example.[21-22]

Conformational changes abound on compression as molecules move to accommodate more stable packing arrangements, *i.e.* increasing the packing density to reduce the molecular volume (minimisation of the *PV* contribution). A contact may compress until a lower limit is reached, H···H distances for example have a lower limit of compression of 1.7 Å.[23] As interactions approach these critical limits phase transitions result as the short contacts move to relieve repulsion effects. It may be possible then to predict when a phase transition will occur. Phase transitions may be displacive or reconstructive in nature. Displacive transitions are characterised as having group-subgroup relationships with only small changes in atomic positions between the phases.[24] Conversely, reconstructive transitions, are characterised by bonds breaking and reforming, and often lack any group-subgroup relationship.[25] Transitions may occur as single-crystal to single-crystal; single-crystal to polycrystalline powder; powder to powder transformations, or even as complete amorphisation events.

1.1.3. Examples of High-Pressure Polymorphism

The crystal structure of salicylaldoxime, an industrially important sequestering compound, has been investigated under high pressure and was found to undergo a phase transition between 5.3 and 5.9 GPa. Molecules are linked in pairs by OH···O hydrogen bonds and stack by π···π interactions forming pseudo-macrocyclic cavities which close-up on compression. The phase transition was found to be driven partly by the relief of intermolecular repulsions in the OH···O and π···π dimer pairs. An OH···N interaction is replaced by an OH···O interaction as a more favourable packing arrangement is adopted in the high-pressure phase.[26]

The antidiabetic drug, chlorpropamide undergoes a reversible phase transition from the orthorhombic ambient pressure phase ($P2_12_12_1$) to a monoclinic ($P2_111$) phase at *ca.* 2.8 GPa. The hydrogen bond network persists between phases, although hydrogen-bond lengths increase slightly. Changes in the other intermolecular interactions are more pronounced resulting in conformational changes which accommodates better packing.[27]

Toluene has four known polymorphs, the first two, I and II are obtained on cooling the liquid to 105 and 165 K, and the other two forms, III and IV are obtained from high-pressure *in situ* crystallisation techniques. The high-pressure polymorphs pack in three dimensions by CH···π interactions which differs from the two-dimensional sheet topology formed in the ambient pressure phases (I and II).[28]

Some high-pressure polymorphs are stable enough to be recovered at ambient pressure, and in organic crystals, used as seeds in ambient pressure crystallisations. For example, a single crystal of the monohydrate form of the neurotransmitter γ-amino butyric acid has been obtained and recovered from high-pressure (0.4–0.8 GPa) and used as a seed in ambient pressure crystallisations. In the absence of the recovered high-pressure polymorph, recrystallisations produced only the anhydrous form.[29] This approach may be appealing in batch scale-up processes in industry where large product volumes of a specific polymorph are required.

The molecular complex tris(μ_2-3,5-diisopropyl-1,2,4-triazolato-$\kappa_2N^1:N^2$)trigold(I) exhibits four successive phase transitions (all reversible) to the modest pressure of 3 GPa, with the ambient pressure phase re-emerging at high pressure, a rare phenomenon in molecular materials. The first two phase transitions are driven by a reduction in volume, while the third phase transition yields the ambient pressure phase and occurs from structural distortions about aurophilic interactions. The driving force of the final transition is rationalised as volume reduction by the authors.[30]

The compression of molecular solids has been widely studied, at least to 10 GPa, and some common features in the compression mechanisms are apparent.[31] Compression proceeds in an anisotropic manner and favours closing of voids. While compression of long-intermolecular contacts is preferred over short contacts. Kaźmierczak and Katrusiak show that the strongest interactions tend to persist on phase transformations, even at high pressure.[32-33] Most intermolecular bond lengths have been shown to shorten on compression to 10 GPa but do not decrease below distances found in similar interactions in ambient-pressure structures.[16, 26] The associated changes in both crystal lattice and intermolecular energies can be followed by computational approaches, such as PIXEL (see Section 1.5) or density functional theory (DFT) to rationalise any changes observed in packing on compression.

1.1.4. Applications of High-Pressure in Other Research Areas

In organic molecules, primary bonds are generally regarded as incompressible to at least to 10 GPa while the intermolecular interactions governing packing, and molecular torsions, are sensitive to pressure. In metal complexes however, structural responses to pressure are not so easily defined and modifications in primary bonding can occur giving rise to a host of tuneable properties. For example, changes in metal-ligand distances; formation of bridging ligands; and modification of spin states or even coordination number.[34] Changes in metal-ligand bonding occur in $[UN''_2]_2(\mu\text{-}\eta^6\text{:}\eta^6\text{-}C_6H_6)$ ($N''=N(SiMe_3)_2$) at 3.2 GPa as agostic interactions form between -CH and the uranium centre.[35] Similarly, pressure induces a phase transition in the mononuclear macrocycle, *cis*-$[PdCl_2$(1,4,7-trithiacyclo-nonane)] at 0.44 GPa as polymer chains form by new metal–ligand interactions.[36]

Spin-crossover (SCO) events can be initiated by pressure, but also by temperature, irradiation or exposure to a magnetic field. SCO can result in drastic variations in a material's structure, conductivity or magnetic properties.

Pressure-induced SCO occurs at *ca.* 1 GPa in [FeL1] $(ClO_4)_2$(Ll=2,6-bis[3-methylpyrazol-1-yl]-pyrazine).[37] The high-spin to low-spin transition is accompanied by a complete ordering of the perchlorate counter ions. In $Fe^{II}(Metz)_6(Fe^{III}Br_4)_2$ (Metz=methyltetrazole) pressure induces full SCO and magnetic ordering at ambient temperature.[38] Pressure is therefore seen to be a useful tool in the search for new multifunctional materials.

In materials science, the study of metal-organic-frameworks (MOFs) is of great interest due to their applications in gas storage and catalysis. Pressure has been used to activate otherwise unreactive materials. In the MOF, zeolitic imidazolate framework-8 (ZIF-8), pressure causes solvent uptake by direct force at 0.18 GPa and then again at 1.47 GPa as the result of a phase transition that results in an increase in the pore sizes and solvent accessible volume.[39] MOFs are typically flexible materials and some of them can expand on compression, a rare and extraordinary phenomenon known as negative linear compressibility (NLC). Zinc alkyl gate-4 (ZAG-4) shows reversible NLC to 9 GPa,[40] but some classes of small molecules, such as the metallocyanides, also exhibit NLC. For example, $(C_6F_5Au)_2$ (μ-1,4,-diisocyanobenzene) exhibits NLC to 4 GPa.[41] Nevertheless, the largest NLC behaviour is exhibited in the framework materials. ZAG-6 exhibits NLC and undergoes a bond rearrangement on compression. Pressure also induces a reversible proton transfer between solvent water molecules and the phosphonate group of the metal-organic-framework.[42]

Our understanding of the fundamental properties of matter is challenged under pressure. Lithium, the lightest alkali metal behaves as a nearly free-electron metal at ambient conditions, but the system symmetry breaks at pressures of 80 GPa and causes the metals to transform to a semiconductor.[43] Yet, further compression leads to another transformation back to a metal at 120 GPa and the free-electron model breaksdown.[44] Pressure has also been used to synthesise novel van der Waals compounds from otherwise unreactive starting materials. Xenon, is closed shell and generally regarded as unreactive, yet it forms a metallic-like compound with molecules of nitrogen, $Xe(N_2)_2$, at

the modest pressure of 5 GPa at 300 K.[45] Similarly, Xe has also been shown to form mixtures with H_2 at pressures as low as 4.2 GPa at 300 K.[46] Another xenon compound, XeF_2, has been studied by powder X-ray diffraction and computational methods and is shown to be pressure stable to 28 GPa, where it undergoes a phase transition, with another occurring at 59 GPa; full metallisation of the compound is predicted to occur at 152 GPa.[47]

1.2. The High-Pressure Experiment

1.2.1. The Diamond-Anvil Cell

Diamond-anvil cells have been widely used for over half a century to generate static high-pressures in a multitude of sample types and environments. They come in various shapes and sizes, depending on the experimental needs. Bassett gives a comprehensive review of the history, evolution and applications of the diamond-anvil cell in the literature.[48] Briefly, its invention is credited to Weir, Lippincott, Van Valkenburg and Bunting,[49] who based their design on the earlier works of P.W. Bridgman, the winner of the Nobel Prize in Physics in 1946, for his invention of "an apparatus to produce extremely high pressures, and for discoveries he made therewith in the field of high pressure physics." [50] Diamonds were chosen as anvils by Weir *et al.* for their transparency to a wide range of the electromagnetic spectrum; single-crystal nature and their high strength, which differs from Bridgman's WC-anvil design, producing higher pressures with optical access to the sample *in situ*. Diamond anvil cells can generate static high pressures into the megabar range depending on design and are suitable for a range of techniques, for example: infrared, Raman, Mossbauer, and X-ray spectroscopies; single crystal and powder diffraction methods; and magnetic measurements.[51-52] Of course, the accessible pressure range and experimental application is dictated by the type of DAC and diamonds used, and experimental aims should be considered prior to experimentation.[53-54]

Merrill-Bassett and BX90 type DACs were used in this thesis, [55-56] and are shown in **Figure 1.1**. In both designs, force is applied to the opposing anvils by screws, and pressure is generated about the flat-faces (culets) of the diamonds. The diamonds are separated by a hard gasketing material such as tungsten or rhenium, which supports the anvils and comprises the cylindrical sample chamber that contains the solid sample of interest in a hydrostatic pressure transmitting medium (PTM). Pressure is transmitted isotropically to the sample from the anvils and gasket by the PTM. The backing seats that contain the diamonds are conically cut to accommodate Boehler–Almax diamonds which are wedged into the backing seats. This set up provides additional support to the anvils while allowing a wider angular access to the sample chamber than other typical cell geometries.[57] Such considerations are vital for successful high-pressure diffraction experiments, as the cell opening dictates the limiting angle of diffraction and accessible reciprocal-space volume. The backing seats are typically made from tungsten carbide, or cubic boron nitride (*c*-BN) for their strength. *c*-BN seats have the advantage of being transparent to the high-energy X-rays typically used in X-ray diffraction studies at synchrotron facilities.

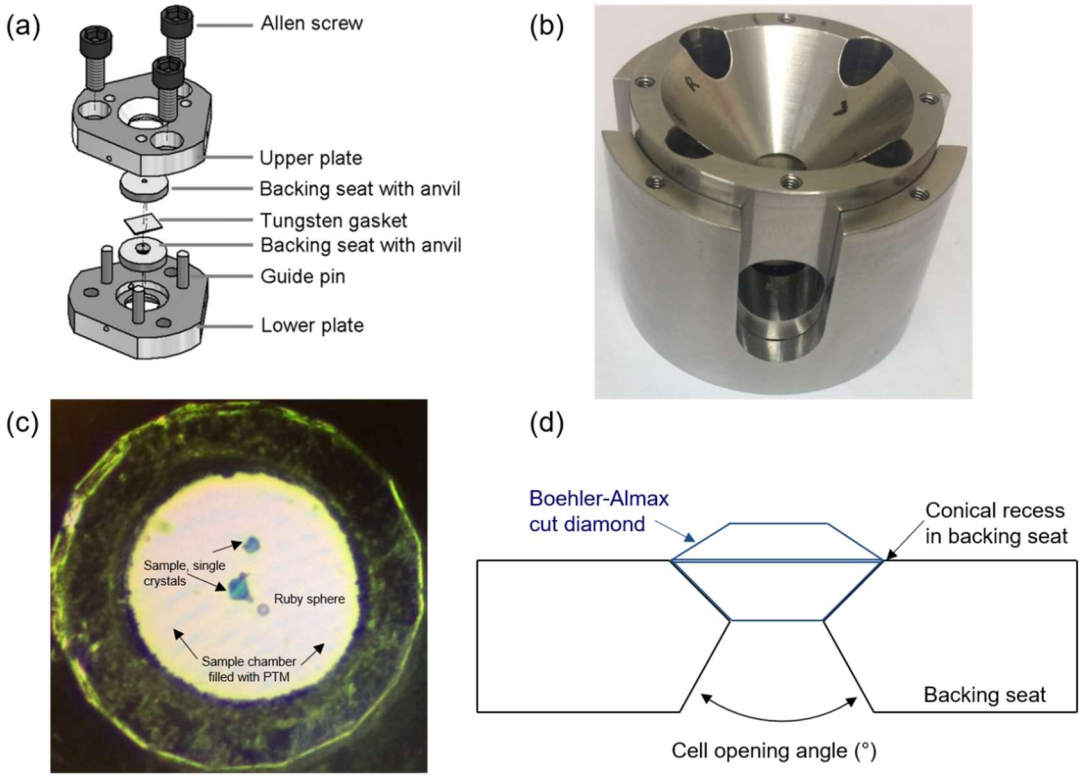

Figure 1.1 The high-pressure experiment: (a) schematic of the Merrill-Bassett cell,[57] (b) BX90 cell, (c) axial view of the sample chamber, and (d) schematic of the Boehler-Almax cut diamond wedged into the backing seat.

1.2.2. Merrill–Basset Cell

The Merrill–Bassett cells comprise two metal plates containing the anvils that are pushed together by three screws, with a cell opening angle of 80°.[55] The Merrill–Basset cells are small, and easily accommodated by most lab-source diffractometers. However, shading from the body of the DAC results in incomplete data collections. Therefore, optimised collection strategies, such as that of Dawson *et al.*[58] must be used to maximise the quality and quantity of data collected, while avoiding instrument collisions.

1.2.3. BX90 Cell

The BX90 type DAC provides enhanced stability over the Merrill-Bassett cell due to its piston design.[56] The loading force is applied in a smooth and accurate manner by four screws contained within packed, conical spring washers. Such a set up helps prevent sudden pressure changes, which can result in experimental failure. The cell features a wider opening angle, 90°, than the Merrill-Bassett design (80°), as well as side-openings available for resistivity measurements or radial diffraction experiments. Although the BX90 cell is larger than the Merrill-Bassett, it is small enough (ø=50 mm, thickness= *ca.* 35 mm) that it can be accommodated on most synchrotron beamlines with appropriate cell mounts. However, its bulky size and weight precludes the cell from use on standard lab source diffractometers. The BX90 was used here for the ease in which it can be gas loaded in a compressed gas gas-loader system, and data collected using synchrotron facilities. Data collection methods and strategies varied in each chapter and are detailed therein.

1.2.4. Gas-Loading

It is necessary to load samples in a suitable pressure transmitting medium to reduce anisotropic stress on the sample. This can be a solid, liquid or gas. Common PTM have been well characterised and ranked in detail,[59-61] with some common examples given in **Table 1.1**.

The preferred media for high-pressure experiments (> 10 GPa) are the noble gases helium and neon because they exhibit low shear strengths well beyond their freezing pressures at 12.1 and 4.8 GPa and have been shown to provide nearly hydrostatic conditions to 80 GPa when used to compress hard solids like iron.[61] Further to their improved hydrostaticity over other conventional media such as liquid alcohol mixtures, the noble gases are advantageous for their low X-ray scattering backgrounds and chemical inertness.

Table 1.1 Hydrostatic compression limits of common pressure transmitting media.[59]

Pressure Transmitting Medium	Freezing Pressure at 300 K (GPa)	Hydrostatic Limit (GPa)
1:1 iso-*n*-pentane	7.4	7.4
4:1 methanol-ethanol	10.5	10.5
Silicone Oil	2.5	2.5
Argon	1.4	10
Nitrogen	2.4	10
Neon	4.8	15
Helium	12.1	23

One major disadvantage of using helium, however, is that it can cause diamond embrittlement in high-temperature studies, whereby helium percolates in the bulk diamond structure through defects and breaks the diamond. This behaviour is observed at pressures as low as 20 GPa,[62] therefore, larger rare gases such as neon may be preferred in moderate pressure studies.

Gas-loading can be achieved by cryoloading or using compressed gas methods. Cryoloading involves cooling the DAC to liquid nitrogen temperatures (77 K) and flooding the cryo chamber containing the DAC with a liquefied gas, such as O_2, N_2 or Ar. In high-pressure gas-loading methods, the DAC is contained in a pressure vessel in a purpose-built gas-loader and filled with liquefied gas at *ca.* 200 MPa. The cell is then remotely closed by motorised rotary feedthroughs, trapping the liquefied gas within the DAC sample chamber. The pressure vessel is then purged, and the DAC removed, ready for experimentation.

Loading with He or Ne can be problematic if the sample chamber is not efficiently filled with the condensed gas. The gasket is prone to shrinkage on pressurisation of the DAC because of the high compressibilities of the gas media. The shrunk gasket reduces the available scattering geometry, or worse, crushes the sample. Small sample sizes and large initial gasket holes are therefore necessary to offset these problems. Compressed gas-loading methods are preferred over cryoloading because they are more readily controlled by the gas-loading system, and samples are unlikely to be washed away.

1.2.5. Pressure Determination

The internal pressure of the DAC is commonly measured by the ruby fluorescence method.[63] A small chip of ruby, or synthetic ruby spheres, are placed inside the cell alongside the sample. Ruby (Al_2O_3:Cr^{3+}) is irradiated with green or blue laser light which excites Cr^{3+} impurities into an excited state giving

rise to a ruby doublet (R1, R2) in the fluorescence spectrum at *ca.* 694.3 nm. Increasing the pressure results in a shift of the doublet to lower energies and pressure is measured with respect to the shift in the R1 peak. The R1 shift is calibrated against known pressure standards, Cu, Mo, and Pd, which provides an accurate measurement of the internal pressure.[63] Peak broadening or merging; or variations in the peak shift, may be observed due to temperature fluctuations and non-hydrostatic stresses. When these errors are accounted for, the ruby fluorescence method is still regarded as sufficiently accurate (±1 % of the wavelength shift) and thus the preferred method for determining pressures in most high-pressure studies; it has been calibrated for use to 2.5 Mbar.[64] Pressure can also be calculated from unit cell volumes obtained from diffraction measurements.

The change in volume (V) of a material is dependent on its resistance to hydrostatic pressure (P) at a constant temperature (T), which is defined as its bulk modulus (K) (see Equation 3). If K and V of a material are known, they can be fitted to its equation-of-state (EoS), such as the third-order Birch-Murnaghan (Equation 4),[65] to determine its pressure.

$$K = -V\left(\frac{\partial P}{\partial V}\right)_T \tag{3}$$

$$P(V) = \frac{3}{2}K_0\left[\left(\frac{V_0}{V}\right)^{\frac{7}{3}} - \left(\frac{V_0}{V}\right)^{\frac{5}{3}}\right]\left\{1+\frac{3}{4}\left(K_0^{'}-4\right)\left[\left(\frac{V_0^{\frac{2}{3}}}{V}-1\right)\right]\right\} \tag{4}$$

K' is the pressure derivative of the bulk modulus and is a measure of a material's compressibility and subscript *0* denotes values at ambient pressure. Inclusion of a well-characterised material, such as NaCl,[66] as an internal standard for pressure determination in diffraction experiments is therefore common practice. This method is useful when there is no optical access, *e.g.* in

a Paris-Edinburgh cell, and it is occasionally possible to use the PTM or gasket itself as a pressure marker.[67]

Both the ruby fluorescence method and diffraction methods have been used in this thesis to measure internal pressures.

1.3. Synchrotron Radiation Sources

Synchrotrons are particle accelerators capable of producing high-intensity X-rays with multiple orders of magnitude greater flux (100 billion times brighter) than those from an X-ray tube source. Synchrotrons offer tuneable wavelengths (from IR to X-rays), a low divergent beam, small beam sizes and access to specialist equipment, *e.g.* gas-loading apparatus, which make them appealing resources in overcoming some of the limitations of the high-pressure diffraction experiment, such as weak scattering or limited resolution.[52, 68]

Prior to X-rays being harvested from the storage ring for experiment, electrons must be generated and accelerated to their final energy. Electrons are generated by an electron gun which comprises a metal plate that is heated in a vacuum causing the loss of electrons at its surface. Electrons are then emitted by the application of a positive electric field near the surface. As electrons are emitted towards the anode, some of them pass through an aperture towards the linear accelerator (linac). The linac then accelerates the electrons to 99.99997 % the speed of light by oscillating electric potentials along a linear path. Concurrently the electrons are focussed by quadrupole electromagnets. The energies of the accelerated electrons range from a few hundreds of MeV to the full energy of the storage ring. Most synchrotrons do not operate the linac at the full energy of the storage ring. Instead, the accelerated electrons are fed into a booster ring which accelerates the particle beam further, and the energy increases from *ca.* 0.3 to 3–6 GeV. The booster ring also serves to reduce emittance of the electrons and improve the efficiency of injection into the

storage ring as the acceptance limit is small. The electrons pass through radio frequency (RF) cavities in the booster ring that cause the electrons to accelerate which results in bunching. The electron bunches are separated by a short time delay in the order a few of nanoseconds, depending on the harmonic number of the RF moderator which is largely synchrotron dependent.[69] For example, The Advanced Light Source (ALS) consists of a booster synchrotron which generates electrons up to 1.9 GeV (beam current, 500 mA)[70] a modest energy compared to other large facilities, such as Diamond, 3 GeV (beam current, 300 mA),[71] or PETRA III, 6 GeV (beam current 100 mA).[72]

The electrons are then fed periodically into the storage ring which serves to store the beam and replenish energy lost to radiation. The storage ring comprises a series of straight and curved sections.

Bending magnets situated at the curved section send electrons into their circular orbit but the change in direction of the electron bunch results in the emission of electromagnetic radiation tangential to the electron orbit. The emitted electromagnetic radiation, which varies in wavelength from IR to X-ray depending on the strength of the magnetic field and synchrotron energy, can then be harvested by beamlines for experimentation. Meanwhile, the electrons continue in their circular orbit in the storage ring through straight sections that comprise a series of magnets (*e.g.* quadrupole and sextupole magnets) which focus and direct the electrons so that they remain in their ideal orbit. In third generation synchrotrons, such as the ALS, Diamond and PETRA III, insertion devices are also present in the straight sections. The insertion device is an array of small magnets (undulator or wiggler) that force electrons to follow an oscillating trajectory and emit radiation at each bend. Radiation generated at each bend overlaps and interferes to generate a fine beam of very intense (brilliant), directional X-rays. The emitted radiation is concentrated at the fundamental and harmonic energies and can be fine-tuned by changing the spacing between the magnets. The resultant X-rays produced by insertion devices are much more brilliant those of bending magnets and can also be

directed to beamlines. RF cavities present in the storage ring, like in the booster ring, act to replenish energy lost in the form of electromagnetic radiation at each turn.

1.3.1. Synchrotron Sources in High-Pressure Crystallography[68]

Synchrotrons offer advantages over typical lab sources, mainly, for their increased flux, this is especially important in high pressure diffraction experiments that typically use small and weakly diffracting crystals. The relative scattering power of a crystal (S) can be estimated by the following equation:

$$S = \left(\frac{F_{000}}{V_{cell}}\right)^2 V_{crystal}\,\lambda^3 \tag{5}$$

where: F_{000}=number of electrons per unit cell. V=volume, and λ= wavelength.[73] Equation 5 is modified to give an approximation of the crystal's ability to diffract (I_{diff}) with respect to varying incident intensity (I_{inc})[74]:

$$I_{diff} \approx \lambda^3 L I_{inc} F_{000}^2 \frac{V_{crystal}}{V_{cell}^2} \tag{6}$$

where the Lorentz correction (L) is approximately proportional to 1/λ, and the approximation of the diffracted intensity simplifies to:

$$I_{diff} \approx \lambda^2 I_{inc} F_{000}^2 \frac{V_{crystal}}{V_{cell}^2} \tag{7}$$

The diffracted intensity is therefore approximately proportional to the wavelength squared; thus, it is advantageous to use higher wavelength X-rays on weakly diffracting samples. For example, a Cu-Kα source (λ=1.5418 Å) is preferred over Mo-Kα (λ=0.7107 Å) on a lab source for the improved diffracted intensities, however, absorption effects also increase with increased wavelength, and absorption from the diamonds render this approach difficult or impossible in high-pressure diffraction experiments. Therefore, improvements to I_{diff} are readily exploited by synchrotron sources for their multiple orders of magnitude increase in X-ray flux as $I_{diff} \propto I_{inc}$. This feature also makes synchrotrons appealing for large molecules such as the metal-organic-frameworks, which will

suffer from weak diffraction because of their large unit cell volumes as $I_{diff} \approx V_{crystal}/V^2_{cell}$.

The appeal of synchrotron sources is also evidenced by the ability to optimise experiments by selecting a wavelength from a wide spectrum. High-pressure data collections suffer from incompleteness because the high-pressure cell restricts the angle of diffraction and accessible reciprocal-space volume. This is improved by selecting a low incident wavelength *e.g.* Ag-Kα λ=0.5608 Å which has the effect of compressing the diffraction pattern allowing more reflections to be harvested for a given angular range.[55] Conversely, data collection of twinned or large unit cell crystals can be optimised by increasing the wavelength, which has the effect of resolving reflections on the detector.

Synchrotron radiation sources and X-ray diffraction beamlines are therefore ideal for obtaining full three-dimensional structures for relatively complex and weakly diffracting systems. The need for such resources is apparent for most high-pressure crystallographic studies and forms the main route for experimental work in this thesis.

1.3.2. Beamlines 11.3.1 and 12.2.2

Single-crystal X-ray diffraction experiments were performed on the Small Molecule Chemical Crystallography and Diffraction at Non-ambient Conditions beamlines, 11.3.1 and 12.2.2 at the Advanced Light Source (ALS).

Beamline 11.3.1 produces a 2.0–0.7 Å (6–17 keV) X-ray beam focused to a 280 x 90 μm^2 spot size suitable for studying small crystals, *ca.* 10 μm^3, and high-pressure samples.[68, 75] X-rays are produced from a bending magnet with a magnetic field strength of 1.27 T. The white beam is monochromated by a Si(111) crystal. The monochromated light then passes through horizontal slits, followed by the toroidal focussing mirror. The optical design is simple, comprising only two components: a monochromator followed by the focussing mirror.

The end station comprised a conventional, three-circle, fixed chi Bruker D8 diffractometer, rotating about a horizontal axis. The detector was positioned perpendicular to the plane of scattering, as polarisation effects result in zero diffracted intensities along the horizontal polarisation plane in synchrotron radiation. Diffraction data were measured on a PHOTON II charge-integrating pixel array detector (CPAD), which allowed shutterless data collection and high sample throughput. Data collections and processing were done using the APEX3 suite of programs, a widely used commercial software package, which simplifies the user experience during beamtime. The end station also comprised an Oxford Cryosystems Cryostream 800+ for low temperature measurements. The 11.3.1 X-ray spectrum, however, is not suitable for all high-pressure experiments due to its limited flux at shorter wavelengths.[68]

Beamline 12.2.2 produces shorter wavelength X-rays than 11.3.1 (2.0–0.3 Å (6–40 keV)) with high-flux, suitable for most high-pressure studies.[52, 68, 76] The increased flux is a consequence of the 5.29 T superbend magnet X-ray source, which has a higher beamline critical energy (12 keV) than Beamline 11.3.1 (3 keV).

The optical setup of 12.2.2 comprised a parabolic collimating mirror which directs X-rays into a Kohzu double crystal Si(111) monochromator. A second toroidal mirror focuses and directs the monochromated X-rays into the hutch on End Station 1, which was equipped with a STOE Eulerian cradle diffractometer. However, X-rays can continue along the same path via a pair of Kikpatrick–Baez (KB) mirrors which refocus the beam at the sample position on End Station 2. A spot size of either 10x10 or 30x30 μm^2 is obtainable by slitting the incident beam. All experiments performed on Beamline 12.2.2 in this thesis were done on End Station 2. The station comprised a single Huber rotation axis (ϕ) stacked between two *xyz* stages. The lower *xyz* stage was used to centre the rotation axis while the upper *xyz* stage was used to centre the sample on ϕ and the X-ray focus spot. Single-crystal diffraction data were collected on a Perkin Elmer amorphous silicon detector and data processed using the APEX3 suite of programs. The beamline set-up accommodates a multitude of DAC types and external apparatus such as heating and cooling systems.[52] Fuller descriptions of the beamline setup and capabilities can be found in the literature.[52, 76]

Experimental aims were considered before deciding on which beamline to use for data collection. Beamline 11.3.1 can only accommodate small Merrill-Bassett DACs, while the 12.2.2 configuration accommodates most cell types, including the heavier BX90. The incident beam size was also considered. The finer spot size available on beamline 12.2.2 allows focussing of the beam on specific crystallites contained in the pressure cell, which minimises contamination from diffraction of the gasket material. On Beamline 11.3.1, however, the beam spot size is fixed. Therefore, suitably large sample chambers were prepared prior to experimentation to reduce beam-clipping. Beamline 12.2.2 favoured higher-pressure experiments (> 10 GPa), which required small crystals and sample chambers. Beamline 12.2.2 also offered improved data completeness over 11.3.1 because of its access to higher flux X-rays at shorter wavelengths. Data processing in all cases, required careful masking of

experimental features such as shading from the cell body, powder diffraction rings from the gasket material, and diamond peaks, see **Figure 1.2**.

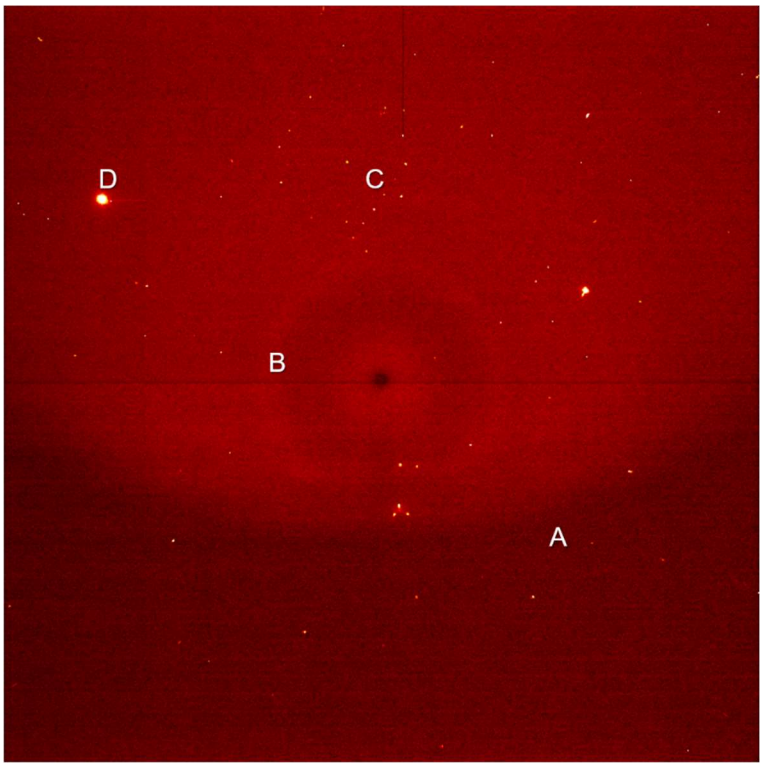

Figure 1.2 A high-pressure single-crystal frame collected on beamline 12.2.2. A, denotes the detector area shaded by the body of the DAC.B, denotes a faint powder ring from the gasket material. C, denotes a region rich in sample reflections. D- denotes an intense diamond reflection.

1.4. Neutron Sources in High-Pressure Crystallography

Neutron diffraction techniques offer a complementary alternative to X-ray methods and are notably advantageous in the study of low atomic number, *Z*, containing molecules. The benefits of neutron diffraction arise from the properties of the neutron. Firstly, neutrons are highly penetrating, and thus suitable probes for samples contained in high-pressure apparatus. Neutrons are scattered by nuclei in atoms, which act like point scatterers, unlike X-rays which are scattered by diffuse electron clouds. The resultant neutron diffraction peaks are weaker than in X-ray scattering so the neutron experiment typically requires larger samples. Secondly, the diffracted intensities from neutron experiments are independent of *Z*, and low-*Z* atoms like hydrogen or deuterium (*Z*=1), which are strong neutron scatterers but weak X-ray scatterers, are readily located. Scattering intensities of X-rays are seen to increase almost linearly with increasing *Z*. However, the scattering intensities of neutrons are seen to vary randomly with *Z*. Vanadium (*Z*=23) diffracts X-rays readily, but is a poor neutron scatterer, which makes vanadium a useful metal in machined components of the neutron experiment *e.g.* sample vessels. The differences in neutron scattering factors of elements readily allows contrast between adjacent elements and even isotopes. Neutron diffraction was used in Chapters 2 and 4 for its advantages in locating light atoms in organic molecules at high-pressures but does not form the main experimental approach in this thesis. The method is mainly mentioned here for completeness. Fuller reviews of neutron techniques and instrumentation with applications in high-pressure crystallography can be found in the literature.[77-79]

All neutron diffraction data were measured on the PEARL beamline at Target Station 1 at ISIS in this thesis. PEARL is a neutron time-of-flight (TOF) powder diffraction instrument designed around the Paris-Edinburgh (PE) press, a device capable of exerting high pressure on crystalline samples (shown in **Figure 1.3**). The PE cell is not too dissimilar from the DAC. It operates in an opposed anvil geometry with a null-scattering gasket chamber (TiZr) containing

the crystalline sample, pressure marker and PTM. The anvils, however, are made from either tungsten carbide, zirconia-toughened alumina (ZTA) or sintered diamond, where sintered diamond anvils favour higher pressure experiments. The cell was pressurised by an *in situ* hydraulic press, which can apply loads of up to 250 tonnes between the anvils.[80] The PE press provides access to pressures between 0.5 and 28 GPa, and temperature can be controlled by external apparatuses between 80 and 1400 K.[81]

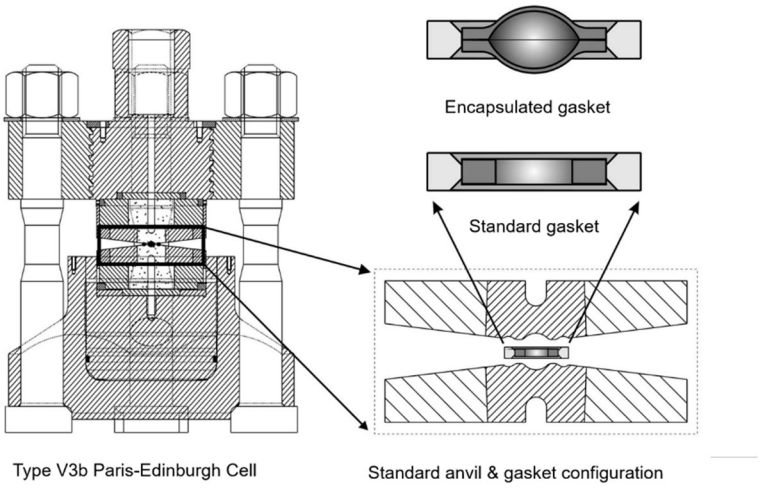

Figure 1.3 The V3b Paris-Edinburgh cell (left) used in neutron diffraction measurements on PEARL. Insets show the anvil and gasket geometry.[80]

The TOF technique is well suited to the high-pressure experiment. In TOF neutron diffraction, a pulsed, continuous spectrum of wavelengths, generated by a spallation source, irradiates the sample while the diffraction angle (θ) remains fixed. This approach differs from the conventional X-ray diffraction experiment in which the wavelength is held constant and θ is varied. Consequently, the sample contained in the large, bulky PE cell and detector positions can remain fixed as complete diffraction patterns are obtained at a single scattering angle. On the PEARL beamline, diffracted neutrons are measured as a function of time and *d*-spacing on an array of ZnS detector banks situated in transverse and longitudinal positions about the hutch, optimised for the geometry of the PE press. The resultant accessible *d*-spacing in such an arrangement ranges from, 0.4–4.1 Å in the transverse detector bank for standard

20 ms pulses, to a maximum of 12.5 Å in the longitudinal detector banks. The PEARL instrument therefore represents a suitable tool for extracting high-resolution structural information under variable temperature and pressure conditions.

1.5. Structure Analysis by the PIXEL Method

The PIXEL method is a semiclassical density sums computational technique developed by Gavezzotti,[82-83] that has been used in high-pressure studies to characterise polymorph stability in molecular solids.[16, 26, 84-86] For a modest computational cost, the PIXEL method accurately reproduces enthalpies of organic solids and the results obtained are comparable to those of *ab initio* calculations and energies of sublimation.[87-88] PIXEL gives the total crystal lattice energies as well as a breakdown into its constituent Coulombic, dispersion, repulsion and polarisation terms. It also provides molecule-molecule interaction energies between dimers in the crystal lattice, so that roles of specific interactions in the crystal structure can be probed. The method has been used extensively in this thesis to rationalise the role of intermolecular interactions in phase stabilities in high-pressure structures and to interpret mechanisms of phase transitions.

The appeal of the PIXEL method, in combination with structural information such as bond distances or molecule conformation, is that the energetics in crystal packing can be compared between polymorphs and phase stabilities explained. In variable temperature or pressure studies, the evolution of stabilising or destabilising contacts between phases can be used to explain the driving force of transitions. For example, in the transition of L-serine II to III, a substantial increase in attractive energy of a molecular pair, as calculated by PIXEL, suggests the transition is driven by the bifurcation of a short hydrogen-bond.[89]

PIXEL uses electron densities of a single molecule structure, calculated by a standard quantum chemical package such as GAUSSIAN09, using the MP2/6-31G** level of theory. The calculations produce a density map on a three-dimensional grid typically of step size 0.08 Å in an array of 100–150 symmetry-generated molecules.[88] Electron densities are then condensed into cubes of *n* x *n* x *n* super-pixels to reduce the overall number of pixels. A typical choice of condensation level is *n*=4, the smaller the value of *n*, the finer the resolution of the calculation and more accurate the result, although this comes at the expense of increased computation times. Any condensed pixels that have a charge below a specified threshold (10^{-6} electrons) are removed from the calculation to improve the computational efficiency.[87] The remaining pixels are then renormalised to have an overall neutral charge. The calculations of the constituent energy terms (given below) are then performed between pairs of pixels in a central reference molecule and those generated by symmetry in a cluster of a given radius (typically 18 Å for small, neutral, organic molecules).

Coulombic energies are calculated as sums of the intermolecular pixel-pixel, pixel-nucleus and nucleus-nucleus by the electrostatic potential energy equation:

$$E_{coul} = \frac{q_1 q_2}{4\pi\varepsilon_o r} \tag{8}$$

where $\frac{1}{4\pi\varepsilon_o}$ is Coulomb's constant, and r is the separation between the point charges q_1 and q_2.

The polarisability of any given pixel, *i,* is calculated by assigning the pixel to a specific atom in the molecule to which the distance between them is the smallest fraction of the atomic radius. The atomic polarisability, α_i, is then approximated by the following scheme:

$$\alpha_i = \left(\frac{q_1}{Z_{atom}}\right) \alpha_{atom} \tag{9}$$

where Z_{atom} and α_{atom} are the atomic charge and polarisability of the atom in pixel, *i*. The electric field exerted on each pixel, ε_i, by its surrounding molecules is then calculated, including an adjustable damping factor ε_{max} to prevent physically unrealistic polarisation contributions at very short separations:

$$E_{pol,i} = -\tfrac{1}{2}\alpha_i[\varepsilon_i d_i]^2 \text{ when } \varepsilon<\varepsilon_{max} \tag{10}$$

$$d_i = \exp[-(\varepsilon_i/(\varepsilon_{max} - \varepsilon_i)] \tag{11}$$

If $\varepsilon > \varepsilon_{max}{}^2$ then E_{pol} is set to zero. The total polarisation energy of a molecule is the summation of all the polarisation energies from each of its associated pixels:

$$E_{pol,\,tot} = \sum E_{pol,i} \tag{12}$$

The PIXEL dispersion energy terms (E_{disp}) of molecules A and B are calculated from the sum of pixel-pixel dispersion terms, E_{ij}, in a London-type equation:

$$E_{disp\,A,B} = \frac{(-3/4)\sum_{i,A}\sum_{j,B} E_{OS}\, f(R)\, \alpha_i\alpha_j}{(4\pi\varepsilon_o)^2 (R_{ij})^6} \tag{13}$$

$$f(R) = \exp\left[-(D/R_{ij}-1)^2\right] \text{ for } R_i < D \tag{14}$$

$$f(R) = 1 \text{ for } R_i > D \tag{15}$$

Again, a damping factor, *f(r)*, is introduced in the polarisation term to avoid singularities arising from very short pixel-pixel distances. The *f(r)* term is borrowed from quantum mechanical methods,[90] where, *D*, is an empirical parameter that represents the damping threshold distance which can be adjusted. The E_{OS} term in Equation 13 is the 'oscillator strength' of each pixel. Each pixel is considered as a separate oscillating charge with an ionisation potential, I_i, given by:

$$E_{OS} = (I_i I_j)^{\frac{1}{2}} \tag{16}$$

where I_i is a function of the ionisation potential, I^o, of the atom in pixel *i* and the distance between the atomic nucleus and the pixel, R_i:

$$I_i = I^o \exp(-\beta R_i) \tag{17}$$

Where β is an empirical value that acts as an atom specific dispersion energy coefficient.

The repulsion energy is approximated to be proportional to the overlap of electron densities between molecules A and B, S_{AB}:

$$S_{AB} = \sum_{i,A} \sum_{j,B} \left[\rho_i(A)\rho_j(B)\right] V \tag{18}$$

where ρ_i and ρ_j are the charge densities of molecules A and B, and V is the pixel volume. The calculation uses the original uncontracted electron densities so that the repulsion term is independent of the condensation level. The

contributions from the overlap in each pixel is subdivided into those of the atomic species, *m* and *n*, (S_{mn}) by:

$$E_{rep,mn} = (K_1 - K_2 \Delta\chi_{mn}) S_{mn} \quad (19)$$

where $\Delta\chi_{mn}$ is the difference in electronegativity of the atomic species *m* and *n*, and K_1 and K_2 are empirical parameters. The negative sign of K_2 offsets large reorganisations of electron density that result when atoms with different electronegativities come into close contact. The total repulsion term is calculated as the sum of all pairs of *mn*:

$$E_{rep,\ total} = \sum_{mn} E_{rep,mn} \quad (20)$$

Combining the Coulombic, polarisation, dispersion and repulsion energy terms then give the total intermolecular energy:

$$E_{tot} = E_{coul} + E_{pol} + E_{disp} + E_{rep} \quad (21)$$

and the sum of all the molecular contacts in the cluster gives the crystal lattice energy. The use and validation of PIXEL is demonstrated in the study of benzene at ambient pressure and 183 K.[91] The PIXEL calculated lattice energy is 42.1 kJ mol^{-1} which agrees with the estimated value from experimental measurements, 50 kJ mol^{-1} and the *ab initio* calculated value, 52.1 kJ mol^{-1}. A breakdown into the component energies of the nearest neighbour pairs of molecules (of which there are four) shows repulsion and dispersion terms, which are sensitive to intermolecular separation, tend to cancel and the dominating stabilising contribution comes from the Coulombic term. PIXEL reproduces *ab initio*

calculations well at a modest computational cost and time. It therefore represents a useful tool for realising physically meaningful interaction and crystal lattice energies.

1.6. Thesis Aims

The overall aim of this thesis is to explore the effects of high-pressure on intermolecular interactions and their roles in phase transitions.

To achieve this overall aim, this thesis will i) extend the current experimental pressure limit for structural analysis of strong hydrogen-bonding present in an amino acid and ii) halogen-bonding in a halogen substituted cyanobenzene. To complete the range of interactions investigated, the compression of metal···metal and dispersion-based interactions will be studied in iii) an organometallic complex and iv) pyridine. The roles of these interactions in compression mechanisms and phase transitions will be rationalised by applying the PIXEL method.

1.7. References

1. O'Bannon, E.; Beavers, C. M.; Kunz, M.; Williams, Q., The high-pressure phase of lawsonite: A single crystal study of a key mantle hydrous phase. *Journal of Geophysical Research: Solid Earth* **2017**.

2. Vennari, C. E.; Williams, Q., A novel carbon bonding environment in deep mantle high-pressure dolomite. *American Mineralogist* **2018,** *103* (1), 171-174.

3. Kato, C.; Li, L.; Nogi, Y.; Nakamura, Y.; Tamaoka, J.; Horikoshi, K., Extremely Barophilic Bacteria Isolated from the Mariana Trench, Challenger Deep, at a Depth of 11,000 Meters. *Applied and Environmental Microbiology* **1998,** *64* (4), 1510-1513.

4. Hazael, R.; Meersman, F.; Ono, F.; McMillan, P. F., Pressure as a Limiting Factor for Life. *Life* **2016,** *6* (3), 34.

5. Zakharov, B. A.; Boldyreva, E. V., High pressure: a complementary tool for probing solid-state processes. *CrystEngComm* **2019,** *21* (1), 10-22.

6. Boldyreva, E., High-pressure diffraction studies of molecular organic solids. A personal view. *Acta Crystallographica Section A* **2008,** *64* (1), 218-231.

7. Hejny, C.; Minkov, V. S., High-pressure crystallography of periodic and aperiodic crystals. *IUCrJ* **2015,** *2* (2), 218-229.

8. Katrusiak, A., High-pressure crystallography. *Acta Crystallographica Section A* **2008,** *64* (1), 135-148.

9. Ballaran, T. B.; Kurnosov, A.; Trots, D., Single-crystal X-ray diffraction at extreme conditions: a review. *High Pressure Research* **2013,** *33* (3), 453-465.

10. Fabbiani, F. P. A.; Pulham, C. R., High-pressure studies of pharmaceutical compounds and energetic materials. *Chemical Society Reviews* **2006,** *35* (10), 932-942.

11. Klebe, G.; Graser, F.; Hadicke, E.; Berndt, J., Crystallochromy as a solid-state effect: correlation of molecular conformation, crystal packing and colour in perylene-3,4:9,10-bis(dicarboximide) pigments. *Acta Crystallographica Section B* **1989,** *45* (1), 69-77.

12. Diao, Y.; Lenn, K. M.; Lee, W.-Y.; Blood-Forsythe, M. A.; Xu, J.; Mao, Y.; Kim, Y.; Reinspach, J. A.; Park, S.; Aspuru-Guzik, A.; Xue, G.; Clancy, P.; Bao, Z.; Mannsfeld, S. C. B., Understanding Polymorphism in Organic Semiconductor Thin Films through Nanoconfinement. *Journal of the American Chemical Society* **2014,** *136* (49), 17046-17057.

13. Galek, P. T. A.; Allen, F. H.; Fábián, L.; Feeder, N., Knowledge-based H-bond prediction to aid experimental polymorph screening. *CrystEngComm* **2009,** *11* (12), 2634-2639.

14. Reilly, A. M.; Cooper, R. I.; Adjiman, C. S.; Bhattacharya, S.; Boese, A. D.; Brandenburg, J. G.; Bygrave, P. J.; Bylsma, R.; Campbell, J. E.; Car, R.; Case, D. H.; Chadha, R.; Cole, J. C.; Cosburn, K.; Cuppen, H. M.; Curtis, F.; Day, G. M.; DiStasio Jr, R. A.; Dzyabchenko, A.; van Eijck, B. P.; Elking, D. M.; van den Ende, J. A.; Facelli, J. C.; Ferraro, M. B.; Fusti-Molnar, L.; Gatsiou, C.-A.; Gee, T. S.; de Gelder, R.; Ghiringhelli, L. M.; Goto, H.; Grimme, S.; Guo, R.; Hofmann, D. W. M.; Hoja, J.; Hylton, R. K.; Iuzzolino,

L.; Jankiewicz, W.; de Jong, D. T.; Kendrick, J.; de Klerk, N. J. J.; Ko, H.-Y.; Kuleshova, L. N.; Li, X.; Lohani, S.; Leusen, F. J. J.; Lund, A. M.; Lv, J.; Ma, Y.; Marom, N.; Masunov, A. E.; McCabe, P.; McMahon, D. P.; Meekes, H.; Metz, M. P.; Misquitta, A. J.; Mohamed, S.; Monserrat, B.; Needs, R. J.; Neumann, M. A.; Nyman, J.; Obata, S.; Oberhofer, H.; Oganov, A. R.; Orendt, A. M.; Pagola, G. I.; Pantelides, C. C.; Pickard, C. J.; Podeszwa, R.; Price, L. S.; Price, S. L.; Pulido, A.; Read, M. G.; Reuter, K.; Schneider, E.; Schober, C.; Shields, G. P.; Singh, P.; Sugden, I. J.; Szalewicz, K.; Taylor, C. R.; Tkatchenko, A.; Tuckerman, M. E.; Vacarro, F.; Vasileiadis, M.; Vazquez-Mayagoitia, A.; Vogt, L.; Wang, Y.; Watson, R. E.; de Wijs, G. A.; Yang, J.; Zhu, Q.; Groom, C. R., Report on the sixth blind test of organic crystal structure prediction methods. *Acta Crystallographica Section B* **2016,** *72* (4), 439-459.

15. Braga, D., Crystal engineering, Where from? Where to? *Chemical Communications* **2003,** (22), 2751-2754.

16. Moggach, S. A.; Parsons, S.; Wood, P. A., High-pressure polymorphism in amino acids. *Crystallography Reviews* **2008,** *14* (2), 143-184.

17. Johnstone, R. D. L.; Lennie, A. R.; Parker, S. F.; Parsons, S.; Pidcock, E.; Richardson, P. R.; Warren, J. E.; Wood, P. A., High-pressure polymorphism in salicylamide. *CrystEngComm* **2010,** *12* (4), 1065-1078.

18. Nyman, J.; Day, G. M., Static and lattice vibrational energy differences between polymorphs. *CrystEngComm* **2015,** *17* (28), 5154-5165.

19. Zakharov, B. A.; Seryotkin, Y. V.; Tumanov, N. A.; Paliwoda, D.; Hanfland, M.; Kurnosov, A. V.; Boldyreva, E. V., The role of fluids in high-pressure polymorphism of drugs: different behaviour of β-chlorpropamide in different inert gas and liquid media. *RSC Advances* **2016,** *6* (95), 92629-92637.

20. Fisch, M.; Lanza, A.; Boldyreva, E.; Macchi, P.; Casati, N., Kinetic Control of High-Pressure Solid-State Phase Transitions: A Case Study on l-Serine. *The Journal of Physical Chemistry C* **2015,** *119* (32), 18611-18617.

21. Moggach, S. A.; Allan, D. R.; Clark, S. J.; Gutmann, M. J.; Parsons, S.; Pulham, C. R.; Sawyer, L., High-pressure polymorphism in l-cysteine: the crystal structures of l-cysteine-III and l-cysteine-IV. *Acta Crystallographica Section B* **2006,** *62* (2), 296-309.

22. Bull, C. L.; Flowitt-Hill, G.; de Gironcoli, S.; Kucukbenli, E.; Parsons, S.; Pham, C. H.; Playford, H. Y.; Tucker, M. G., [zeta]-Glycine: insight into the mechanism of a polymorphic phase transition. *IUCrJ* **2017,** *4* (5), 569-574.

23. Wood, P. A.; McKinnon, J. J.; Parsons, S.; Pidcock, E.; Spackman, M. A., Analysis of the compression of molecular crystal structures using Hirshfeld surfaces. *CrystEngComm* **2008,** *10* (4), 368-376.

24. Dove Martin, T., Review: Theory of displacive phase transitions in minerals. In *American Mineralogist*, 1997; Vol. 82, p 213.

25. Dmitriev, V. P.; Rochal, S. B.; Gufan, Y. M.; Toledano, P., Definition of a Transcendental Order Parameter for Reconstructive Phase Transitions. *Physical Review Letters* **1988,** *60* (19), 1958-1961.

26. Wood, P. A.; Forgan, R. S.; Henderson, D.; Parsons, S.; Pidcock, E.; Tasker, P. A.; Warren, J. E., Effect of pressure on the crystal structure of salicylaldoxime-I, and the structure of salicylaldoxime-II at 5.93 GPa. *Acta Crystallographica Section B* **2006,** *62* (6), 1099-1111.

27. Seryotkin, Y. V.; Drebushchak, T. N.; Boldyreva, E. V., A high-pressure polymorph of chlorpropamide formed on hydrostatic compression of the [alpha]-form in saturated ethanol solution. *Acta Crystallographica Section B* **2013,** *69* (1), 77-85.

28. Marciniak, J.; Bąkowicz, J.; Dobrowolski, M. A.; Dziubek, K. F.; Kaźmierczak, M.; Paliwoda, D.; Rajewski, K. W.; Sobczak, S.; Stachowicz, M.; Katrusiak, A., Most Frequent Organic Interactions Compressed in Toluene. *Crystal Growth & Design* **2016,** *16* (3), 1435-1441.

29. Fabbiani, F. P. A.; Buth, G.; Levendis, D. C.; Cruz-Cabeza, A. J., Pharmaceutical hydrates under ambient conditions from high-pressure seeds: a case study of GABA monohydrate. *Chemical Communications* **2014,** *50* (15), 1817-1819.

30. Woodall, C. H.; Christensen, J.; Skelton, J. M.; Hatcher, L. E.; Parlett, A.; Raithby, P. R.; Walsh, A.; Parker, S. C.; Beavers, C. M.; Teat, S. J.; Intissar, M.; Reber, C.; Allan, D. R., Observation of a re-entrant phase transition in the molecular complex tris([mu]2-3,5-diisopropyl-1,2,4-triazolato-[kappa]2N1:N2)trigold(I) under high pressure. *IUCrJ* **2016,** *3* (5), 367-376.

31. Resnati, G.; Boldyreva, E.; Bombicz, P.; Kawano, M., Supramolecular interactions in the solid state. *IUCrJ* **2015,** *2* (6), 675-690.

32. Kaźmierczak, M.; Katrusiak, A., Bimodal Distribution of the Shortest Intermolecular Contacts in Crystals of Organic Compounds. *Crystal Growth & Design* **2014,** *14* (5), 2223-2229.

33. Kaźmierczak, M.; Katrusiak, A., Quantitative estimate of cohesion forces. *CrystEngComm* **2015,** *17* (48), 9423-9430.

34. Tidey, J. P.; Wong, H. L. S.; Schröder, M.; Blake, A. J., Structural chemistry of metal coordination complexes at high pressure. *Coordination Chemistry Reviews* **2014,** *277-278*, 187-207.

35. Arnold, P. L.; Prescimone, A.; Farnaby, J. H.; Mansell, S. M.; Parsons, S.; Kaltsoyannis, N., Characterizing Pressure-Induced Uranium C–H Agostic Bonds. *Angewandte Chemie International Edition* **2015,** *54* (23), 6735-6739.

36. Allan, D. R.; Bailey, D.; Bird, N.; Blake, A. J.; Champness, N. R.; Huang, D.; Keane, C. P.; McMaster, J.; Prior, T. J.; Tidey, J. P.; Schroder, M., High-pressure studies of palladium and platinum thioether macrocyclic dihalide complexes. *Acta Crystallographica Section B* **2014,** *70* (3), 469-486.

37. Shepherd, H.; Tonge, G.; Hatcher, L.; Bryant, M.; Knichal, J.; Raithby, P.; Halcrow, M.; Kulmaczewski, R.; Gagnon, K.; Teat, S., A High Pressure Investigation of the Order-Disorder Phase Transition and Accompanying Spin Crossover in [FeL12](ClO4)2 (L1 = 2,6-bis{3-methylpyrazol-1-yl}-pyrazine). *Magnetochemistry* **2016,** *2* (1), 9.

38. Rodríguez-Velamazán, J. A.; Fabelo, O.; Beavers, C. M.; Natividad, E.; Evangelisti, M.; Roubeau, O., A Multifunctional Magnetic Material under Pressure. *Chemistry – A European Journal* **2014,** *20* (26), 7956-7961.

39. Moggach, S. A.; Bennett, T. D.; Cheetham, A. K., The Effect of Pressure on ZIF-8: Increasing Pore Size with Pressure and the Formation of a High-Pressure Phase at 1.47 GPa. *Angewandte Chemie International Edition* **2009,** *48* (38), 7087-7089.

40. Gagnon, K. J.; Beavers, C. M.; Clearfield, A., MOFs Under Pressure: The Reversible Compression of a Single Crystal. *Journal of the American Chemical Society* **2013,** *135* (4), 1252-1255.

41. Woodall, C. H.; Beavers, C. M.; Christensen, J.; Hatcher, L. E.; Intissar, M.; Parlett, A.; Teat, S. J.; Reber, C.; Raithby, P. R., Hingeless Negative Linear Compression in the Mechanochromic Gold Complex [(C6F5Au)2(μ-1,4-diisocyanobenzene)]. *Angewandte Chemie International Edition* **2013,** *52* (37), 9691-9694.

42. Ortiz, A. U.; Boutin, A.; Gagnon, K. J.; Clearfield, A.; Coudert, F.-X., Remarkable Pressure Responses of Metal–Organic Frameworks: Proton Transfer and Linker Coiling in Zinc Alkyl Gates. *Journal of the American Chemical Society* **2014,** *136* (32), 11540-11545.

43. Matsuoka, T.; Shimizu, K., Direct observation of a pressure-induced metal-to-semiconductor transition in lithium. *Nature* **2009,** *458*, 186.

44. Matsuoka, T.; Sakata, M.; Nakamoto, Y.; Takahama, K.; Ichimaru, K.; Mukai, K.; Ohta, K.; Hirao, N.; Ohishi, Y.; Shimizu, K., Pressure-induced reentrant metallic phase in lithium. *Physical Review B* **2014,** *89* (14), 144103.

45. Howie, R. T.; Turnbull, R.; Binns, J.; Frost, M.; Dalladay-Simpson, P.; Gregoryanz, E., Formation of xenon-nitrogen compounds at high pressure. *Scientific Reports* **2016,** *6*, 34896.

46. Somayazulu, M.; Dera, P.; Smith, J.; Hemley, R. J., Structure and stability of solid Xe(H2)n. *The Journal of Chemical Physics* **2015,** *142* (10), 104503.

47. Wu, G.; Huang, X.; Huang, Y.; Pan, L.; Li, F.; Li, X.; Liu, M.; Liu, B.; Cui, T., Confirmation of the Structural Phase Transitions in XeF2 under High Pressure. *The Journal of Physical Chemistry C* **2017,** *121* (11), 6264-6271.

48. Bassett, W. A., Diamond anvil cell, 50th birthday. *High Pressure Research* **2009,** *29* (2), 163-186.

49. Weir, C. E.; Lippincott, E. R.; Vanvalkenburg, A.; Bunting, E. N., Infrared Studies in the 1-Micron to 15-Micron Region to 30,000 Atmospheres. *Journal of Research of the National Bureau of Standards—A. Physics and Chemistry* **1959,** *63* (1), 55-62.

50. The Nobel Prize in Physics 1946, NobelPrize.org, Nobel Media AB 2019. <https://www.nobelprize.org/prizes/physics/1946/summary/> (accessed 12/04/2019).

51. Jayaraman, A., Diamond anvil cell and high-pressure physical investigations. *Reviews of Modern Physics* **1983,** *55* (1), 40.

52. Stan, C. V.; Beavers, C. M.; Kunz, M.; Tamura, N., X-Ray Diffraction under Extreme Conditions at the Advanced Light Source. *Quantum Beam Science* **2018,** *2* (1), 4.

53. Miletich, R.; Allan, D. R.; Kuhs, W. F., High-Pressure Single-Crystal Techniques. *Reviews in Mineralogy and Geochemistry* **2000,** *41* (1), 445-519.

54. Shen, G.; Mao, H. K., High-pressure studies with x-rays using diamond anvil cells. *Reports on Progress in Physics* **2016,** *80* (1), 016101.

55. Merrill, L.; Bassett, W. A., Miniature diamond anvil pressure cell for single crystal x-ray diffraction studies. *Review of Scientific Instruments* **1974,** *45* (2), 290-294.

56. Kantor, I.; Prakapenka, V.; Kantor, A.; Dera, P.; Kurnosov, A.; Sinogeikin, S.; Dubrovinskaia, N.; Dubrovinsky, L., BX90: A new diamond anvil cell design for X-ray diffraction and optical measurements. *Review of Scientific Instruments* **2012,** *83* (12), 125102.

57. Moggach, S. A.; Allan, D. R.; Parsons, S.; Warren, J. E., Incorporation of a new design of backing seat and anvil in a Merrill-Bassett diamond anvil cell. *Journal of Applied Crystallography* **2008,** *41*, 249-251.

58. Dawson, A.; Allan, D. R.; Parsons, S.; Ruf, M., Use of a CCD diffractometer in crystal structure determinations at high pressure. *Journal of Applied Crystallography* **2004,** *37* (3), 410-416.

59. Klotz, S.; Chervin, J. C.; Munsch, P.; Marchand, G. L., Hydrostatic limits of 11 pressure transmitting media. *Journal of Physics D: Applied Physics* **2009,** *42* (7), 075413.

60. Angel, R. J.; Bujak, M.; Zhao, J.; Gatta, G. D.; Jacobsen, S. D., Effective hydrostatic limits of pressure media for high-pressure crystallographic studies. *Journal of Applied Crystallography* **2007,** *40* (1), 26-32.

61. Jephcoat, A. P.; Mao, H. K.; Bell, P. M., Static compression of iron to 78 GPa with rare gas solids as pressure-transmitting media. *Journal of Geophysical Research: Solid Earth* **1986,** *91* (B5), 4677-4684.

62. Dewaele, A.; Loubeyre, P.; André, R.; Härtwig, J., An x-ray topographic study of diamond anvils: Correlation between defects and helium diffusion. *Journal of Applied Physics* **2006,** *99* (10), 104906.

63. Mao, H. K.; Bell, P. M.; Shaner, J. W.; Steinberg, D. J., Specific volume measurements of Cu, Mo, Pd, and Ag and calibration of the ruby R1 fluorescence pressure gauge from 0.06 to 1 Mbar. *Journal of Applied Physics* **1978,** *49* (6), 3276-3283.

64. Akahama, Y.; Kawamura, H., High-pressure Raman spectroscopy of diamond anvils to 250GPa: Method for pressure determination in the multimegabar pressure range. *Journal of Applied Physics* **2004,** *96* (7), 3748-3751.

65. Birch, F., Finite elastic strain of cubic crystals. *Phys. Rev.* **1947,** *71*, 809.

66. Birch, F., Finite strain isotherm and velocities for single-crystal and polycrystalline NaCl at high pressures and 300°K. *Journal of Geophysical Research: Solid Earth* **1978,** *83* (B3), 1257-1268.

67. Anzellini, S.; Dewaele, A.; Occelli, F.; Loubeyre, P.; Mezouar, M., Equation of state of rhenium and application for ultra high pressure calibration. *Journal of Applied Physics* **2014,** *115* (4), 043511.

68. McCormick, L. J.; Giordano, N.; Teat, S. J.; Beavers, C. M., Chemical Crystallography at the Advanced Light Source. *Crystals* **2017,** *7* (12), 382.

69. Baruchel, J.; Hodeau, J. L.; Lehmann, M. S.; Regnard, J. R., *Neutron and synchrotron radiation for condensed matter studies Volume 1: theory, instruments and methods*. Editions de la Physique: France, 1993.

70. White, A.; Goldberg, K.; Kevan, S.; Leitner, D.; Robin, D.; Steier, C.; Yarris, L., A New Light for Berkeley Lab—the Advanced Light Source Upgrade. *Synchrotron Radiation News* **2019,** *32* (1), 32-36.

71. Materlik, G.; Rayment, T.; Stuart, D. I., Diamond Light Source: status and perspectives. *Philosophical Transactions of the Royal Society A: Mathematical, Physical and Engineering Sciences* **2015,** *373* (2036), 20130161.

72. Drube, W.; Bieler, M.; Caliebe, W. A.; Schulte-Schrepping, H.; Spengler, J.; Tischer, M.; Wanzenberg, R., The PETRA III extension. *AIP Conference Proceedings* **2016,** *1741* (1), 020035.

73. Bachmann, R.; Kohler, H.; Schulz, H.; Weber, H.-P., Structure investigation of a 6[mu]m CaF2 crystal with synchrotron radiation. *Acta Crystallographica Section A* **1985,** *41* (1), 35-40.

74. Harding, M., Recording Diffraction Data for Structure Determination for Very Small Crystals. *Journal of synchrotron radiation* **1996,** *3* (6), 250-259.

75. Thompson, A. C.; Padmore, H. A.; Oliver, A. G.; Teat, S. J.; Celestre, R. S.; Clark, S. M.; Domning, E. E.; Franck, K. D.; Morrison, G. Y., A Simple High Performance Beamline for Small Molecule Chemical Crystallography. *AIP Conference Proceedings* **2004,** *705* (1), 482-485.

76. Kunz, M.; MacDowell, A. A.; Caldwell, W. A.; Cambie, D.; Celestre, R. S.; Domning, E. E.; Duarte, R. M.; Gleason, A. E.; Glossinger, J. M.; Kelez, N.; Plate, D. W.; Yu, T.; Zaug, J. M.; Padmore, H. A.; Jeanloz, R.; Alivisatos, A. P.; Clark, S. M., A beamline for high-pressure studies at the Advanced Light Source with a superconducting bending magnet as the source. *Journal of synchrotron radiation* **2005,** *12* (5), 650-658.

77. Klotz, S., Techniques in high pressure neutron scattering. CRC press: 2012.

78. Bailey, I., A review of sample environments in neutron scattering. *Zeitschrift für Kristallographie-Crystalline Materials* **2003,** *218* (2), 84-95.

79. Coates, L.; Cao, H. B.; Chakoumakos, B. C.; Frontzek, M. D.; Hoffmann, C.; Kovalevsky, A. Y.; Liu, Y.; Meilleur, F.; Santos, A. M. d.; Myles, D. A. A.; Wang, X. P.; Ye, F., A suite-level review of the neutron single-crystal diffraction instruments at Oak Ridge National Laboratory. *Review of Scientific Instruments* **2018,** *89* (9), 092802.

80. Marshall, W. G.; Francis, D. J., Attainment of near-hydrostatic compression conditions using the Paris-Edinburgh cell. *Journal of Applied Crystallography* **2002,** *35* (1), 122-125.

81. Bull, C. L.; Funnell, N. P.; Tucker, M. G.; Hull, S.; Francis, D. J.; Marshall, W. G., PEARL: the high pressure neutron powder diffractometer at ISIS. *High Pressure Research* **2016,** *36* (4), 493-511.

82. Gavezzotti, A., Calculation of lattice energies of organic crystals: The PIXEL integration method in comparison with more traditional methods. *Zeitschrift für Kristallographie* **2005,** *220*, 499-510.

83. Gavezzotti, A., Efficient computer modeling of organic materials. The atom–atom, Coulomb–London–Pauli (AA-CLP) model for intermolecular electrostatic-polarization, dispersion and repulsion energies. *New Journal of Chemistry* **2011,** *35* (7), 1360-1368.

84. Johnstone, R. D. L.; Francis, D.; Lennie, A. R.; Marshall, W. G.; Moggach, S. A.; Parsons, S.; Pidcock, E.; Warren, J. E., High-pressure polymorphism in L-serine monohydrate: identification of driving forces in high pressure phase transitions and possible implications for pressure-induced protein denaturation. *CrystEngComm* **2008,** *10* (12), 1758-1769.

85. Hutchison, I. B.; Delori, A.; Wang, X.; Kamenev, K. V.; Urquhart, A. J.; Oswald, I. D. H., Polymorphism of a polymer precursor: metastable glycolide polymorph recovered via large scale high-pressure experiments. *CrystEngComm* **2015,** *17* (8), 1778-1782.

86. Fabbiani, F. P. A.; Bergantin, S.; Gavezzotti, A.; Rizzato, S.; Moret, M., X-ray diffraction and computational studies of the pressure-dependent tetrachloroethane solvation of diphenylanthracene. *CrystEngComm* **2016,** *18* (12), 2173-2181.

87. Gavezzotti, A., Towards a realistic model for the quantitative evaluation of intermolecular potentials and for the rationalization of organic crystal structures. Part I. Philosophy. *CrystEngComm* **2003,** *5* (76), 429-438.

88. Maschio, L.; Civalleri, B.; Ugliengo, P.; Gavezzotti, A., Intermolecular Interaction Energies in Molecular Crystals: Comparison and Agreement of Localized Møller–Plesset 2, Dispersion-Corrected Density Functional, and Classical Empirical Two-Body Calculations. *The Journal of Physical Chemistry A* **2011,** *115* (41), 11179-11186.

89. Wood, P. A.; Francis, D.; Marshall, W. G.; Moggach, S. A.; Parsons, S.; Pidcock, E.; Rohl, A. L., A study of the high-pressure polymorphs of L-serine using ab initio structures and PIXEL calculations. *CrystEngComm* **2008,** *10* (9), 1154-1166.

90. Birnbaum, G.; Borysow, A.; Buechele, A., Collision-induced absorption in mixtures of symmetrical linear and tetrahedral molecules: Methane–nitrogen. *The Journal of Chemical Physics* **1993,** *99* (5), 3234-3243.

91. Dunitz, J. D.; Gavezzotti, A., How molecules stick together in organic crystals: weak intermolecular interactions. *Chemical Society Reviews* **2009,** *38* (9), 2622-2633.

Chapter 2

High-Pressure Polymorphism in L-Threonine

2.1. Introduction

The amino acids have been studied extensively in the context of high-pressure polymorphism because they serve as model systems for the behaviour of H-bonding in other, potentially more complex molecules, but also in part because of their biological significance.[1-2] Glycine, the simplest amino acid, has three ambient pressure polymorphs which show differing stabilities under compression. α-Glycine is stable to 23 GPa,[3] but β-glycine transforms to δ-glycine at 0.8 GPa, while the γ-form gradually yields the ε-polymorph between 2.0 and 4.3 GPa.[4-5] ε-Glycine transforms back to the γ-form via a, sixth, short-lived ζ-polymorph.[6] L-serine has four high-pressure polymorphs.[7-12] The ambient pressure form, L-serine I, transforms to L-serine II and III on rapid compression at *ca*. 5 and 8 GPa and to L-serine IV above 5.6 GPa on slow compression.[13] L-cysteine I transforms on compression above 1.8 GPa to give L-cysteine III and then again on decompression from 4.2 to 1.7 GPa to form L-cysteine IV.[14] Structural changes in L-α-glutamine were studied to 4.9 GPa but it does not undergo any phase transitions.[15] L-alanine also remains in the same ambient pressure phase on compression to 13.6 GPa but it undergoes reversible amorphisation at 15 GPa.[16-17] A summary of the discussion above is given in **Table 2.1**.

Table 2.1 A summary of phase transformations in some amino acids at high pressures.

Amino Acid	Starting Pressure (GPa)	Polymorph Label	Transformation conditions
Glycine ($C_2H_5NO_2$)	0	α	stable to 23 GPa.[3]
		β	β to δ at 0.8 GPa. [4–5]
		γ	γ to ε between 2.0 and 4.3 GPa. [4–5]
	2.0–4.3	ε	decompression yields ζ. [6]
L-serine ($C_3H_7NO_3$)	0	I	I to II at 5 GPa (rapid compression).[7–13] I to IV above 5.6 GPa (slow compression).[7–13]
	5	II	II to III at 8 GPa (rapid compression).[7–13]
L-cysteine ($C_3H_7NO_2S$)	0	I	I to III above 1.8 GPa.[14]
	4.2	III	III to IV on decompression to 1.7 GPa.[14]
	0	II	Unknown. No pressure data reported
L-α-glutamine ($C_5H_{10}N_2O_3$)	0	n/a	No transitions observed to 4.9 GPa.[15]
L-alanine ($C_3H_7NO_2$)	0	n/a	Ambient pressure phase stable to 13.6 GPa but amorphises at 15 GPa.[16–17]

The role of H-bonding and other non-bonding interactions are important in understanding phase stability as a structure evolves under compression to fill space more efficiently and avoid short repulsive contacts.[18] Crystallographic studies of complex molecular materials, however, rarely achieve pressures beyond 10 GPa. The Cambridge Structural Database (CSD) (v.5.40, November 2018) contains almost 3000 entries which specify the pressure of the structure determination, and a list of these is included in Microsoft Excel format in the ESI. There are 2561 entries determined at above 10 atm, and 2457 above 1000 atm (0.1 GPa). Only 14 molecular compounds have been studied above 10 GPa

(100 000 atm), only one of which is an amino acid, L-alanine (LALNIN51), whose structure was determined by powder methods at 13.6 GPa (see **Table S2.1**, ESI).[16] The highest pressure entry is that of CO_2 at 28 GPa (SACBAA) which was also obtained by powder diffraction; [19] the next highest pressure entry is that of benzene (BENZEN09) at 24 GPa but the entry lacks 3D coordinates.[20] The highest pressure entry in the CSD of a complex molecular compound, determined by single-crystal diffraction and with refined 3D coordinates is that of palladium (II) oxathioether (NONWES30) at *ca.* 14 GPa.[21]

A search of the Inorganic Crystal Structure Database (ICSD) for non-metal compounds at pressures greater than or equal to 10 GPa results in 187 hits. Amongst the molecular elements,[22-24] oxygen becomes metallic at 96 GPa.[25] The structure of a high-pressure phase of molecular nitrogen has been determined by single-crystal X-ray diffraction at 56 GPa,[23] and the structure of polymeric nitrogen, which forms at 110 GPa and 2000 K, has been determined using X-ray diffraction and Raman scattering at 115 GPa.[26]

Beyond the elements, there are 84 crystal structures of molecular solids at pressures greater than 10 GPa deposited in the ICSD, comprising 15 different compounds. Some notable examples include the single-crystal structure determinations of arsenolite and its helium clathrate to 30 GPa[27] and the van der Waals compound $Kr(H_2)_4$ whose structure was determined at 11.24 GPa.[28] Xenon difluoride has been studied by powder X-ray diffraction and computational methods and is shown to undergo two phase transitions at 28 and 59 GPa, with metallisation predicted to occur at 152 GPa.[29]

Although crystal structures of complex molecular solids above 10 GPa are quite rare, spectroscopic methods, particularly Raman spectroscopy, have been very useful in detecting phase transitions. This approach has been used extensively to study amino acids.[30] We now describe the crystal structure of L-threonine (**Figure 2.1**) to 22.3 GPa with the aim of identifying the structural

features associated with the three phase transitions which have been characterised by a series of Raman studies, most recently by Holanda *et al.*[31]

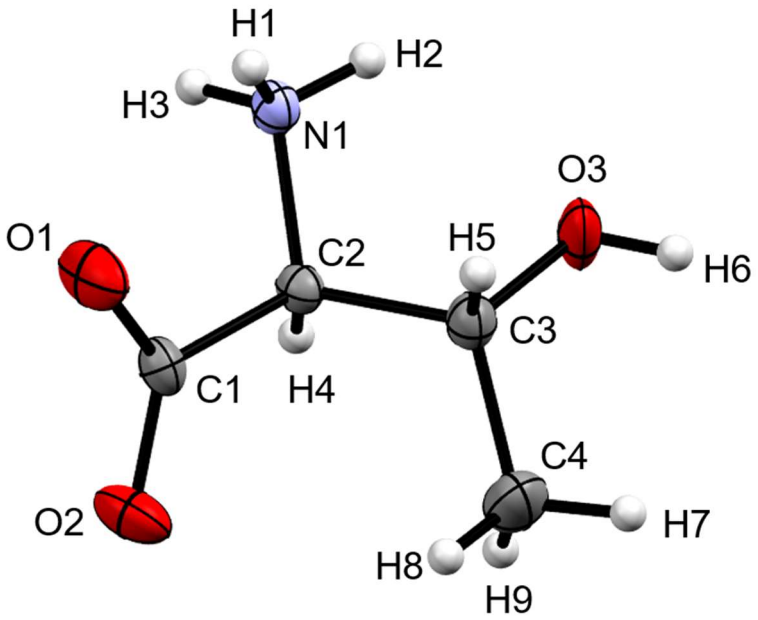

Figure 2.1 Molecular structure of L-threonine at ambient conditions showing the numbering scheme used. Ellipsoids are shown at the 50 % probability level.

2.2. Experimental

2.2.1. X-Ray Crystallography

L-threonine (99% Sigma-Aldrich) was recrystallised from a 656 mM ethanol solution by slow evaporation; forming colourless, blade-shaped crystals. Single-crystal diffraction data were collected at ambient pressure and room temperature using a cut crystal measuring 0.2 x 0.2 x 0.1 mm³ on a Bruker 3-circle goniometer APEX-II diffractometer using Mo-Kα radiation (λ=0.71073 Å). Below 7 GPa diffraction data were measured at room temperature using silicon (111) monochromated synchrotron radiation (λ=0.4780 Å) on Station 9.8 at the Synchrotron Radiation Source, Daresbury, UK. A single crystal of L-threonine measuring *ca.* 0.1 mm³ was loaded in a Merrill-Bassett type diamond anvil cell (DAC) along with a ruby chip in 4:1 methanol-ethanol as a pressure-transmitting medium.[32-33] A total of six diffraction measurements were carried out between 1.26 to 6.67 GPa using a Bruker-Nonius APEX II diffractometer following the collection strategy of Dawson *et al*.[34]

Single-crystal diffraction data between 4.0 and 22.3 GPa were measured at room temperature on Beamline 12.2.2 at the Advanced Light Source in Berkeley, California, USA, which has been described in detail elsewhere.[35-36] Crystals measuring *ca.* 50 μm³ were cut from larger single crystals and mounted with a ruby sphere in a BX-90 type DAC[37] consisting of 500 μm Boehler-Almax cut diamonds mounted in tungsten-carbide backing seats.[38] The rhenium gasket hole had an initial diameter 320 μm and thickness of *ca.* 70 μm. The cell was gas-loaded in neon using a GSECARS/COMPRES gas-loader[39] at the Advanced Light Source. Data were collected in steps of approximately 1.4 GPa; and on decompression at 13.0 GPa on a custom-built Huber diffractometer with silicon (111) monochromated synchrotron radiation (λ=0.4959 Å) and a Perkin-Elmer amorphous silicon detector, using a combination of shutterless ϕ-scans at 0.25° and 1° step-widths across the half-opening angle (±40°) of the sample chamber and cell body. Additional low-pressure measurements were performed in the same manner from 2.6 to 5.9 GPa on a separate sample.

In all cases, pressure was measured using the ruby fluorescence method.[40]

2.2.2. Structure Analysis

Diffraction data were processed using the APEX3 suite of programs.[41] Data reduction was carried out using SAINT,[42] employing dynamic masks generated by ECLIPSE[43] to mask shaded detector areas. Absorption and shading corrections were applied using the multi-scan procedure SADABS.[43] Data-sets were initially analysed using XPREP,[44] the structures at ambient pressure and following a phase transition at 18.2 GPa were solved using dual space methods (SHELXT)[45] and then refined by full-matrix least-squares on $|F|^2$ (SHELXL)[46] using the ShelXLe graphical user interface.[47] Otherwise refinements started from the atomic coordinates of the preceding pressure point.

There is a single-crystal to single-crystal phase transition at 18.2 GPa which reduces the space group symmetry from $P2_12_12_1$, to $P2_1$, although the unit cell metrics are similar either side of the transition. The structure was modelled with a two-fold axis about **a** as a twin law, but the twin fraction refined to 0.05(5). The orthorhombic cells of the structure below 18.2 GPa were placed in a non-standard setting to match that of the monoclinic phase in order to facilitate comparisons between phases.

Intramolecular bond distances in all high-pressure refinements were restrained to those of the ambient pressure structure. Data sets were modelled with isotropic displacement parameters in order to reduce the number of refined parameters. H-atoms were placed in calculated positions and allowed to ride on their parent atoms. The hydroxyl hydrogen atom was placed on the site forming the most favourable H-bond geometry while also being staggered with respect to O3-C3. The refinement and H-atom placement strategies are discussed below. Selected crystal and refinement data of structures in the different phases are collected in **Table 2.2.** A full set of parameters for all structures collected over the course of this study are available in the ESI (Table

S2.2). CCDC 1903563-1903583 contains the supplementary crystallographic data for this chapter.

2.2.3. Neutron Powder Diffraction at High Pressure

In order to improve the precision of the equation of state (EOS) of L-threonine and to corroborate the X-ray measurements, a series of neutron powder diffraction measurements was collected on compression from 0.00 to 8.77 GPa in steps of *ca.* 0.55 GPa using the PEARL instrument at the ISIS facility, Rutherford Appleton Labs, Didcot, UK. Deuterated L-threonine (CDN Isotopes, used as received) was loaded into a TiZr capsule gasket with a 4:1 mixture of deuterated methanol and ethanol, and a pellet of lead as a pressure marker. The sample was compressed using a type V3 Paris–Edinburgh cell with WC type anvils. Pressure measurements were obtained from the equation of state of lead.[48] Unit cell parameters were extracted by the Pawley method using TOPAS.[49]

2.2.4. PIXEL Energy Calculations

The PIXEL method is a semi-empirical computational technique for the calculation of lattice and intermolecular interaction energies in molecular crystal structures. The calculations are based on a pixelated model of the molecular electron densities within a cluster generated about a central reference molecule using the space group symmetry of the crystal structure. The interaction energies between the reference molecule and the other molecules in the cluster are obtained by summing the Coulombic, polarisation, dispersion and repulsion terms between individual electron density pixels. The sum of energies within the cluster gives the lattice energy, and this is broken down into individual molecule-molecule contributions. The energies are also broken down into constituent Coulombic, polarisation, dispersion and repulsion

contributions. Full details of the method and its application are available in references [8, 50-54].

In this study the cluster radius was 15 Å, and the molecular electron densities were obtained from GAUSSIAN-09[55] with the 6-31G** basis set at the MP2 level of theory. The PIXEL calculations themselves were accomplished with the CLP-PIXEL suite.[52] The electron densities were calculated on a grid of dimensions 0.08 x 0.08 x 0.08 $Å^3$, but in order to speed up subsequent energy calculations, blocks of 4 x 4 x 4 pixels were combined into superpixels (*i.e.* the *condensation level* was 4).

Individual intermolecular interaction energies obtained using PIXEL (and symmetry-adapted perturbation theory at the SAPT2+3 level, see below) are shown in **Table 2.3** at ambient pressure and 17.1 GPa. A breakdown of the lattice energy at each pressure and a comparison of relative energies with those calculated by DFT (see below) are given in **Tables S2.3** and **S2.4** of the ESI. Also available in the ESI are listings of contact energies at 18.2 GPa (**Tables S2.5** and **S2.6**) and plots showing dimers formed within the first coordination spheres at 0, 17.1 and 18.2 GPa in **Figures S2.1-4**)

2.2.5. Periodic Density Functional Theory (DFT) Calculations

Geometry optimisations were carried-out on the ambient pressure crystal structure as well as those at 3.97, 5.91, 6.12, 8.50, 9.82, 11.19, 13.94, 15.20, 15.78, 17.05, 18.20, 20.62 and 22.31 GPa, using the plane-wave pseudopotential method in the CASTEP[56] code as incorporated in Materials Studio.[57] The PBE exchange-correlation functional was used with the 'on the fly' pseudopotentials embedded in the program and the Tkatchenko-Scheffler correction for dispersion.[58] The basis set cut-off energy was 780 eV and Brillouin zone integrations were performed with a Monkhorst-Pack[59] **k**-point grid spacing of 0.07 $Å^{-1}$. These conditions gave a convergence in total energy of better than 1 meV/atom.

The starting coordinates for the optimisations were taken from the single-crystal X-ray diffraction structures with distances to hydrogen normalised to typical neutron values. The cell dimensions were fixed to the experimental values, and the space group symmetry was retained. In geometry optimisations the energy convergence criterion was $5x10^{-6}$ eV/atom, with a maximum force tolerance of 0.01 eV $Å^{-1}$ and a maximum displacement of $5x10^{-4}$ Å; the SCF convergence criterion was $1x10^{-8}$ eV/atom.

2.2.6. Symmetry-adapted Perturbation Theory (SAPT) Calculations

SAPT calculations were performed at the SAPT2+3 level of theory on dimers taken from the ambient pressure and 17.1 GPa structures using the PSI4 code (version 1.0.54) with the aug-cc-pvdz basis set.[60-61]

2.2.7. Other Programs Used

Geometric parameters were calculated using PLATON.[62] EoSFit7-GUI[63] was used for EOS calculations. OLEX2-1.2,[64] DIAMOND 3.0[65] and MERCURY (CCDC)[66] were used for structure visualisation. CONQUEST[67] was used to survey the CSD and MR_PIXEL[68] was used to facilitate setting-up of PIXEL calculations. Topology calculations were accomplished with TOPOSPRO.[69]

2.2.8. Validation of Computational Methods

In the following analysis, the results of PIXEL calculations are used to interpret the structural changes occurring on compression. The use of this method has been validated by comparison of the lattice energy of L-threonine with the experimental value, by comparing the total energies of the compressed structures with those obtained by DFT calculations, and finally by comparing individual molecule-molecule energies at ambient pressure and 17.1 GPa with values obtained with symmetry adapted perturbation theory.

The experimental enthalpy of sublimation of L-threonine is 161 kJ mol^{-1} at 298.15 K, [70] but once proton transfer between the ammonium and carboxylate groups during sublimation is taken into account,[71] the energy of sublimation of zwitterionic L-threonine is 270.7±7 kJ mol^{-1}, which compares with the PIXEL value of 252.0 kJ mol^{-1}.

The pressure-dependence of the lattice energy of L-threonine was calculated using the PIXEL method and periodic DFT (see Section 3.4.1 and **Table S2.4** in the ESI). The goodness-of-fit of the PIXEL calculated energies from ambient pressure to 22.3 GPa is 0.85, which improves to 0.93 if the highest-pressure structure is discounted.

Individual intermolecular interaction energies obtained using PIXEL and symmetry-adapted perturbation theory at the SAPT2+3 level are shown in **Table 2.3** at ambient pressure and 17.1 GPa. At ambient pressure the mean (and median) differences are 1.4(–6.8) kJ mol^{-1}; the corresponding figures at 17.1 GPa are –1.2 (1.3) kJ mol^{-1}. The largest difference at 17.1 GPa is in interaction G/H, for which the PIXEL and SAPT energies are –1.0 and +17.9 kJ mol^{-1}, respectively.

Table 2.2 Selected crystallographic information

Pressure (GPa)	**0.00**	**2.05**	**3.23**	**8.50**
Phase	**I**	**I**	**I'**	**I'**
Crystal data				
Crystal system, space group	Orthorhombic, $P2_12_12_1$	Orthorhombic, $P2_12_12_1$	Orthorhombic, $P2_12_12_1$	Orthorhombic, $P2_12_12_1$
Temperature (K)	298	296	296	298
a, *b*, *c* (Å)	5.1481 (1), 13.6138 (2), 7.7426 (1)	5.0359 (6), 13.462 (3), 7.2375 (16)	5.0055 (2), 13.4104 (9), 7.1162 (4)	4.879 (3), 13.135 (8), 6.658 (6)
α, β, γ (°)	90, 90, 90	90, 90, 90	90, 90, 90	90, 90, 90
V (Å^3)	542.64 (2)	490.67 (16)	477.68 (5)	426.7 (5)
Radiation type	Mo *K*α	Synchrotron, λ = 0.4780 Å	Synchrotron, λ = 0.4780 Å	Synchrotron, λ = 0.4959 Å
μ (mm^{-1})	0.12	0.07	0.07	0.08
Crystal size (mm)	0.20 × 0.10 × 0.10	0.10 × 0.10 × 0.10	0.10 × 0.10 × 0.10	0.06 × 0.05 × 0.04
Data collection				
Diffractometer	Bruker *APEX* II CCD	Bruker-Nonius *APEX* II	Bruker-Nonius *APEX* II	Perkin-Elmer a-Si Detector
Absorption correction	Multi-scan	Multi-scan	Multi-scan	Multi-scan
T_{min}, T_{max}	0.676, 0.745	0.604, 0.744	0.629, 0.744	0.453, 0.744
No. of measured, independent and observed [$I > 2\sigma(I)$] reflections	5775, 1123, 1065	2455, 627, 542	2848, 738, 684	766, 227, 192
R_{int}	0.025	0.055	0.041	0.089
θ_{max} (°)	26.4	17.5	17.4	14.4
$(\sin\theta/\lambda)_{max}$ (Å^{-1})	0.625	0.628	0.625	0.500
Refinement				
$R[F^2 > 2\sigma(F^2)]$, $wR(F^2)$, S	0.026, 0.070, 0.82	0.064, 0.151, 1.09	0.062, 0.152, 1.05	0.062, 0.142, 1.08
No. of parameters	76	33	33	34
No. of restraints	0	17	17	17
$\Delta\rho_{max}$, $\Delta\rho_{min}$ (e Å^{-3})	0.18, -0.13	0.33, -0.27	0.42, -0.31	0.26, -0.23

Table 2.2 Continued

Pressure (GPa)	**9.28**	**17.05**	**18.20**	**22.31**
Phase	**II**	**II**	**III**	**III**
Crystal data				
Crystal system, space group	Orthorhombic, $P2_12_12_1$	Orthorhombic, $P2_12_12_1$	Monoclinic, $P2_1$	Monoclinic, $P2_1$
Temperature (K)	298	298	298	298
a, b, c (Å)	4.842 (6), 13.025 (17), 6.589 (12)	4.768 (4), 12.883 (10), 6.353 (7)	4.735 (5), 12.823 (13), 6.275 (8)	4.620 (9), 12.52 (2), 6.037 (14)
α, β, γ (°)	90, 90, 90	90, 90, 90	90, 91.14 (3), 90	90, 92.54 (4), 90
V (Å^3)	415.5 (11)	390.2 (6)	380.9 (8)	348.9 (12)
Radiation type	Synchrotron, λ = 0.4959 Å	Synchrotron, λ = 0.4959 Å	Synchrotron, λ = 0.4959 Å	Synchrotron, λ = 0.4959 Å
μ (mm^{-1})	0.08	0.09	0.09	0.10
Crystal size (mm)	0.06 × 0.05 × 0.04	0.06 × 0.05 × 0.04	0.06 × 0.05 × 0.04	0.06 × 0.05 × 0.04
Data collection				
Diffractometer	Perkin-Elmer a-Si Detector	Perkin-Elmer a-Si Detector	Perkin-Elmer a-Si Detector	Perkin-Elmer a-Si Detector
Absorption correction	Multi-scan	Multi-scan	Multi-scan	Multi-scan
T_{min}, T_{max}	0.555, 0.744	0.408, 0.744	0.463, 0.744	0.610, 0.744
No. of measured, independent and observed [$I > 2\sigma(I)$] reflections	711, 329, 194	1101, 331, 208	901, 378, 305	334, 183, 156
R_{int}	0.100	0.070	0.055	0.061
θ_{max} (°)	18.1	18.1	16.1	14.3
$(\sin\theta/\lambda)_{max}$ (Å^{-1})	0.625	0.627	0.558	0.499
Refinement				
$R[F^2 > 2\sigma(F^2)]$, $wR(F^2)$, S	0.091, 0.245, 1.05	0.086, 0.228, 1.11	0.078, 0.192, 1.05	0.079, 0.196, 1.15
No. of parameters	34	33	67	66
No. of restraints	17	17	51	51
$\Delta\rho_{max}$, $\Delta\rho_{min}$ (e Å^{-3})	0.36, -0.36	0.31, -0.34	0.30, -0.27	0.24, -0.30

Table 2.3 Interactions in the first coordination sphere of L-threonine at 0.0 and 17.05 GPa. The 12 molecules in the first coordination spheres are labelled A–N in order of increasing energy. All energies are in kJ mol^{-1}. Contact distances are to H-atoms. Symmetry equivalent pairs of molecules are listed together *e.g.* Molecules A and B are listed as A/B.

			Centroid	PIXEL					SAPT 2+3	
Label	Symmetry	Pressure (GPa)	Distance (Å)	Coulombic	Polarization	Dispersion	Repulsion	Total	Total	Contacts
A/B	1/2–x, 1–y, 1/2+z	0.00	5.555	–93.9	–30.3	–20.3	38.7	–105.8	–119.3	N1H3···O2 = 1.94 Å
	1/2–x, 1–y, –1/2+z	17.05	4.960	–150.7	–58.4	–41.9	144.8	–106.2	–118.4	N1H3···O2 = 1.98 Å
C/D	1–x, –1/2+y, 3/2–z	0.00	6.965	–82.6	–32.6	–11.7	71.8	–55.1	–59.9	O3H6···O1 = 1.87 Å
	1–x, 1/2+y, 3/2–z	17.05	6.583	–109.4	–51.5	–17.4	137.7	–40.6	–43.8	O3H6···O1 = 1.73 Å
E/F	3/2–x, 1–y, 1/2+z	0.00	6.432	–41.7	–8.7	–7.3	4.7	–53.0	–55.6	N1H3···O1 = 2.65 Å
	3/2–x, 1–y, –1/2+z	17.05	5.633	–101.3	–35.7	–22.9	73.9	–86.0	–85.5	O1···H3(N1)/H2(N1) = 1.92/2.50 Å
G/H	1+x, y, z	0.00	5.148	–23.5	–27.0	–20.9	37.7	–33.6	–26.8	N1H1···O2 = 2.04 Å
	–1+x, y, z	17.05	4.768	–51.0	–58.7	–44.5	153.1	–1.0	17.9	N1H1···O2 = 1.83 Å
I/J	–x, 1/2+y, 3/2–y	0.00	8.031	–9.4	–2.5	–1.9	0.1	–13.7	–13.4	C4H7···O2 = 3.59 Å
	–x, –1/2+y, 3/2–y	17.05	7.677	–10.4	–4.4	–3.5	1.7	–16.6	–18.1	C4H7···O2 = 2.97 Å
K/L	1/2+x, 1/2–y, 1–z	0.00	4.934	–3.6	–12.9	–21.9	29.4	–9.0	–5.6	N1H2···O3 = 2.31 Å
	–1/2+x, 1/2–y, 1–z	17.05	4.344	–49.8	–47.3	–47.7	153.5	8.5	19.3	N1H2···O3 = 2.04 Å
M/N	–1/2+x, 1/2–y, 2–z	0.00	6.391	–5.0	–2.7	–9.9	8.5	–9.0	–8.3	C4H7···H5(C3) = 2.42 Å
	1/2+x, 1/2–y, 2–z	17.05	5.767	–16.5	–17.3	–22.8	64.0	7.3	2.5	C4H7···H5(C3) = 1.88 Å

2.3. Results & Discussion

2.3.1. Phase Behaviour

The X-ray crystal structure of L-threonine was first determined by Shoemaker in 1950.[72] It exists as a zwitterion in the solid–state with charged carboxylate and ammonium groups situated on the α-carbon (C2) and a hydroxyl and methyl group on the β-carbon (C3) with the chemical formula $C_4H_9NO_3$. L-threonine crystallises in the space group $P2_12_12_1$ with four molecules in the unit cell (Z' = 1) at ambient pressure and temperature, with the unit cell parameters: a=5.1481(1) Å, b=13.6138(2) Å, c=7.7426(1) Å and V= 542.64(2) Å^3. The atom labelling, which follows Shoemaker's work, is given in **Figure 2.1**.

The phase behaviour of L-threonine has been most recently studied using Raman spectroscopy by Holanda *et al.*, who inferred three structural phase transitions at *ca.*2 GPa, between 8.2 and 9.2 GPa and between 14.0 and 15.5 GPa based on changes in the slopes of frequency-pressure plots and the splitting, appearance or disappearance of bands.[31] We shall label the phases formed in these transitions I', II and III, respectively. Over the course of this and two earlier Raman studies, the transition to phase I' had been observed between 1.1 and 1.6 GPa,[31] at 1.9 GPa (in D-threonine)[73] and at 2.2 GPa,[74] the authors ascribing these differences to the influence of the different pressure-transmitting media used in the three studies (methanol-ethanol, Nujol and argon).

The variation of the refined unit cell volume and dimensions with pressure is shown in **Figure 2.2**. The structure remains orthorhombic, space group $P2_12_12_1$, from ambient pressure to 17.1 GPa, *i.e.* throughout the range for phases I, I' and II,[31] and it is clear that the structures of these phases are very closely related.

The discontinuity between 17.1 and 18.2 GPa, observed in all four curves, corresponds to the transition from phase II to III, which occurred between 14.0 and 15.5 GPa in Holanda's study. The difference in the transition pressure may, as these authors suggest, be the result of the influence of the pressure-

transmitting medium (Ne in our case). Alternatively, it may reflect the sensitivity of spectroscopic methods to local structural changes, as was the case in [Cu(pyrazine)(H_2O)$_2F_2$], where premonitory disordering of Jahn-Teller directions, observed by high pressure electron paramagnetic resonance, was not evident in the average structure obtained by analysis of Bragg scattering in single-crystal diffraction measurements.[75]

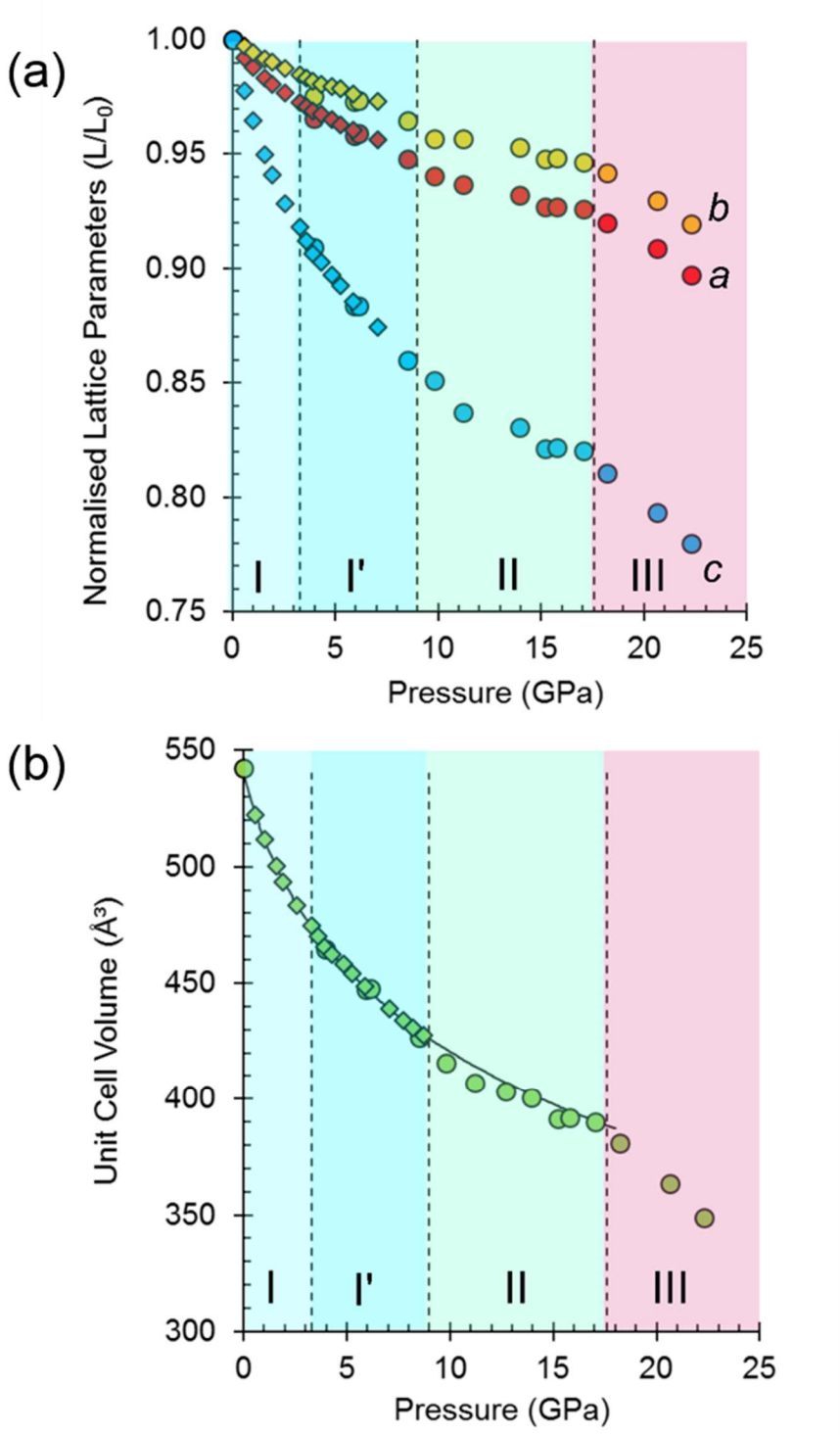

Figure 2.2 Variation of **(a)** the normalised lattice parameters and **(b)** unit cell volume of L-threonine as a function of pressure. Neutron data, collected using the d_8 isotopologue, are shown as diamonds. X-ray diffraction data, collected using isotopically normal threonine, are shown as circles. There is little evidence of any isotopic effect at the resolution of these experiments. The curve is the equation of state of phase I and I'. The I', II and III phase boundaries determined in this study are shown as dashed lines and each region is coloured to help guide the eye (phases were initially inferred from Holanda's study [ref. 31]). Error bars are obscured by the data points.

At 17.1 GPa the unit cell dimensions of phase II are a = 4.768(4), b = 12.883(10), c = 6.353(7) Å, V = 390.2(6) Å^3, representing a volume reduction of 28 % compared to the ambient-pressure structure. The cell dimensions after the transition to phase III at 18.2 GPa are a = 4.735(5), b = 12.823 (13), c = 6.275(8) Å, β = 91.14(3)°, V = 380.9 (8) Å^3, so that after the phase transition, although the 2_1 operations along the a and c directions are lost, the translational symmetry of the lattice is preserved and Z is still equal to four, but Z' = 2. The structure remains in phase III up to 22.3 GPa, the highest pressure reached in this study. At 22.3 GPa the unit cell volume is 348.9(12) Å^3, representing a 36 % reduction compared to ambient pressure. Pressure release from 22.3 GPa to 13.0 GPa re-forms phase II. Further X-ray decompression measurements were not performed, but Holanda's Raman measurements indicate full reversibility from 27 GPa to ambient pressure.

Fitting the pressure-volume data of L-threonine-d_9 I and I' obtained in the neutron powder diffraction experiment to a Vinet equation of state[76] gives values of the bulk modulus (K_0) and its first derivative (K') of 15.23(8) GPa and 7.97(6), respectively. The zero-pressure volume in this fit was fixed to 540.236 Å^3 and χ^2 was 1.94. The bulk modulus of L-threonine is comparable to other hydrogen bonded amino acids, *e.g.* L-serine I is 23.4 GPa and those of polymorphs II and III are 14.7 and 13.9 GPa;[77] and that of L-alanine is 13.1(6) GPa.[16]

Superposition of the equation of state curve on all the pressure-volume points collected in this study between ambient pressure and 17.1 GPa shows the points between 9.8 and 17.1 GPa lie to systematically lower volume, pointing to the formation of phase II between 8.7 and 9.8 GPa. This is consistent with the phase I' to II transition observed between 8.2 and 9.2 GPa by Holanda *et al.*,[31] albeit with a more subtle signature than the transition to phase III. The transition is also marked by a small discontinuity in the b-axis length [**Figure 2.2(a)**].

It will be seen from **Figure 2.2(b)** that all the points between ambient pressure and 8.7 GPa are consistent with the same equation of state, and there appears to be little indication in the plots for the I to I' transition proposed by Holanda *et al.* near 2 GPa (see also below).

2.3.2. The Effects of Pressure on the Intramolecular Structure

High pressure data sets almost always suffer from low completeness as a result of the limited scattering geometry of the diamond anvil cell. Accordingly, the data-sets of threonine-I, I' and II collected here had completenesses of between 43 and 73 %, the corresponding figures for the lower symmetry phase III were 32–45 %. As a result, it is usually necessary to place restraints on the structure refinements, and bond distances and angles were restrained to values observed at ambient pressure.

In order to assess the suitability of the restraints applied, the structures of phase I at ambient pressure and phase III at 22.3 GPa were optimised by periodic DFT. The calculations indicated that bond distances change by as much as 0.071 Å, and bond angles by 5.43° (see **Table S2.7** in the ESI), while the root-mean-square deviations between the optimised and experimental molecular structures were 0.0284 and 0.131 Å, respectively (see **Tables S9** and **S10** in the ESI, which also contains further comparison data). Use of the optimised model as a freely rotating rigid body in the refinement against the 22.3 GPa data set lowered the *R*-factor, but only slightly (0.17 % for 183 reflections), so that it is not possible to state definitively whether the intramolecular bond distances and angles are significantly affected by pressure, as the differences are beyond the resolution of the data obtained in this study. By contrast, the torsion angles do vary significantly with pressure. **Figure 2.3** shows differences in conformation between the ambient pressure and highest-pressure molecular structures, with differences apparent about the carboxylate, hydroxyl and methyl groups. Holanda *et al.* noted that the most prominent changes in the Raman spectra of threonine with pressure were associated with

vibrations of the carboxylate moiety. The variation of the orientation of the carboxylate group with pressure, represented by the O2-C1-C2-C3 torsion angle (τ), is shown in **Figure 2.4**. The features in these plots correlate with the phase transitions suggested by Holanda *et al*. and is described in Section 2.3.1

Between 0.0 and 2.1 GPa τ decreases from –83.2(2)° to –85.3(6)°, but this trend appears to reverse between 2.1 and 3 GPa. These changes are small, but the pressure at which they occur is the same as the I to I' transition inferred from the Raman data. The small magnitude of the change is consistent with lack of any obvious signature in the cell dimensions or volume at this pressure.

Beyond 3 GPa the value of τ continues to become more positive, but between 8.5 and 9.8 GPa it changes dramatically from –82(1)° to –76(2)°, the trend flattening-off again between 9.8 and 17.1 GPa. These changes coincide with the transition from phase I' to II. The standard uncertainties of τ become large above the phase II to III transition at 17.1 GPa. However, with the change in *Z'* from 1 to 2, it appears that the value continues to become gradually more positive in one molecule (molecule B) but more negative in the other.

Although H-atoms could not be located in difference maps, the changes in the positions of acceptor atoms imply that there is also a change in the orientation of the hydroxyl moiety over the course of the II to III transition. Hydrogen atoms were placed in calculated positions (see Section 2.2.2.) and based on this approach the torsion C4-C3-O3-H6 changes from –50° in phase II to –60° in molecule A, and to –78° in molecule B in phase III. The change in the position of H6 is also seen in DFT optimisations, but is less pronounced (**Table S2.11** and **Figure S2.8** in ESI); the corresponding torsional changes over the course of the II to III transition are: –45 to –41° and –47° in molecules A and B, respectively. The implications of the change in position of H6 are discussed in Section 2.3.4.3.

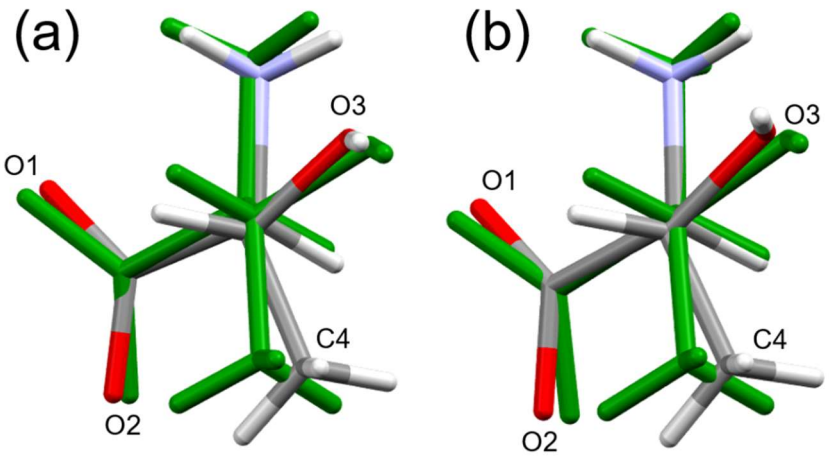

Figure 2.3 Structure overlay of the two symmetry-independent molecules of threonine at 22.3 GPa (coloured by element) [(a) molecule A and (b) molecule B] with the molecule at ambient pressure (coloured green). The view is down the C3-C2 bond. Overlay of the structures was determined using the structure overlay feature in MERCURY from atoms C1, C2 and C3 only.

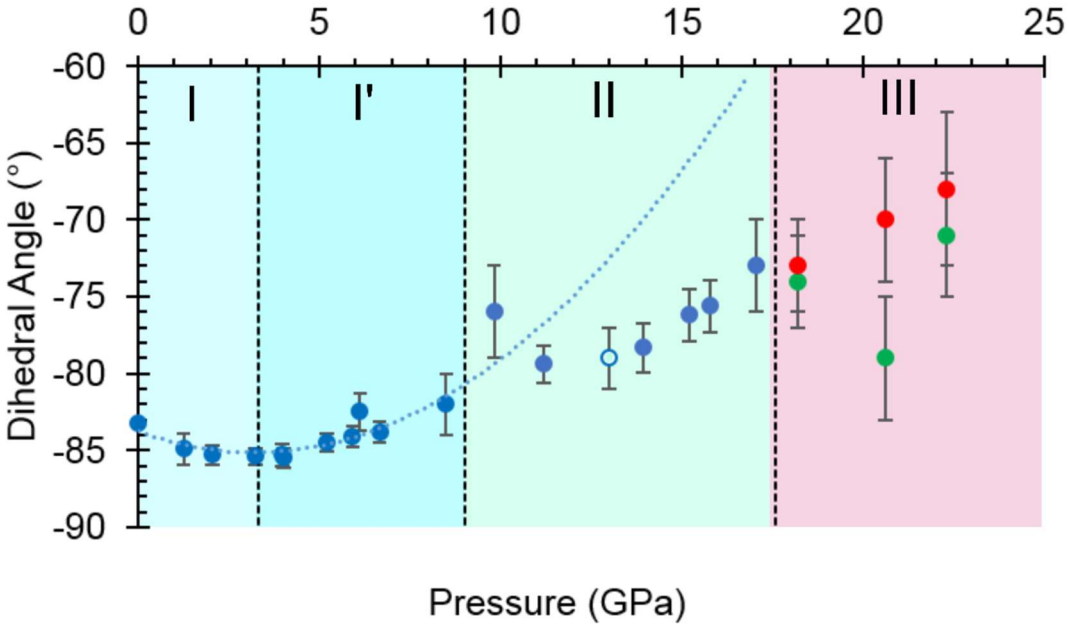

Figure 2.4 The O2-C1-C2-C3 torsion angle (τ) as a function of pressure. The green and red circles in phase III represent molecules A and B, and the open circle represents the decompression measurement. A second order polynomial was fitted to phase I and I' data, the minimum of the parabolic function was determined to be –85.0° at 3.3 GPa. Extrapolating the curve to 17.1 GPa serves to highlight the slower rate of change exhibited in phase II. Plots of other torsion angles against pressure are available in the ESI.

2.3.3. Intermolecular Interactions at Ambient Pressure

Intermolecular interaction energies in phase I at ambient pressure are listed in **Table 2.3**, where contacts are ordered by interaction energy and grouped in symmetry-equivalent pairs. **Table 2.3** also lists the breakdown of the molecule-molecule energies into component Coulombic, polarization, dispersion and repulsion terms obtained from the PIXEL calculations. Validation of the PIXEL results against those of other methods is described in Section 2.8. Given that the PIXEL method is semi-empirical and developed using ambient-pressure structural and thermodynamic data, the level of agreement with other methods is remarkable.

The strongest contacts comprising four pairs of crystallographically unique interactions labelled A/B–G/H. The strongest (A/B; –105.8 kJ mol^{-1}) involves molecules connected by N1H3···O2 hydrogen bonds, with a hydrogen-acceptor separation of 1.94 Å forming a primary-level *C*(5) chain which runs along **c**. Interactions G and H involving N1H1···O2 hydrogen bonds (2.04 Å, –33.6 kJ mol^{-1}) form a second primary-level *C*(5) chain which runs along **a**. The

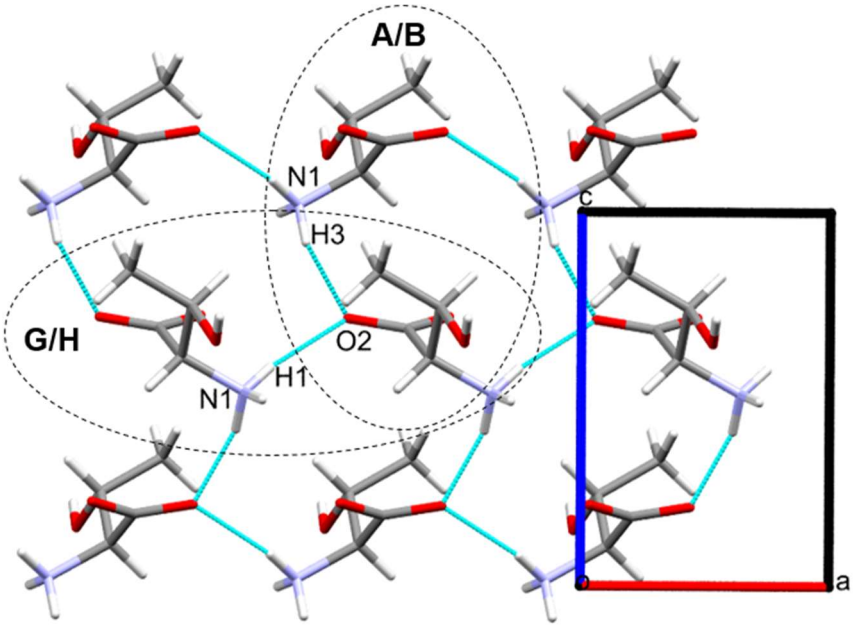

Figure 2.5 Hydrogen bonding in L-threonine at ambient pressure as viewed along **b.** Dimer pairs A/B and G/H are highlighted in black dashed ellipsoids.

combination of these two *C*(5) chains generates a layer in the *ac* plane (**Figure 2.5**).

The third dimension of the H-bond network is completed by *C*(6) chains formed by O3H6···O1 hydrogen bonds between the carboxylate and hydroxyl groups along **b**, see **Figure 2.6** [interaction C/D in **Table 2.3**, the hydrogen-acceptor distance is 1.87 Å and the energy is –55.1 kJ mol^{-1}]. This is the second most stabilising interaction in the ambient pressure structure. The Coulombic interaction is almost as strong as in the A/B contacts (–82.6 versus –93.9 kJ mol^{-1}), but the repulsion term is also much more positive (+71.8 versus 38.7 kJ mol^{-1}), so that, paradoxically, the interaction with the shorter H-bond is also the less stabilising.

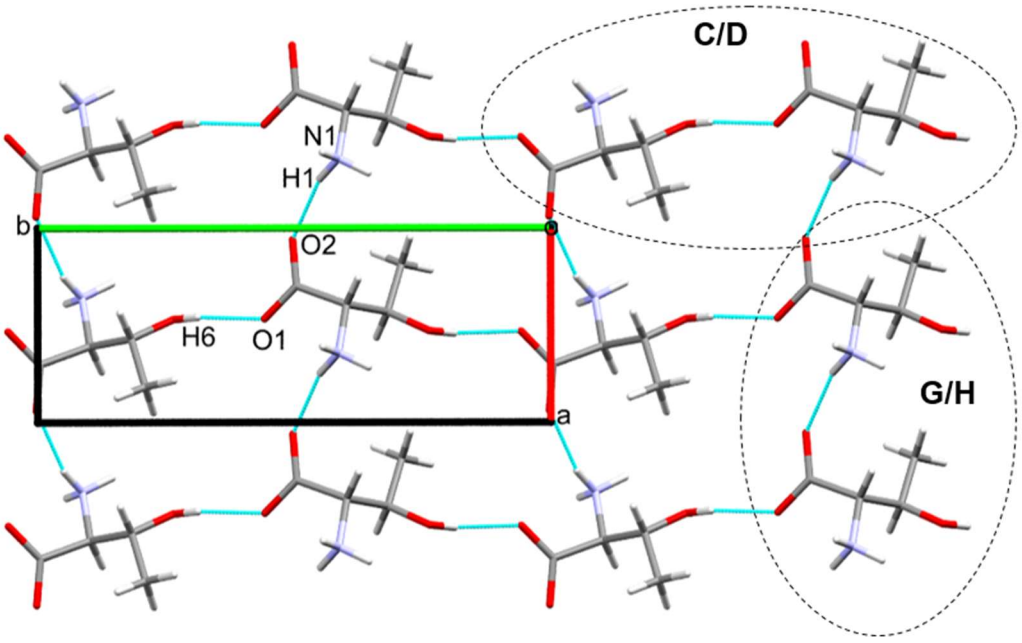

Figure 2.6 Hydrogen bonding in L-threonine at ambient pressure, as viewed along **c**. Dimer pairs C/D and G/H are highlighted in black dashed ellipsoids.

Interactions E and F are strongly stabilising, with an energy of –53.0 kJ mol^{-1} but featuring a rather long N1H3···O1 contact of 2.65 Å with a <N1H3···O1 angle of only 110.4°. This angle is too tight for a H-bond,[78] and the component energies show that the interaction is predominantly Coulombic

with a much smaller dispersion contribution than the hydrogen bonds described above. The contact is therefore better regarded as a long-range intra-layer electrostatic contact than a hydrogen bond. This interaction has an important influence on the compression of L-threonine, as described in the following section.

The hydrogen bonding scheme described above appears to leave the potentially strong donor N1H2 unbound. There is an additional *C*(5) chain connected by N1H2···O3 interactions (labelled K and L in **Table 2.3**) though the DH···X separation is quite long at 2.31 Å. The contact has a modest Coulombic component and is dominated by the dispersion term. It has an interaction energy of only –9.0 kJ mol^{-1}. The low value of the Coulombic contribution can be ascribed to the juxtaposition of both positive and negative regions of the electrostatic potentials of the contacting molecules.

In addition to the contacts listed above there are two pairs of longer-range interactions (I/J and M/N) with energies of –13.7 and –9.0 kJ mol^{-1} and H···O distances of between 3.59 and 2.42 Å. Topological analysis based on Voronoi-Dirichlet partitioning indicates that interactions I/J lie outside the first coordination sphere, a finding consistent with the low contributions of dispersion and repulsion to the energy of this interaction. The molecular centroids define a coordination sequence of 12-42-92, which is characteristic of an underlying face centred cubic topology. This arrangement persists at high pressure. Plots of the first coordination spheres at 0, 17.1 and 18.2 GPa are given in **Figure S2.5** in the ESI.

2.3.4. The Effects of Pressure on Intermolecular Interactions

2.3.4.1. The Effect of Pressure on The Lattice Energy

The effect of pressure on the lattice energy of L-threonine is shown in **Figure 2.7**, the points being calculated using the PIXEL method and periodic DFT.

In phases I, I' and II the lattice energies increase steadily with increasing pressure, which is expected as repulsion contributions increase as molecules are

forced into close proximity. There is a discontinuity in the gradient at the II to III phase transition at 18.2 GPa leading to a sharp destabilisation of the lattice energy. Examination of the contributions of the interactions in the first coordination sphere to the lattice energy (**Figure 2.8**) shows that all except the symmetry-related pair E and F are driven into destabilising regions of their potentials, that of the strongest H-bonding interaction A/B being particularly steep.

Based on the trends seen in **Figure 2.7**, the lattice energy of phase II at 18.2 GPa would be expected to be approximately –126 kJ mol^{-1}, compared to –124.9 kJ mol^{-1} for the observed phase III. Although phase III is less stable than phase II in terms of internal energy, at 18.2 GPa, the difference in molecular volume is 2.3 Å^3. This figure, though apparently modest, contributes a $p\Delta V$ term of –25 kJ mol^{-1} to the free energy change of the transition, which more than compensates for the change in lattice energy. Like most high-pressure phase transitions, therefore, the II to III transition in threonine is driven by the need to fill space efficiently at high pressure.

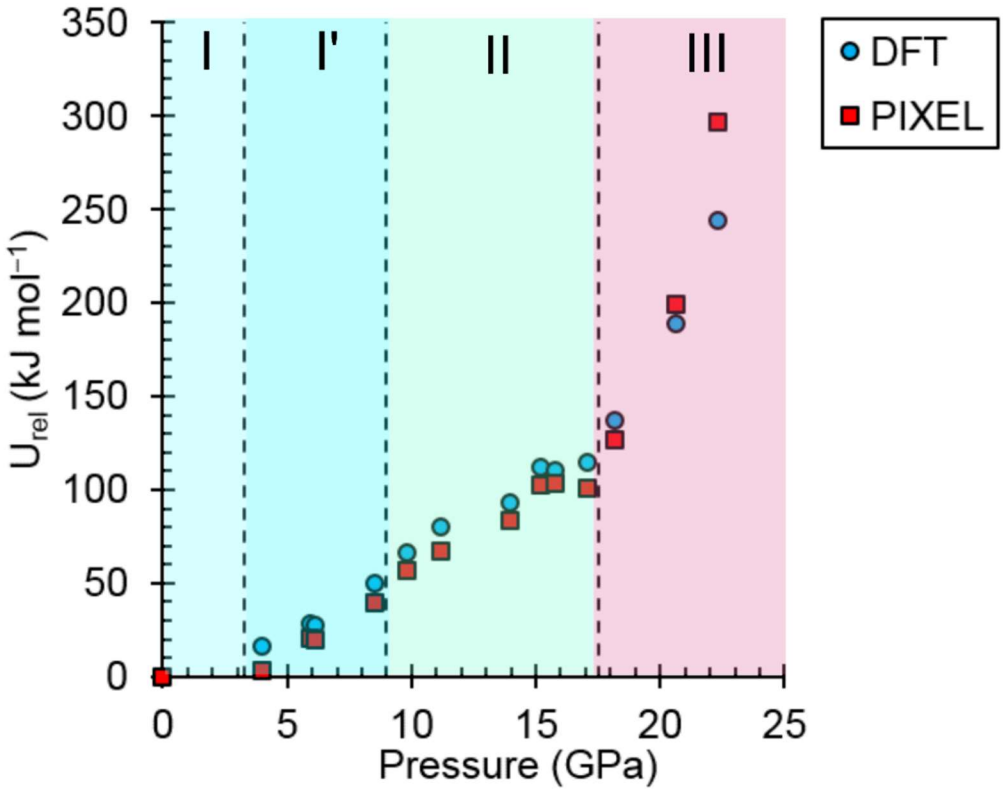

Figure 2.7 The variation of the lattice energy of threonine with pressure. The points are relative to ambient pressure (U_{rel}).

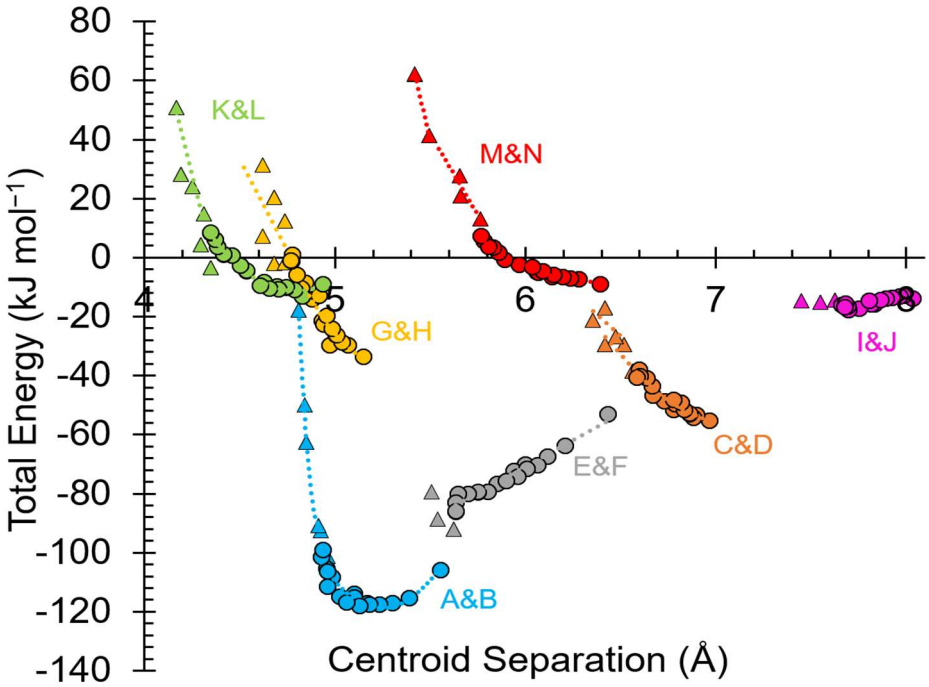

Figure 2.8 Molecular interaction energies of contacts A-N as a function of centroid separation. Circles represent phases I to II ($P2_12_12_1$), and triangles represent phase III ($P2_1$). The dotted lines have no functional significance and are meant to guide the eye.

2.3.4.2. The Effect of Pressure on Intermolecular Interactions in the ac Planes

An animation showing the path of compression of the layers formed in the *ac* planes is available in the ESI, while plots of the selected interaction distances against pressure are given in **Figures 2.9 (a)–(d)**.

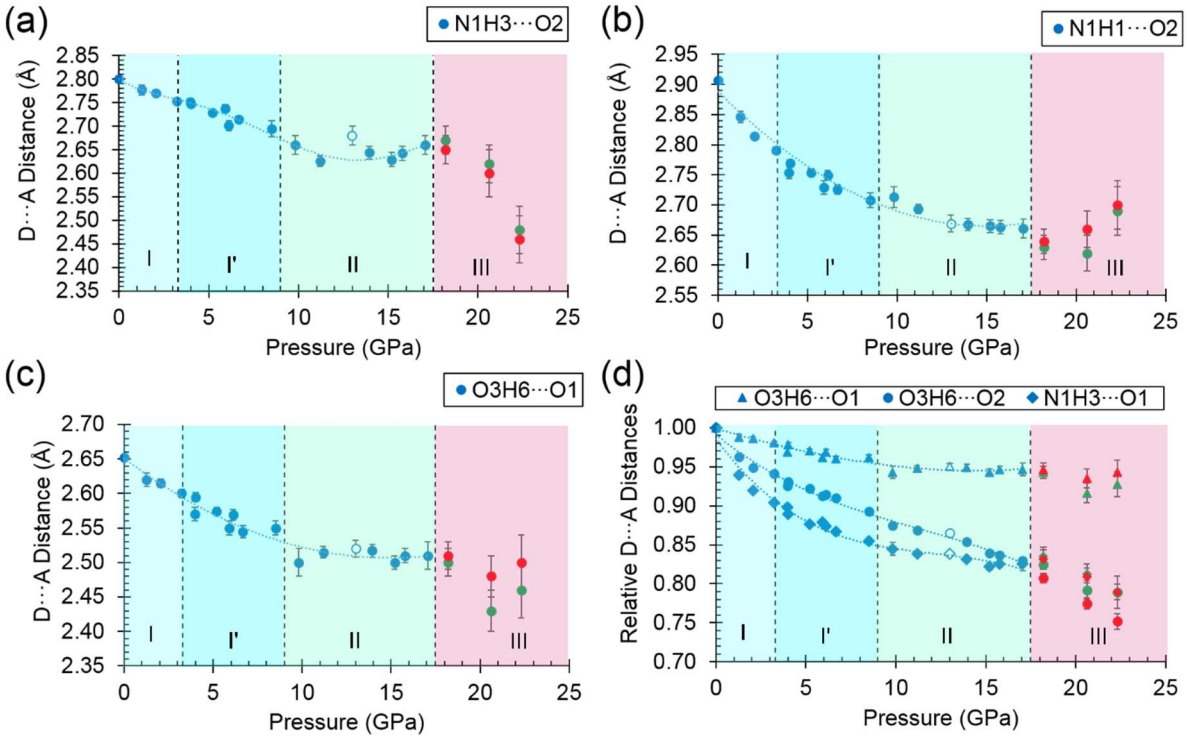

Figure 2.9 (a)–(d) Donor–acceptor distances of selected hydrogen bonds as a function of pressure, Decompression measurements at 13.0 GPa are represented by open markers. Molecules A and B in phase III are represented by green and red markers respectively. Trendlines are meant to guide the eye only.

By far the biggest change within the *ac* layers occurs in interaction E/F. Between 0 and 9.82 GPa the N1H3···O1 distance in this interaction changes from 2.65 Å to 2.03 Å. The N1H3···O2 distance of interaction A/B barely varies over the same pressure range. The angles subtended at H3 in the two interactions are respectively 110.4 and 162.7° at ambient pressure and 120.9° and 136.2° at 9.8 GPa. Interactions E/F thus change from being long-range Coulombic contacts at ambient pressure to ones mediated by a bifurcated H-bond at 9.8 GPa.

The change can be viewed as the positively-charged H3 adjusting its position within the large and strongly negative region of the combined

electrostatic potentials of the molecules involved in interactions A/B and E/F. The interaction energy becomes simultaneously more negative, the only stabilising change to occur on compression, providing a lower energy pathway for the structure to accommodate compression. Since interactions E and F are generated by a screw axis along **c**, the *c*-axis compresses substantially more than either the *a* or *b*-axes (**Figure 2.2(a)**). The gradual bifurcation of H3 reflects Holanda and co-workers' comment that the I' to II transition is the final result of a long process which affects the carboxylate rocking motion from about *ca.* 4.8 GPa.[31] Crystallographically, we can see that by this stage the H3···O1 distance is already around 2.3 Å.

While the principal structural effect of the I' to II transition is seen in interactions E/F, effects are also seen in the other interactions formed in the *ac* plane. The H-bonded dimers A/B are also slightly stabilised by the bifurcation of H3 while in phase I', but the energy begins to increase rapidly after the I' to II phase transition. Similar comments apply to interactions G/H, which actually becomes repulsive in phase III.

The lengths of the *a* and *c* axes undergo more rapid compression after the II to III transition. The animation of the pressure series shows that the loss of the 2_1 axes along *a* and *c,* which occurs during the transition, enables neighbouring rows of molecules linked by N1H3···O2 to shift in alternate directions enabling them to approach more closely, and the molecules to pack more efficiently. The lowering of symmetry illustrates Dove's comment that high-pressure phase transitions generally favour distorted phases in order to maximise density.[79]

2.3.4.3. Interactions Between the ac Planes

An animation showing the path of compression of the layers formed in the *ab* planes is available in the ESI. The layers which form parallel to the *ac* planes are connected by O3H6···O1 H-bonds between the hydroxyl and carboxylate groups

(interactions C/D), and a plot of the interaction distance against pressure is shown in **Figure 2.9 (c)**.

The C/D interaction energy does not show any initial stabilisation with pressure, in contrast to interactions A/B and E/F, a consequence, perhaps, of the repulsion term, which is appreciable even at ambient pressure. The energy becomes more positive as the pressure increases and does not exhibit any major discontinuities at the phase transitions.

The O3H6···O1 H-bond shortens steadily from 1.87 Å at ambient pressure to 1.77 Å at 8.50 GPa. The distance between H6 and the O2 atom of the same carboxylate group falls below 3 Å at 8.50 GPa, but is still very unsymmetrical at this stage, the angles subtended at H6 to O1 and O2 being 158.4 and 129.5°, respectively. The transition from phase I' to II is marked by greater translational movement of the neighbouring rows generated by lattice repeats along **a** relative to each other. The compression of the O3H6···O2 H-bond begins to level-off at this point, to be replaced by an increasing bifurcation of H6. At 9.82 GPa the H6···O1 and O2 distances are 1.73 and 2.91 Å, and the corresponding angles at H6 are 156.9 and 128.5°. By 17.1 GPa the H6···O2 distance has shortened to 2.73 Å, though without much change in the other parameters (H6···O1 = 1.73 Å, angles at H6 are 128.3 and 159.6°). Thus, the phase I' to II transition is marked along the *b* axis by a change in the way that the structure accommodates the applied pressure.

The symmetry reduction that occurs in the phase II to III transition is marked by a change in the orientation of the hydroxyl group in half of the molecules. The molecules labelled A retain the conformation of phase II, while H6B become more clearly bifurcated, so that at 18.2 GPa the O3BH6B···O1B increases to 1.97 Å, O3BH6B···O2B decreases to 2.62 Å, and respective angles at H6B are 122.1 and 129.8°. The corresponding parameters for the 'A' molecules are like those in phase II: 1.77 Å, 2.70 Å, 146.8° and 129.5°. The structural signature of the II to III transition is thus similar to the I' to II transition in that it involves the bifurcation of a hydrogen bond. The difference between the

transitions is that the change occurs in one pressure step, rather than being gradual, and involves a change in molecular conformation.

2.4. Conclusions

The crystal structure of L-threonine has been determined up to 22.3 GPa, one of the highest pressures ever achieved for a complex molecular material, providing amongst the most detailed information beyond 10 GPa ever published for this type of system.

The structure undergoes two isosymmetric phase transitions on compression between 0.0 and 17.1 GPa. The ambient pressure phase I transforms to phase I' between 2.1 and 3.0 GPa, the result of a subtle reorientation of the carboxylate group. The transformation of phase I' to phase II between 8.5 and 9.8 GPa follows a gradual transformation of a long-range Coulombic interaction into one mediated by a bifurcated hydrogen bond. The transition therefore reflects a change in the way the structure absorbs pressure rather than a distinct structural change, and in this regard, it is somewhat akin to a second order thermal event such as a glass transition.

Further compression results in the transformation to phase III between 17.1 and 18.2 GPa. The II to III transition is driven by a discontinuous reduction in volume and is characterised by the rotation and bifurcation of the hydroxyl groups in half of the molecules in the unit cell.

The crystallographic results are consistent to those seen in the earlier Raman studies. Indeed, the interpretation of the crystallographic data has been substantially guided by the Raman results of Holanda *et al.*[31] While the phase II to III transition involves a discontinuous change in volume and symmetry, phases I, I' and II are all very similar, and the designation of these forms as separate phases is based on discontinuities of the trends seen in Holanda *et al.*'s Raman spectra with increasing pressure. In particular, the I and I' transition is not at all obvious from examination of the crystallographic data alone, and it would probably have been missed without the Raman data. This said, while

Raman spectra have proved to be an extremely sensitive tool for detecting the phase transitions, they are a less definitive guide to the magnitude of the structural changes.

Above 17.1 GPa the crystal structure of L-threonine destabilises rapidly. Holanda's Raman spectra suggest that the material remains crystalline to at least 27 GPa, but the ultimate response of a relatively complex crystal structure such as threonine to very rapid onset of destabilisation is largely unexplored territory. One possibility is amorphisation, as seen for L-alanine at 15 GPa.[16] Cleavage of primary covalent bonds forms another potential route, exemplified by proton transfer in oxalic acid at 5.3 GPa,[80] or even wholescale decomposition into amorphous networks such as is seen for benzene[81-82] and pyridine.[83-84]

Although the hydrogen bonds in L-threonine are substantially compressed up to 22.3 GPa, it is remarkable that their distances all find precedents at ambient pressure, and none of them can be described as 'abnormally short' (**Figure 2.10**). In the 5064 structures of amino acids, peptides and complexes in the CSD (v5.40 November 2018) there are 2105 individual hydrogen bond lengths (ca. 5 %) which are equal to or shorter than the shortest hydrogen bond length in L-threonine at 22.3 GPa. This is in spite of a reduction in unit cell volume by over one-third. Hydrogen bonds are the strongest and most consistently formed intermolecular interactions in organic crystal structures, and this study reveals that their robustness persists well above 10 GPa, even in relatively complex molecular crystals.

It has been shown that the strongest intermolecular interactions generally persist across phase transitions.[85-86] However, the drive to reduce volume becomes ever more pressing as pressure is increased, leading to a perturbation in the hierarchy of intermolecular interactions. It will be fascinating to discover the point at which this effect finally wins out and the fundamental nature of the hydrogen bond is altered beyond our current understanding.

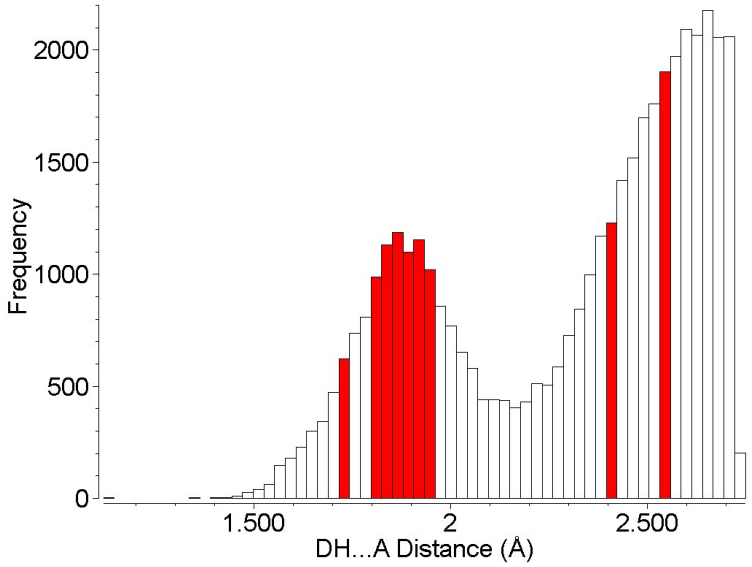

Figure 2.10. Hydrogen bond distances formed in the crystal structures of amino acids. Red bars show H-bond distances observed in L-threonine at 22.3 GPa.

2.5. References

1. Görbitz, C.-H., Crystal structures of amino acids: from bond lengths in glycine to metal complexes and high-pressure polymorphs. *Crystallography Reviews* **2015,** *21* (3), 160-212.

2. Moggach, S. A.; Parsons, S.; Wood, P. A., High-pressure polymorphism in amino acids. *Crystallography Reviews* **2008,** *14* (2), 143-184.

3. Murli, C.; Sharma, S. M.; Karmakar, S.; Sikka, S. K., α-Glycine under high pressures: a Raman scattering study. *Physica B: Condensed Matter* **2003,** *339* (1), 23-30.

4. Dawson, A.; Allan, D. R.; Belmonte, S. A.; Clark, S. J.; David, W. I. F.; McGregor, P. A.; Parsons, S.; Pulham, C. R.; Sawyer, L., Effect of High Pressure on the Crystal Structures of Polymorphs of Glycine. *Crystal Growth & Design* **2005,** *5* (4), 1415-1427.

5. Moggach, S. A.; Marshall, W. G.; Rogers, D. M.; Parsons, S., How focussing on hydrogen bonding interactions in amino acids can miss the bigger picture: a high-pressure neutron powder diffraction study of ε-glycine. *CrystEngComm* **2015,** *17* (28), 5315-5328.

6. Bull, C. L.; Flowitt-Hill, G.; de Gironcoli, S.; Kucukbenli, E.; Parsons, S.; Pham, C. H.; Playford, H. Y.; Tucker, M. G., [zeta]-Glycine: insight into the mechanism of a polymorphic phase transition. *IUCrJ* **2017,** *4* (5), 569-574.

7. Moggach, S. A.; Allan, D. R.; Morrison, C. A.; Parsons, S.; Sawyer, L., Effect of pressure on the crystal structure of l-serine-I and the crystal structure of l-serine-II at 5.4 GPa. *Acta Crystallographica Section B* **2005,** *61* (1), 58-68.

8. Wood, P. A.; Francis, D.; Marshall, W. G.; Moggach, S. A.; Parsons, S.; Pidcock, E.; Rohl, A. L., A study of the high-pressure polymorphs of L-serine using ab initio structures and PIXEL calculations. *CrystEngComm* **2008,** *10* (9), 1154-1166.

9. Boldyreva, E., V.; Kolesnik, E., N.; Drebushchak, T., N.; Sowa, H.; Ahsbahs, H.; Seryotkin Yuri, V., A comparative study of the anisotropy of lattice strain induced in the crystals of DL-serine by cooling down to 100 K, or by increasing pressure up to 8.6 GPa. A comparison with L-serine. *Zeitschrift für Kristallographie - Crystalline Materials* **2006,** *221* (2), 150.

10. Drebushchak, T. N.; Sowa, H.; Seryotkin, Y. V.; Boldyreva, E. V.; Ahsbahs, H., l-Serine III at 8.0 GPa. *Acta Crystallographica Section E* **2006,** *62* (9), o4052-o4054.

11. Moggach, S. A.; Marshall, W. G.; Parsons, S., High-pressure neutron diffraction study of l-serine-I and l-serine-II, and the structure of l-serine-III at 8.1 GPa. *Acta Crystallographica Section B* **2006,** *62* (5), 815-825.

12. Boldyreva, E. V.; Sowa, H.; Seryotkin, Y. V.; Drebushchak, T. N.; Ahsbahs, H.; Chernyshev, V.; Dmitriev, V., Pressure-induced phase transitions in crystalline l-serine studied by single-crystal and high-resolution powder X-ray diffraction. *Chemical Physics Letters* **2006,** *429* (4), 474-478.

13. Fisch, M.; Lanza, A.; Boldyreva, E.; Macchi, P.; Casati, N., Kinetic Control of High-Pressure Solid-State Phase Transitions: A Case Study on l-Serine. *The Journal of Physical Chemistry C* **2015,** *119* (32), 18611-18617.

14. Moggach, S. A.; Allan, D. R.; Clark, S. J.; Gutmann, M. J.; Parsons, S.; Pulham, C. R.; Sawyer, L., High-pressure polymorphism in l-cysteine: the crystal structures of l-cysteine-III and l-cysteine-IV. *Acta Crystallographica Section B* **2006,** *62* (2), 296-309.

15. Lozano-Casal, P.; Allan, D. R.; Parsons, S., High-pressure structural study of l-[alpha]-glutamine and the use of Hirshfeld surfaces and graph-set notation to investigate the hydrogen bonding present in the structure up to 4.9 GPa. *Acta Crystallographica Section B* **2008,** *64* (4), 466-475.

16. Funnell, N. P.; Marshall, W. G.; Parsons, S., Alanine at 13.6 GPa and its pressure-induced amorphisation at 15 GPa. *CrystEngComm* **2011,** *13* (19), 5841-5848.

17. Tumanov, N. A.; Boldyreva, E. V.; Kolesov, B. A.; Kurnosov, A. V.; Quesada Cabrera, R., Pressure-induced phase transitions in l-alanine, revisited. *Acta Crystallographica Section B* **2010,** *66* (4), 458-471.

18. Johnstone, R. D. L.; Francis, D.; Lennie, A. R.; Marshall, W. G.; Moggach, S. A.; Parsons, S.; Pidcock, E.; Warren, J. E., High-pressure polymorphism in L-serine monohydrate: identification of driving forces in high pressure phase transitions and possible implications for pressure-induced protein denaturation. *CrystEngComm* **2008,** *10* (12), 1758-1769.

19. Yoo, C. S.; Kohlmann, H.; Cynn, H.; Nicol, M. F.; Iota, V.; LeBihan, T., Crystal structure of pseudo-six-fold carbon dioxide phase II at high pressures and temperatures. *Physical Review B* **2002,** *65* (10), 104103.

20. Thiéry, M. M.; Léger, J. M., High pressure solid phases of benzene. I. Raman and x-ray studies of C6H6 at 294 K up to 25 GPa. *The Journal of Chemical Physics* **1988,** *89* (7), 4255-4271.

21. Tidey, J. P.; Wong, H. L. S.; McMaster, J.; Schroder, M.; Blake, A. J., High-pressure studies of three polymorphs of a palladium(II) oxathioether macrocyclic complex. *Acta Crystallographica Section B* **2016,** *72* (3), 357-371.

22. Datchi Dr, F.; Weck Dr, G., X-ray crystallography of simple molecular solids up to megabar pressures: application to solid oxygen and carbon dioxide. *Zeitschrift für Kristallographie – Crystalline Materials* **2014,** *229* (2), 135.

23. Turnbull, R.; Hanfland, M.; Binns, J.; Martinez-Canales, M.; Frost, M.; Marqués, M.; Howie, R. T.; Gregoryanz, E., Unusually complex phase of dense nitrogen at extreme conditions. *Nature communications* **2018,** *9* (1), 4717-4717.

24. Akahama, Y.; Nishimura, M.; Kawamura, H.; Hirao, N.; Ohishi, Y.; Takemura, K., Evidence from x-ray diffraction of orientational ordering in phase III of solid hydrogen at pressures up to 183 GPa. *Physical Review B* **2010,** *82* (6), 060101.

25. Weck, G.; Desgreniers, S.; Loubeyre, P.; Mezouar, M., Single-Crystal Structural Characterization of the Metallic Phase of Oxygen. *Physical Review Letters* **2009,** *102* (25), 255503.

26. Eremets, M. I.; Gavriliuk, A. G.; Trojan, I. A.; Dzivenko, D. A.; Boehler, R., Single-bonded cubic form of nitrogen. *Nature Materials* **2004,** *3*, 558.

27. Guńka, P. A.; Dziubek, K. F.; Gładysiak, A.; Dranka, M.; Piechota, J.; Hanfland, M.; Katrusiak, A.; Zachara, J., Compressed Arsenolite As4O6 and Its Helium Clathrate As4O6·2He. *Crystal Growth & Design* **2015,** *15* (8), 3740-3745.

28. Kleppe, A. K.; Amboage, M.; Jephcoat, A. P., New high-pressure van der Waals compound Kr(H2)4 discovered in the krypton-hydrogen binary system. *Scientific Reports* **2014,** *4*, 4989.

29. Wu, G.; Huang, X.; Huang, Y.; Pan, L.; Li, F.; Li, X.; Liu, M.; Liu, B.; Cui, T., Confirmation of the Structural Phase Transitions in XeF2 under High Pressure. *The Journal of Physical Chemistry C* **2017,** *121* (11), 6264-6271.

30. Freire, P. T. C.; Barboza, F. M.; Lima, J. A.; Melo, F. E. A.; Filho, J. M., Raman Spectroscopy of Amino Acid Crystals. In *Raman Spectroscopy and Applications*, Khan Maaz, IntechOpen: 2017; pp 201-223.

31. Holanda, R. O.; Lima, J. A.; Freire, P. T. C.; Melo, F. E. A.; Mendes Filho, J.; Polian, A., New pressure-induced phase transitions of l-threonine crystal: A Raman spectroscopic study. *Journal of Molecular Structure* **2015,** *1092*, 160-165.

32. Merrill, L.; Bassett, W. A., Miniature diamond anvil pressure cell for single crystal x-ray diffraction studies. *Review of Scientific Instruments* **1974,** *45* (2), 290-294.

33. Moggach, S. A.; Allan, D. R.; Parsons, S.; Warren, J. E., Incorporation of a new design of backing seat and anvil in a Merrill–Bassett diamond anvil cell. *Journal of Applied Crystallography* **2008,** *41*, 249-251

34. Dawson, A.; Allan, D. R.; Parsons, S.; Ruf, M., Use of a CCD diffractometer in crystal structure determinations at high pressure. *Journal of Applied Crystallography* **2004,** *37* (3), 410-416.

35. McCormick, L. J.; Giordano, N.; Teat, S. J.; Beavers, C. M., Chemical Crystallography at the Advanced Light Source. *Crystals* **2017,** *7* (12), 382.

36. Stan, C. V.; Beavers, C. M.; Kunz, M.; Tamura, N., X-Ray Diffraction under Extreme Conditions at the Advanced Light Source. *Quantum Beam Science* **2018,** *2* (1), 4.

37. Kantor, I.; Prakapenka, V.; Kantor, A.; Dera, P.; Kurnosov, A.; Sinogeikin, S.; Dubrovinskaia, N.; Dubrovinsky, L., BX90: A new diamond anvil cell design for X-ray diffraction and optical measurements. *Review of Scientific Instruments* **2012,** *83* (12), 125102.

38. Boehler, R.; De Hantsetters, K., New anvil designs in diamond-cells. *High Pressure Research* **2004,** *24* (3), 391-396.

39. Rivers, M.; Prakapenka, V. B.; Kubo, A.; Pullins, C.; Holl, C. M.; Jacobsen, S. D., The COMPRES/GSECARS gas-loading system for diamond anvil cells at the Advanced Photon Source. *High Pressure Research.* **2008,** *28* (3), 273-292.

40. Mao, H. K.; Bell, P. M.; Shaner, J. W.; Steinberg, D. J., Specific volume measurements of Cu, Mo, Pd, and Ag and calibration of the ruby R1 fluorescence pressure gauge from 0.06 to 1 Mbar. *Journal of Applied Physics* **1978,** *49* (6), 3276-3283.

41. *Bruker AXS Inc., APEX 3, Madison, Wisconsin, USA* **2017**.

42. *Bruker AXS Inc., SAINT, Madison, Wisconsin, USA* **2014/15**.

43. Parsons, S., *ECLIPSE- Program for masking high-pressure diffraction images and conversion between CCD image formats. The University of Edinburgh* **2014**.

44. Sheldrick, G. M. *XPREP*, 2008/2; Bruker, Bruker AXS Inc.: Madison, Wisconsin, USA, 2008.

45. Sheldrick, G., SHELXT - Integrated space-group and crystal-structure determination. *Acta Crystallographica Section A* **2015,** *71* (1), 3-8.

46. Sheldrick, G., Crystal structure refinement with SHELXL. *Acta Crystallographica Section C* **2015,** *71* (1), 3-8.

47. Hubschle, C. B.; Sheldrick, G. M.; Dittrich, B., ShelXle: a Qt graphical user interface for SHELXL. *Journal of Applied Crystallography* **2011,** *44* (6), 1281-1284.

48. Kuznetsov, A.; Dmitriev, V.; Dubrovinsky, L.; Prakapenka, V.; Weber, H. P., FCC–HCP phase boundary in lead. *Solid State Communications* **2002,** *122* (3), 125-127.

49. Coelho, A., TOPAS and TOPAS-Academic: an optimization program integrating computer algebra and crystallographic objects written in C++. *Journal of Applied Crystallography* **2018,** *51* (1), 210-218.

50. Gavezzotti, A., Calculation of lattice energies of organic crystals: the PIXEL integration method in comparison with more traditional methods. *Zeitschrift für Kristallographie-Crystalline Materials* **2005,** *220* (5/6), 499-510.

51. Gavezzotti, A., *Molecular Aggregation: Structure Analysis and Molecular Simulation of Crystals and Liquids*. Oxford University Press: Oxford, UK, 2007.

52. Gavezzotti, A., Efficient computer modeling of organic materials. The atom–atom, Coulomb–London–Pauli (AA-CLP) model for intermolecular electrostatic-polarization, dispersion and repulsion energies. *New Journal of Chemistry* **2011,** *35* (7), 1360-1368.

53. Maschio, L.; Civalleri, B.; Ugliengo, P.; Gavezzotti, A., Intermolecular Interaction Energies in Molecular Crystals: Comparison and Agreement of Localized Møller–Plesset 2, Dispersion-Corrected Density Functional, and Classical Empirical Two-Body Calculations. *The Journal of Physical Chemistry A* **2011,** *115* (41), 11179-11186.

54. Wood, P. A.; Forgan, R. S.; Henderson, D.; Parsons, S.; Pidcock, E.; Tasker, P. A.; Warren, J. E., Effect of pressure on the crystal structure of salicylaldoxime-I, and the structure of salicylaldoxime-II at 5.93 GPa. *Acta Crystallographica Section B* **2006,** *62* (6), 1099-1111.

55. Frisch, M. J.; Trucks, G. W.; Schlegel, H. B.; G. E. Scuseria; M. A. Robb; J. R. Cheeseman; G. Scalmani; V. Barone; B. Mennucci; G. A. Petersson; H. Nakatsuji; M. Caricato; X. Li; H. P. Hratchian; A. F. Izmaylov; J. Bloino; G. Zheng; J. L. Sonnenberg; M. Hada; M. Ehara; K. Toyota; R. Fukuda; J. Hasegawa; M. Ishida; T. Nakajima; Y. Honda; O. Kitao; H. Nakai; T. Vreven; J. A. Montgomery, J.; J. E. Peralta; F. Ogliaro; M. Bearpark; J. J. Heyd; E. Brothers; K. N. Kudin; V. N. Staroverov; R. Kobayashi; J. Normand; K. Raghavachari; A. Rendell; J. C. Burant; S. S. Iyengar; J. Tomasi; M. Cossi; N. Rega; J. M. Millam; M. Klene; J. E. Knox; J. B. Cross; V. Bakken; C. Adamo; J. Jaramillo; R. Gomperts; R. E. Stratmann; O. Yazyev; A. J. Austin; R. Cammi; C. Pomelli; J. W. Ochterski; R. L. Martin; K. Morokuma; V. G. Zakrzewski; G. A. Voth; P. Salvador; J. J. Dannenberg; S. Dapprich; A. D. Daniels; Ö. Farkas; J. B. Foresman; J. V. Ortiz; Cioslowski, J.; Fox, D. J. *Gaussian 09*, Gaussian Inc.: Wallingford, USA, 2009.

56. Clark, S., J.; Segall, M., D.; Pickard, C., J.; Hasnip, P., J.; Probert, M., I. J.; Refson, K.; Payne, M., C., First principles methods using CASTEP. *Zeitschrift für Kristallographie - Crystalline Materials* **2005,** *220* (5/6), 567.

57. Dassault Systèmes BIOVIA, Materials Studio 2017. *Dassault Systèmes BIOVIA, Materials Studio, San Diego* **2017**.

58. Tkatchenko, A.; Scheffler, M., Accurate Molecular Van Der Waals Interactions from Ground-State Electron Density and Free-Atom Reference Data. *Physical Review Letters* **2009,** *102* (7), 073005-07300 .

59. Monkhorst, H. J.; Pack, J. D., Special points for Brillouin-zone integrations. *Phys. Rev. B* **1976,** *13* (12), 5188-5192.

60. Hohenstein, E. G.; Sherrill, C. D., Efficient evaluation of triple excitations in symmetry-adapted perturbation theory via second-order Møller–Plesset perturbation theory natural orbitals. *The Journal of Chemical Physics* **2010,** *133* (10), 104107.

61. Parrish, R. M.; Burns, L. A.; Smith, D. G. A.; Simmonett, A. C.; DePrince, A. E.; Hohenstein, E. G.; Bozkaya, U.; Sokolov, A. Y.; Di Remigio, R.; Richard, R. M.; Gonthier, J. F.; James, A. M.; McAlexander, H. R.; Kumar, A.; Saitow, M.; Wang, X.; Pritchard, B. P.; Verma, P.; Schaefer, H. F.; Patkowski, K.; King, R. A.; Valeev, E. F.; Evangelista, F. A.; Turney, J. M.; Crawford, T. D.; Sherrill, C. D., Psi4 1.1: An Open-Source Electronic

Structure Program Emphasizing Automation, Advanced Libraries, and Interoperability. *Journal of Chemical Theory and Computation* **2017,** *13* (7), 3185-3197.

62. Spek, A., Structure validation in chemical crystallography. *Acta Crystallographica Section D* **2009,** *65* (2), 148-155.

63. Angel Ross, J.; Alvaro, M.; Gonzalez-Platas, J., EosFit7c and a Fortran module (library) for equation of state calculations. *Zeitschrift für Kristallographie - Crystalline Materials* **2014,** *229* (5), 405.

64. Dolomanov, O. V.; Bourhis, L. J.; Gildea, R. J.; Howard, J. A. K.; Puschmann, H., OLEX2: a complete structure solution, refinement and analysis program. *Journal of Applied Crystallography* **2009,** *42* (2), 339-341.

65. Bradenburg, K., *DIAMOND*. Crystal Impact GbR, Bonn, Germany: 1999.

66. Macrae, C. F.; Bruno, I. J.; Chisholm, J. A.; Edgington, P. R.; McCabe, P.; Pidcock, E.; Rodriguez-Monge, L.; Taylor, R.; van de Streek, J.; Wood, P. A., Mercury CSD 2.0 - new features for the visualization and investigation of crystal structures. *Journal of Applied Crystallography* **2008,** *41* (2), 466-470.

67. Bruno, I. J.; Cole, J. C.; Edgington, P. R.; Kessler, M.; Macrae, C. F.; McCabe, P.; Pearson, J.; Taylor, R., New software for searching the Cambridge Structural Database and visualizing crystal structures. *Acta Crystallographica Section B* **2002,** *58* (3 Part 1), 389-397.

68. Reeves, M.; Parsons, S.; Wood, P. A., *MR_PIXEL, **2019**, The University of Edinburgh, UK*.

69. Blatov, V. A.; Shevchenko, A. P.; Proserpio, D. M., Applied Topological Analysis of Crystal Structures with the Program Package ToposPro. *Crystal Growth & Design* **2014,** *14* (7), 3576-3586.

70. Tyunina, V. V.; Krasnov, A. V.; Badelin, V. G.; Girichev, G. V., Enthalpy of sublimation of hydroxyl-containing amino acids: Knudsen's effusion mass spectrometric study. *The Journal of Chemical Thermodynamics* **2016,** *98*, 62-70.

71. No, K. T.; Cho, K. H.; Kwon, O. Y.; Jhon, M. S.; Scheraga, H. A., Determination of Proton Transfer Energies and Lattice Energies of Several Amino Acid Zwitterions. *The Journal of Physical Chemistry* **1994,** *98* (42), 10742-10749.

72. Shoemaker, D. P.; Donohue, J.; Schomaker, V.; Corey, R. B., The Crystal Structure of Ls-Threoninel. *Journal of the American Chemical Society* **1950,** *72* (6), 2328-2349.

73. Holanda, R. O.; Freire, P. T. C.; Silva, J. A. F.; Melo, F. E. A.; Filho, J. M.; Lima, J. A., High pressure Raman spectra of d-threonine crystal. *Vibrational Spectroscopy* **2013,** *67*, 1-5.

74. Silva, B. L.; Freire, P. T. C.; Melo, F. E. A.; Filho, J. M.; Pimenta, M. A.; Dantas, M. S. S., High-pressure Raman spectra of L-threonine crystal. *Journal of Raman Spectroscopy* **2000,** *31* (6), 519-522.

75. Prescimone, A.; Morien, C.; Allan, D.; Schlueter, J. A.; Tozer, S. W.; Manson, J. L.; Parsons, S.; Brechin, E. K.; Hill, S., Pressure-Driven Orbital Reorientations and

Coordination-Sphere Reconstructions in [CuF2(H2O)2(pyz)]. *Angewandte Chemie International Edition* **2012,** *51* (30), 7490-7494.

76. Vinet, P.; Ferrante, J.; Rose, J. H.; Smith, J. R., Compressibility of solids. *Journal of Geophysical Research: Solid Earth* **1987,** *92* (B9), 9319-9325.

77. Rychkov, D. A.; Stare, J.; Boldyreva, E. V., Pressure-driven phase transition mechanisms revealed by quantum chemistry: l-serine polymorphs. *Physical Chemistry Chemical Physics* **2017,** *19* (9), 6671-6676.

78. Wood, P. A.; Allen, F. H.; Pidcock, E., Hydrogen-bond directionality at the donor H atom—analysis of interaction energies and database statistics. *CrystEngComm* **2009,** *11* (8), 1563-1571.

79. Dove, M. T., *Structure and dynamics : an atomic view of materials*. Oxford; New York, N.Y. : Oxford University Press: Oxford; New York, N.Y., 2003.

80. Casati, N.; Macchi, P.; Sironi, A., Hydrogen migration in oxalic acid di-hydrate at high pressure? *Chemical Communications* **2009,** (19), 2679-2681.

81. Block, S.; Weir, C. E.; Piermarini, G. J., Polymorphism in Benzene, Naphthalene, and Anthracene at High Pressure. *Science* **1970,** *169* (3945), 586-587.

82. Jackson, B. R.; Trout, C. C.; Badding, J. V., UV Raman Analysis of the C:H Network Formed by Compression of Benzene. *Chemistry of Materials* **2003,** *15* (9), 1820-1824.

83. Zhuravlev, K. K.; Traikov, K.; Dong, Z.; Xie, S.; Song, Y.; Liu, Z., Raman and infrared spectroscopy of pyridine under high pressure. *Physical Review B* **2010,** *82* (6), 064116.

84. Fanetti, S.; Citroni, M.; Bini, R., Structure and reactivity of pyridine crystal under pressure. *The Journal of Chemical Physics* **2011,** *134* (20), 204504.

85. Kazmierczak, M.; Katrusiak, A., Bimodal Distribution of the Shortest Intermolecular Contacts in Crystals of Organic Compounds. *Crystal Growth & Design* **2014,** *14* (5), 2223-2229.

86. Kazmierczak, M.; Katrusiak, A., Quantitative estimate of cohesion forces. *CrystEngComm* **2015,** *17* (48), 9423-9430.

Chapter 3

The Effect of Pressure on Halogen Bonding in 4-Iodobenzonitrile

3.1. Introduction

Hydrogen bonded solids were amongst the first organic systems of any complexity to be studied at high pressure. One of the first studies concerned hydrogen-bonding in oxalic acid,[1] and a substantial body of work now exists which demonstrates that hydrogen-bonded systems are highly sensitive to pressure, exhibiting extensive phase diversity on compression, the amino acids having been studied particularly thoroughly.[2-4] A notable example of the effect of pressure is in migration of the proton positions between the hydrogen-bond donor-acceptor sites in the oxalic acid dihydrate and in cyclohexan-1,3-dione.[5-7] These early works and those that followed, show that hydrogen-bonds are extremely responsive to modification by high pressure.[8]

Other similar classes of interaction, such as the analogous halogen bond, R-X···D (where R = organic group, X = halogen, D = nucleophilic site),[9] which have the potential to be highly sensitive to pressure, have been more lightly investigated. Of the 2,715 high pressure structures deposited in the Cambridge Structural Database (CSD) (v5.40, November 2018), only 41 exhibit halogen bonding. Interest in the area mainly concerns the role of halogen bonding in polymorphism[10-11] and in charge transfer properties of materials.[12-13] In crystal engineering the halogen bond has a propensity to be highly directional, and it has been used to direct chain formation in polymerisation reactions at high pressure.[14] The σ-hole (a region of positive electrostatic potential on the halogen atom)[15] forms along the axis of the covalent bond and directs intermolecular interactions with the nucleophile to be linear (R-X···D = 180°). The degree of atomic separation and interaction energies are affected by the electrostatic potential of the σ hole, which can be tuned by changing the electron withdrawing affinity of the R-group, or by substituting the halogen atom for another which leads to a plethora of compounds with halogen bonding.[16-18]

Halogen bond interactions between N and I have been identified as a potential candidates for high-pressure studies as they have already been shown to be sensitive to variations in temperature.[19] The high polarizability of iodine makes its bonding highly flexible. For example, elemental iodine, which at ambient pressure contains semi-conducting planes of donor-acceptor interactions (I···I = 3.50 and 3.97 Å, where 2x the van der Waals radius of I is 4.08 Å),[20] transforms to a metal at 16 GPa.[21] In the context of other metallisation transitions in the main-group elements, this is quite a modest pressure. Very recently compression beyond 10 GPa of the organic polyiodide salt, tetraethylammonium diiodine triiodide has been shown to lead to an insulating-to-semiconducting transformation driven by donor-acceptor bond formation between iodine molecules and tri-iodide anions.[22]

The I···N intermolecular distance in 4-iodobenzonitrile (**Scheme 3.1**) is 3.168(4) Å which is substantially shorter than the sum of the van der Waals radii (3.58 Å).[20] In this chapter we describe the effects of pressure on this interaction up to 8.1 GPa with the aim of characterising its sensitivity to compression.

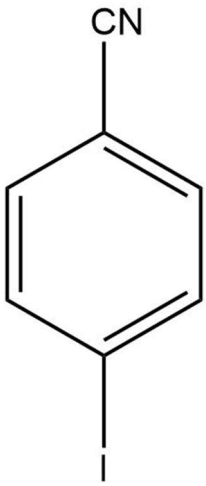

Scheme 3.1 Chemical structure diagram of 4-iodobenzonitrile

3.2. Experimental

3.2.1. High-Pressure Experiments

Single crystal X-ray diffraction, Raman and UV-Vis absorption spectroscopy at high pressure were performed in Merrill-Bassett or Boehler-Almax type diamond anvil cells (DACs) equipped with 0.6 mm culet type Ia Boehler-Almax cut diamonds. Tungsten gaskets with holes of diameter 0.25–0.35 mm and thickness 0.1–0.12 mm formed the sample chambers and the hydrostatic pressure transmitting media, were either 1:1 *n*-pentane:iso-pentane, 4:1 methanol-ethanol or spectroscopic paraffin oil. Pressures were determined by the ruby fluorescence method.[23]

3.2.2. Recrystallisations and Compression Conditions

Over the course of this work the response of 4-iodobenzonitrile to high pressure was studied under four different sets of conditions.

(i) Ex situ crystal growth followed by compression in pentane-isopentane: 4-Iodobenzonitrile (97%, Sigma-Aldrich) was first recrystallised by solvent diffusion of *n*-pentane in dichloromethane solution to give colourless, rectangular-prismatic crystals. Initial ambient and high-pressure X-ray diffraction data were collected on a crystal of dimensions 0.1 x 0.2 x 0.2 mm^3 in *n*-pentane:iso-pentane to 5.0 GPa using a lab source diffractometer (see below). Beyond 5.0 GPa the sample darkened in colour and diffraction quality decreased dramatically (**Figure 3.1(a)**) but there was nevertheless some evidence of crystallinity in the form of weak diffraction at low angle. A second series of measurements was therefore carried out using methanol-ethanol as a hydrostatic medium with the aim of obtaining better quality data above 5 GPa.[24]

(ii) Ex situ crystal growth and compression in methanol-ethanol: 4-Iodobenzonitrile was recrystallised by slow evaporation of a 4:1 methanol-ethanol solution to give colourless, rectangular prism shaped crystals. Ambient and high-pressure X-ray diffraction data were collected using

a crystal (0.1 x 0.1 x 0.1 mm³) and the mother liquor from the crystal growth as the pressure transmitting medium. Data were collected to 5.5 GPa using synchrotron radiation (see below). A new phase formed at 5.5 GPa but the sample contained numerous quite weakly-scattering domains. We therefore turned to *in situ* crystal growth with the aim of obtaining an improved data set.

(iii) In situ crystal growth and slow compression in methanol-ethanol: A 4-iodobenzonitrile in 4:1 methanol-ethanol solution was loaded in a DAC to give a polycrystalline mass on compression at 0.5 GPa. A colourless crystal measuring 0.12 x 0.18 x 0.22 mm³ was obtained by repeatedly heating the DAC to 420 K and cooling to room temperature (**Figure 3.1(b)**). High-pressure X-ray diffraction data were collected to 4.9 GPa in *ca.* 0.9 GPa steps using synchrotron radiation. The crystal broke apart above 5 GPa and no discernible diffraction data could be obtained.

(iv) In situ crystal growth followed by rapid compression in methanol-ethanol: A small single crystal (~0.05 mm³) was regrown *in situ* but rapidly compressed to 8.1 GPa from ambient pressure in one step. High-pressure diffraction measurements were performed immediately on a lab source diffractometer to give sufficiently good data for structure solution and refinement.

3.2.3. Single Crystal X-ray Diffraction

Single crystal diffraction data were collected using both sealed-tube and synchrotron X-radiation. The synchrotron data were collected on Beamline 11.3.1 at the Advanced Light Source on a Bruker D8 diffractometer with silicon (111) monochromated synchrotron radiation, wavelength 0.7749 Å (E = 16.5 keV) and PHOTON-II detector. Shutterless ω-scans with different 2θ and ϕ-offsets were performed at step widths of 0.3° with exposure times of 1 s. The sealed-tube data sets were collected using a Bruker APEX-II diffractometer with graphite monochromated Mo-Kα radiation (λ=0.7107 Å) and exposure times of 30 s.

Diffraction images were integrated using SAINT with dynamic masks generated by ECLIPSE to mask shaded detector areas.[25,26] The multi-scan procedure SADABS[27] was used to treat cell and sample absorption errors. The structure of phase I was solved using direct methods (SHELXT) [28] and that of phase II at 8.1 GPa by simulated annealing (DASH).[29] Structures were refined by full-matrix least-squares on $|F|^2$ (SHELXL)[30] using the ShelXLe graphical user interface.[31]

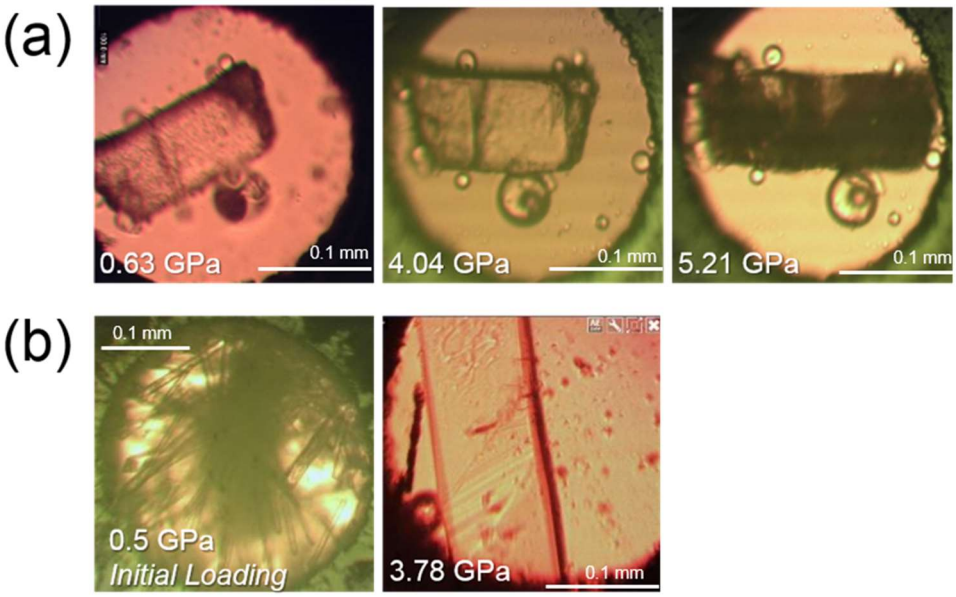

Figure 3.1 Crystals used in this study: (a) *Ex situ* crystal loaded in methanol-ethanol (Section 3.2i), the crystal transparency reduction is apparent at 5.21 GPa. (b) *In situ* crystal growth from melting the initial polycrystalline mass to 420 K and allowing to cool to room temperature repeatedly (Section 3.2iii).

Non-hydrogen intramolecular bond distances in each high-pressure model were restrained to those of the ambient temperature-pressure structure. In phase I the molecule has .2. site symmetry; in phase II it occupies a general position but was restrained to have C_{2v} symmetry during refinement. Only the iodine atom was refined with anisotropic displacement parameters, with the light-atoms restrained to have similar isotropic displacement parameters in the high-pressure structure refinements; the ambient temperature-pressure

structure was refined with anisotropic displacement parameters for non-hydrogen atoms. All H-atoms were placed in calculated positions and allowed to ride on their parent atoms. The phase I to II transition is reconstructive and there is no rational geometric relationship between the lattices; it was found unnecessary to model twinning in phase II.

Crystal and refinement data immediately below and above the phase transition are collected in **Table 3.1**, a full set of parameters for the 18 data collected over the course this study is available in the electronic supplementary information (ESI). CCDC 1911442-1911459 also contains the supplementary crystallographic data for this chapter.

3.2.4. Raman and UV-Vis Spectroscopy

High-pressure Raman spectra were collected in parallel to the single-crystal diffraction experiments during the study using the crystal grown *ex situ* in methanol-ethanol as a pressure transmitting medium [method (ii) above]. The instrument used was a Horiba LabRAM HR Evolution Raman spectrometer using an 1880 lines mm^{-1} grating and 633 nm excitation. The range was 50 to 3400 cm^{-1}. An Olympus BXFM-ILHS microscope with a 50x long working distance objective was used for laser focusing to a spot size of *ca.*2 μm on to the sample. Spectra were collected on compression up to 9.7 GPa and on decompression to ambient pressure at 298 K.

Room temperature UV-Vis absorption spectra at high pressure were performed in a custom-made setup. The modulated light from deuterium and tungsten lamps was dispersed with a monochromator and focused on the sample with a reflective objective. The transmitted light was collected with another reflective objective and the signal detected with a photomultiplier was synchronously detected with a lock-in amplifier. The experiments were carried out using paraffin oil (Merck) as transmitting medium. The pressure and

hydrostatic conditions were checked through the shift and bandwidth of ruby R-lines luminescence, respectively.

3.2.5. High-Pressure Conductivity Measurements

Electrical resistance was measured on a compressed powder sample using a four-probe method in a Merrill-Bassett DAC with 800 μm culet anvils (**Figure 3.2**). Gold contacts were made on one of the anvils through a custom-made mask using a sputter coater. Daphne 7373 oil was used as a pressure medium. A ruby chip was loaded into the sample space and pressure was measured using ruby fluorescence. The metallic parts of the cell and gasket were electrically insulated to avoid short circuits. The electrical resistance of the sample was measured using Keithley 6517A electrometer using the constant voltage method. The electrical resistance was measured with increasing pressure. At just above 5 GPa we observed a sudden drop in resistance which is also accompanied by the darkening of the sample.

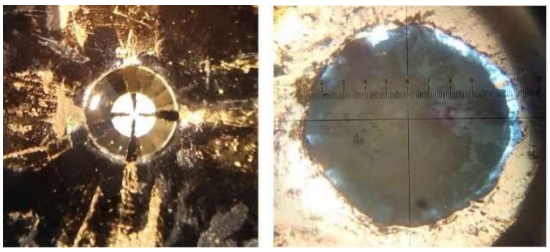

Figure 3.2 On the left: Diamond with gold sputtered contacts (no sample). On the right: IBN sample within a gasket hole under 5 GPa. The transparent light blue areas between inner gasket hole and sample represent PVC layer.

3.2.6. PIXEL Energy Calculations

Molecular electron densities were calculated by quantum chemical methods at each pressure point by GAUSSIAN09[32] with the MP2/DGDZVP level of theory and basis set. CH distances were reset to 1.083 Å for structures determined experimentally with X-ray diffraction, but left unchanged for structures which had been optimised by periodic DFT. The electron density grid obtained from Gaussian was in steps of 0.06 Å and condensation level of 4 was used for the PIXEL calculations (CLP-PIXEL).[16,33] The cluster radius was 15 Å. A breakdown of the interaction energies within the first coordination spheres of phase I at ambient pressure and 5.0 GPa and phase II at 5.5 GPa are given in **Tables 5.2–5.4.**

PIXEL has been used previously to study interactions involving iodine,[16, 34] and the ability of the method to reproduce experimental sublimation energies of iodine compounds is assessed in the ESI. For 4-iodobenzonitrile itself the lattice energy calculated by PIXEL is –62.5 kJ mol^{-1}, which is smaller in magnitude than the experimental enthalpy of sublimation, 88.0(3) kJ mol^{-1}, determined using Knudsen effusion methods by Rocha *et. al.*[35] However, the difference is consistent with the performance of PIXEL for other iodine containing compounds. Rounding errors in the PIXEL energy calculations also occur in the presence of iodine because of its large size and high polarizability and results in small differences in the calculated energies of symmetry equivalent molecules, for example, symmetry related contacts E and F at 0.0 GPa (**Table 3.2**) have Coulombic energy terms of –7.7 and –7.5 kJ mol^{-1}. In these cases, the calculated PIXEL energies are averaged to give –7.6 kJ mol^{-1}.

Table 3.1 Experimental details for the ambient pressure structure, and structures immediately below and above the phase transition. For all structures: C_7H_4IN, M_r = 229.01. Experiments were carried out at 298 K. H-atom parameters were constrained. CCDC deposition numbers are 1911442, 1911457, and 1911458.

Pressure (GPa)	0.00	5.00	5.49
Phase	I	I	II
Crystal data			
Crystal system, space group	Monoclinic, *I*2/*a*	Monoclinic, *I*2/*a*	Triclinic, *P*–1
a, *b*, *c* (Å)	7.788 (2), 10.592 (3), 9.086 (3)	6.8316 (3), 10.2395 (6), 8.0931 (18)	5.692 (5), 6.9674 (11), 7.7283 (12)
α, β, γ (°)	90, 104.934 (9), 90	90, 100.696 (7), 90	65.412 (13), 80.98 (4), 87.77 (3)
V (Å^3)	724.2 (4)	556.29 (13)	275.1 (3)
Z	4	4	2
Radiation type	Synchrotron, λ = 0.7749 Å	Mo *Kα*	Synchrotron, λ = 0.7749 Å
μ (mm^{-1})	5.39	5.63	7.09
Crystal size (mm)	0.20 × 0.02 × 0.02	0.20 × 0.10 × 0.10	0.1 × 0.1 × 0.1
Diffractometer	Bruker D8 with Photon II detector	Bruker *APEX* 2	Bruker D8 with Photon II detector
T_{min}, T_{max}	0.533, 0.746	0.601, 0.745	0.390, 0.745
No. of measured, independent and observed [$I > 2\sigma(I)$] reflections	3052, 741, 703	1028, 192, 189	549, 236, 197
R_{int}	0.027	0.039	0.041
$(\sin\theta/\lambda)_{max}$ (Å^{-1})	0.626	0.622	0.575
$R[F^2 > 2\sigma(F^2)]$, $wR(F^2)$, S	0.016, 0.038, 1.13	0.043, 0.114, 1.19	0.111, 0.293, 1.34
No. of parameters	44	22	30
No. of restraints	0	13	34
$\Delta\rho_{max}$, $\Delta\rho_{min}$ (e Å^{-3})	0.22, –0.53	1.19, –0.56	1.87, –1.16

3.2.7. Periodic Density Functional Theory (DFT) Calculations

Geometry optimisations, vibrational frequency and Raman intensity calculations were carried-out using the plane-wave pseudopotential method in the CASTEP code[36] as incorporated in Materials Studio version 2017. [37] The PBE exchange-correlation functional was used with norm-conserving pseudopotentials and a basis set cut-off energy of 1020 eV.[38] Brillouin zone integrations were performed with a Monkhorst-Pack **k**-point grid spacing of 0.07 $Å^{-1}$. [39] The starting coordinates were taken from the single-crystal diffraction structures at 0.0 and 5.5 GPa and optimised using the Tkatchenko-Scheffler correction for dispersion (DFT-D).[40] The cell dimensions were fixed to the experimental values, and the space group symmetry was retained. For geometry optimisations the convergence criteria were $5x10^{-6}$ eV/atom in energy, 0.01 eV $Å^{-1}$ for force, 5 $x10^{-4}$ Å for displacement and $5x10^{-7}$ eV/atom for self-consistent field convergence. Prior to calculation of the Raman spectra, these were tightened to $1x10^{-8}$ eV/atom, 0.003 eV $Å^{-1}$ and $1x10^{-10}$ eV/atom, respectively.[41] Frequencies were calculated at the Γ-point only for comparison with the experimental Raman spectra.

3.2.8. Band Structure Calculations

Band structure and projected density of state (pdos) calculations were performed using CASTEP (version 16.11), with the PBE exchange-correlation functional. Norm-conserving potentials built into CASTEP and a plane wave basis set energy cut-off of 1300 eV were used. For the band structures, **k**-points were sampled along high symmetry paths (U-R-X-Γ-Y-Z) and (Γ-Y-T-Z-Γ) for the phases I and II, respectively. Projected densities of states were generated from a subsequent band-structure calculation using OptaDOS. [42-43]

3.2.9. Other Programs Used

OLEX2[44] and MERCURY[45] were used for data visualisation, and sample geometries analysed using PLATON.[46] Equation-of-state calculations were performed by EOSFIT.[47] MOGUL,[48] and CONQUEST [49] were used to survey the Cambridge Structural Database (CSD).[50]

3.3. Results & Discussion

3.3.1. Ambient Pressure Structure and the First Coordination Sphere

4-iodobenzonitrile crystallises in phase I at ambient conditions from dichloromethane or a mixture of methanol and ethanol and at high pressure (0.6 GPa) from methanol-ethanol. The crystal structure of 4-iodobenzonitrile was determined by Schlemper and Britton in 1965, [51] and subsequently by Desiraju and Harlow in 1989. [52] The structure has also been compared with those of other iodobenzene derivatives by Merz. [53] The space group is *I*2/*a*, with the four molecules in the unit cell residing on crystallographic two-fold axes. The intermolecular contacts are listed in **Table 3.2**, where contacts are labelled A-L in order of energy as calculated by PIXEL.

Molecules related by unit cell translations along **b** (molecules G and H in **Table 3.2**) are linked by I···N halogen bonding interactions into an exactly linear chain, with a contact distance of 3.168(4) Å and a total intermolecular energy of –10.8 kJ mol^{-1} (**Figure 3.3(a)**). Note that this is not the strongest interaction in the structure. For comparison, Carlucci and Gavezzotti reported a dimer energy of –14.3 kJ mol^{-1} for the interaction involving the I···N contact (at 3.1 Å) in the pyrazine-iodobenzene cocrystal.[16]

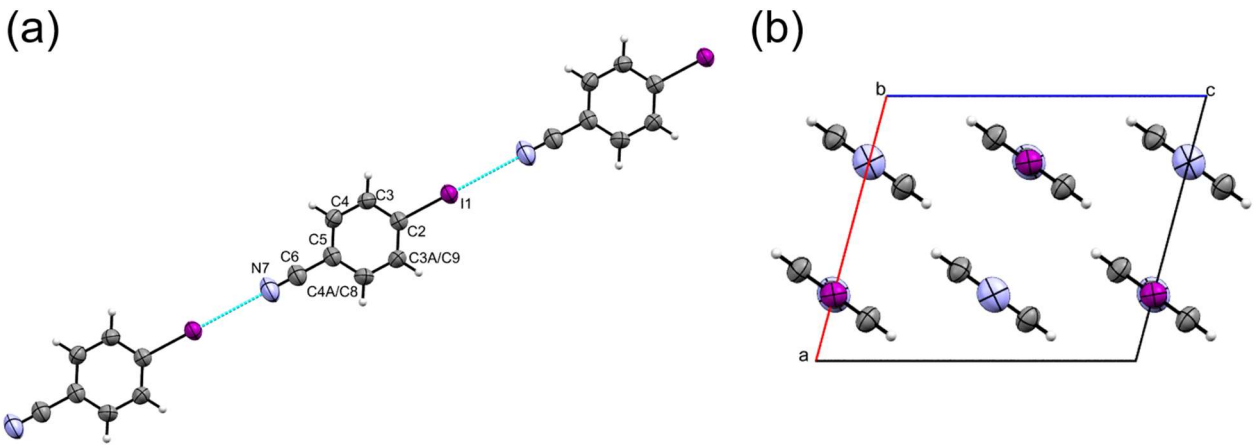

Figure 3.3 (a) ORTEP style plot of 4-iodobenzonitrile and the numbering scheme used in this study. The atom numbering scheme in phase II is the same as that of phase I but the symmetry generated C3 and C4 become C9 and C8, respectively. Ellipsoids are drawn at the 50 % probability level. **(b)** Molecular chains formed along **b** surrounded by six neighbouring chains.

The Raman spectra of 4-iodobenzonitrile are shown as a function of pressure in **Figure 3.4** with an expansion of the lattice mode region at ambient pressure in **Figure 3.5 (a)**, where the experimentally measured spectra are in black with the positions and intensities of the modes calculated by periodic DFT in red. The DFT frequencies, which are unscaled, reproduce the experimental values within 20 cm^{-1}, while the intensities are less reliably reproduced, as is usual. The DFT results indicate that the strong bands at 100 cm^{-1} and below are whole-molecule rocking motions. The calculations also indicate that there are three Raman active modes at 229 (intensity 8 $Å^4$ amu^{-1}), 233 (186) and 241 (16) cm^{-1}, which agrees with the three observed modes at 230, 237 and 243 cm^{-1}). Of these, the central band is the symmetric I···N stretching mode, which has A_g symmetry in the C_{2h} point group of the crystal lattice; the other two modes have B_g symmetry. In the primitive setting of the unit cell there are two unique I···N bonds and the corresponding anti-symmetric mode is only infra-red active (calc. 235 cm^{-1}, A_u symmetry).

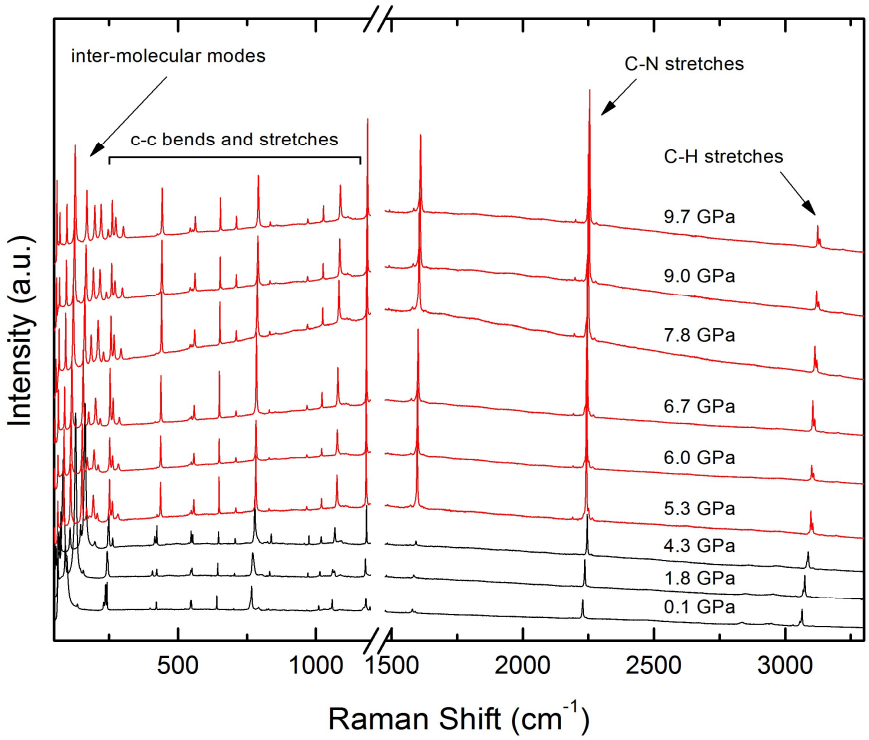

Figure 3.4 Raman spectra collected on compression of 4-iodobenzonitrile over the entire spectral range studied. Phase I spectra are shown in black, and phase II spectra in red.

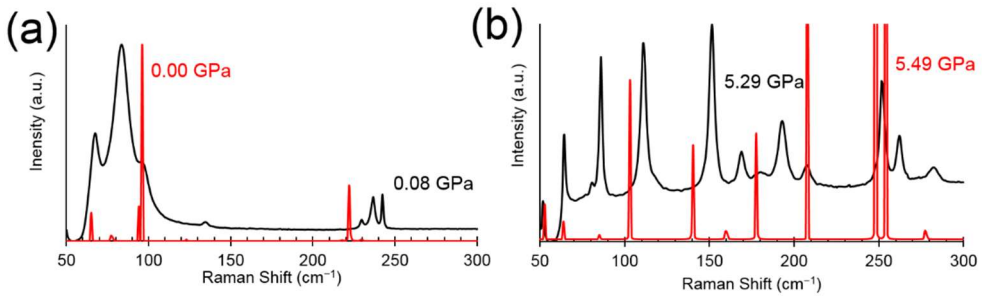

Figure 3.5 Comparison of the lattice phonon regions in the Raman spectrum of 4-iodobenzobitrile. **(a)** Phase I at *ca*. ambient pressure. Black: measured at 0.08 GPa in a diamond anvil cell, red: calculated form the ambient-pressure crystal structure by periodic DFT. **(b)** Phase II at *ca* 5.5 GPa. Black: measured at 5.29 GPa, red: calculated from the crystal structure at 5.49 GPa.

Each halogen-bonded chain in the crystal structure is surrounded by six others, with offset π···π stacking and other dispersion-based interactions between them which range in energy from –6.8 to –12.6 kJ mol^{-1}, **Figure 3.3 (b)**. The shortest contacts between the chains are between C4H4···I1 and C4H4···N7

at *ca.* 3.3 Å in molecules A to F which have total molecule-molecule energies of –12.6 and –11.7 kJ mol^{-1}. Contacts to molecules I and J involve longer C4H4···I interactions at 3.59 Å and have energies of –7.6 kJ mol^{-1}. The longest contacts are formed in offset π···π stacking interactions, at 4.040(2) Å in molecules K and L, with total molecular interaction energies of –6.8 kJ mol^{-1}.

Overall the first coordination sphere contains 12 molecules which can be grouped into four pairs and one quartet of symmetry related interactions, to give rise to five unique dimer pairs. The arrangement of the molecules in the first coordination sphere is referred to as its underlying topology and in phase I can be approximated to be like cubic close packing *i.e.* a molecular coordination number of 12 with ABC layers. The central reference molecule is surrounded by six others forming a layer with three molecules above and three below (**Figure 3.6(a)**).

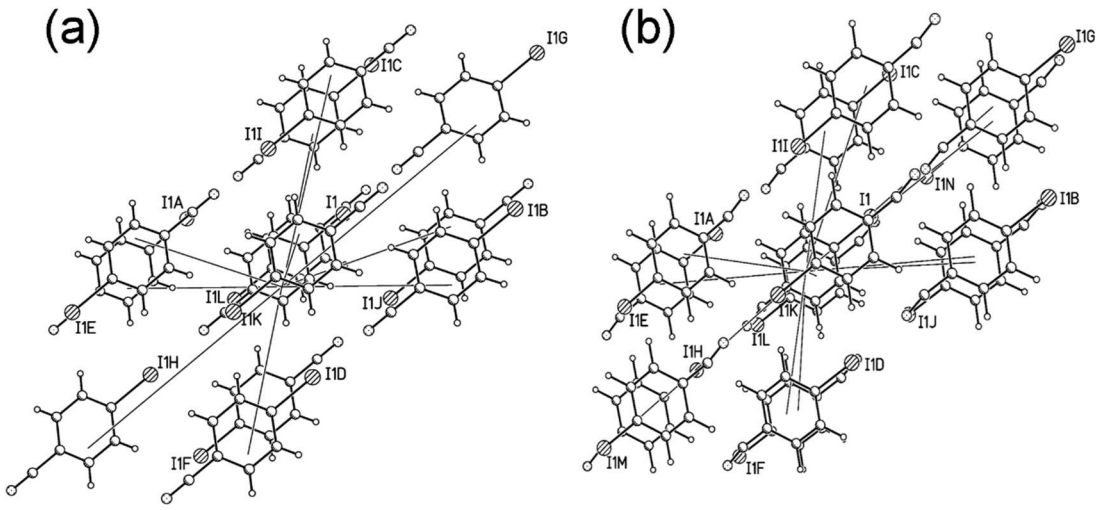

Figure 3.6 First coordination spheres of **(a)** Phase I at 5.0 GPa, which has a molecular coordination number (MCN) = 12 and approximately CCP topology. **(b)** Phase II at 5.5 GPa, which has MCN=14, consistent with a body centred cubic topology. Both phases feature an ABC layering sequence in the vertical direction.

3.3.2. Response of Phase I to Pressure

The energies of the five unique dimers observed between ambient pressure and 5.0 GPa are plotted as a function of centroid separation in **Figure 3.7**, which also shows the structure of each dimer. Dimer energies are listed in **Table 3.2** and **Table 3.3**. There is a pronounced response to pressure in terms of total interaction energies in pairs E and F (ΔE= +10.2 kJ mol^{-1}); G and H (ΔE= +7.5 kJ mol^{-1}); and, K and L (ΔE= +34.9 kJ mol^{-1}).

The least sensitive of these involve the I···N interactions to molecules G and H. The I···N contact shortens from 3.168(4) to 2.840(1) Å between ambient pressure and 5 GPa (**Figure 3.8 (a)**). The Coulombic energy is the largest term in these contacts and the overall molecular interaction remains slightly stabilising at 5.0 GPa with a total energy of –3.3 kJ mol^{-1}. The frequency of the symmetric C-I/I···N stretch increases with pressure, a reflection of the stiffening of intermolecular potentials as the molecules are pushed into closer proximity, reaching a value of 249.3 cm^{-1} at 4.3 GPa (the highest-pressure Raman measurement in phase I).

The contact which is most sensitive to pressure is with molecules K and L which interact via π···π interactions which shorten from 3.6420(8) to 3.139(4) Å (**Figure 3.8(b)**). The overall interaction energy becomes quite destabilising at 5.0 GPa as the molecules are forced into a strongly repulsive regime (total interaction energy = +28.1 kJ mol^{-1}).

Of the remaining interactions, E and F which involve CH···N interactions which shorten from 3.27 to 2.84 Å, are also quite sensitive to pressure. Dispersion is the largest energy term in these contacts, but the Coulombic contribution is also significant. Interaction energies in contacts A to D; and I and J, are characterised by CH···I interactions and hardly change with pressure at all. C4H4···I7 interactions shorten from 3.29 to 2.88 Å and C3H3···I7 interactions shorten from 3.59 to 3.09 Å to 5.0 GPa, and the total energies change by only –2.3 kJ mol^{-1} and +0.2 kJ mol^{-1}, respectively. Molecules A to D,

characterised by C4H4···I7 interactions, are the only contacts seen to strengthen, albeit slightly.

The structural response to pressure thus favours compression of the weaker π···π interactions over the I···N halogen bond. The distinction is reflected in the changes in the unit cell dimensions.

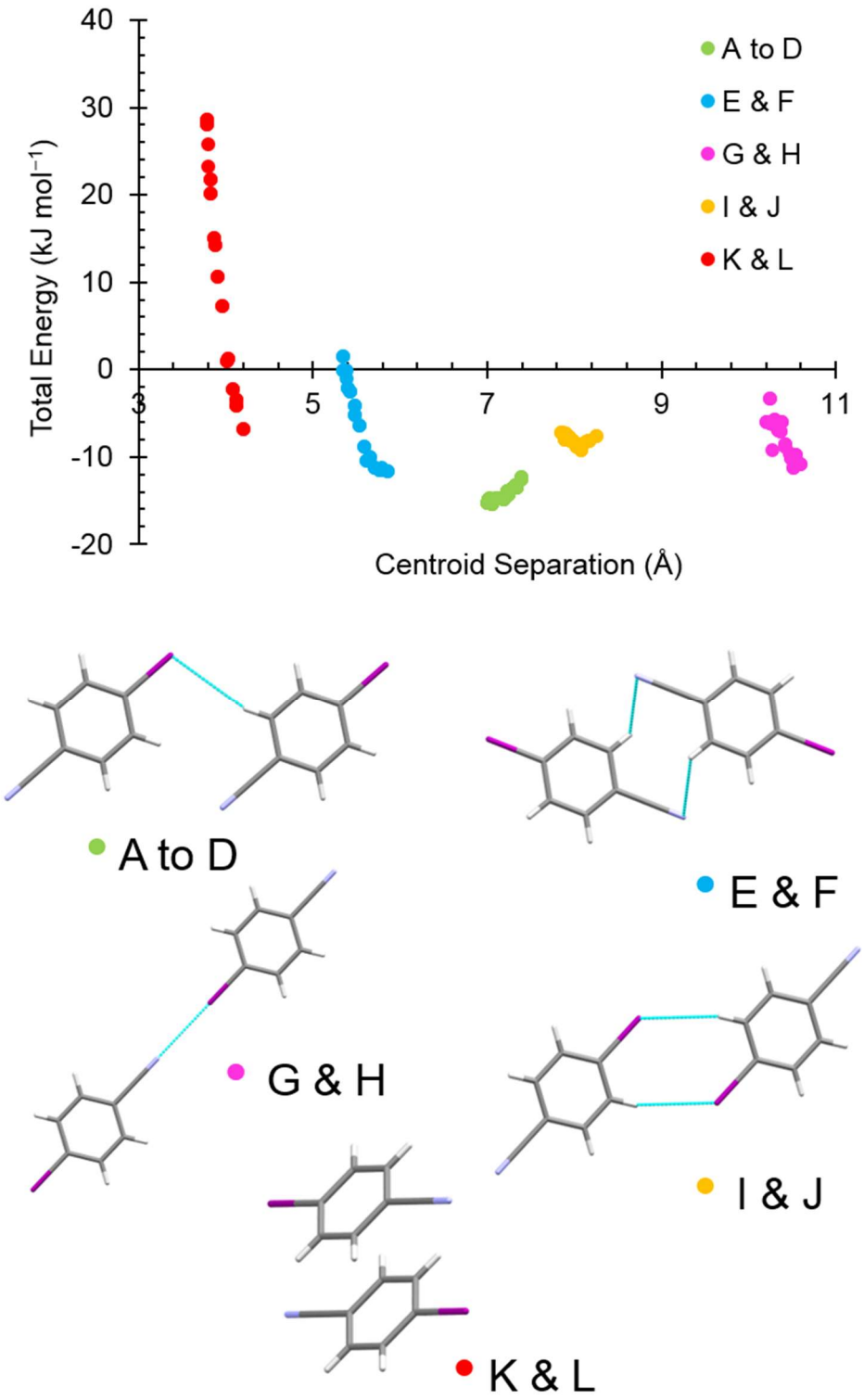

Figure 3.7 Graph of total interaction energy for the five most energetically significant dimers in 4-iodobenzonitrile phase I as a function of molecular centroid separation. The dimers shown are those of the ambient pressure structure. The atom contacts involved in each interaction in phase I are given in **Tables 3.2 and 3.3**.

Table 3.2 PIXEL calculated dimer interaction energies of the phase I polymorph at 0.0 GPa. All energies are in kJ mol^{-1}.

Label	Centroid Distance (Å)	Symmetry	Coulombic	Polarization	Dispersion	Repulsion	Total	Contacts
A	7.398	–1/2+x,1/2+y,–1/2+z	–8.4	–3.2	–10.6	9.6	–12.6	I1···H4C4 = 3.29 Å
B		1/2+x,–1/2+y,1/2+z						
C		–1/2+x,–1/2+y,–1/2+z						
D		1/2+x,1/2+y,1/2+z						
E	5.864	1/2–x,3/2–y,1/2–z	–7.6	–3.1	–12.6	11.6	–11.7	2 x long N7···H4C4 =
F		1/2–x,3/2–y,3/2–z						2 x 3.27 Å
G	10.592	x,–1+y,z	–19.0	–6.6	–8.8	23.6	–10.8	I1···N7 = 3.168(4) Å
H		x,1+y,z						
I	8.248	1/2–x,1/2–y,1/2–z	–5.4	–2.0	–12.5	12.3	–7.6	2 x long I1···H3C3 =
J		1/2–x,1/2–y,3/2–z						2 x 3.59 Å
K	4.205	1–x,1–y,1–z	–15.7	–5.8	–30.9	45.6	–6.8	Cg···Cg = 4.040(2) Å
L		–x,1–y,1–z						

Table 3.3 PIXEL calculated dimer interaction energies of the phase I polymorph at 5.0 GPa, immediately below the phase transition. All energies are in kJ mol^{-1}.

Label	Centroid Distance (Å)	Symmetry	Coulombic	Polarization	Dispersion	Repulsion	Total	Contacts
A	7.009	–1/2+x,1/2+y, –1/2+z	–19.5	–10.7	–20.3	35.6	–14.9	I1···H4 = 2.88 Å &
B		1/2+x, –1/2+y,1/2+z						N7···H3 = 2.83 Å
C		–1/2+x, –1/2+y, –1/2+z						
D		1/2+x,1/2+y,1/2+z						
E	5.349	1/2–x,3/2–y,1/2–z	–28.0	–14.6	–29.6	73.7	1.5	2 x long N7···H3C3 = 2 x 2.90 Å
F		1/2–x,3/2–y,3/2–z						2 x N7···H4C4 = 2 x 2.84 Å
G	10.239	x, –1+y,z	–43.7	–17.5	–15.3	73.2	–3.3	I1···N7 = 2.840(1) Å
H		x,1+y,z						
I	7.862	1/2–x,1/2–y,1/2–z	–24.0	–10.4	–27.4	54.4	–7.4	2 x I1···H3C3 = 2 x 3.09 Å
J		1/2–x, 1/2–y, 3/2–z						
K	3.781	1–x,1–y,1–z	–78.7	–28.4	–65.2	200.4	28.1	Cg···Cg = 3.593(6) Å
L		–x,1–y 1–z						

Table 3.4 PIXEL calculated dimer energies of the phase II polymorph at 5.5 GPa, immediately above the phase transition. All energies are in kJ mol^{-1}.

Label	Centroid Distance (Å)	Symmetry	Coulombic	Polarization	Dispersion	Repulsion	Total	Contacts
A B	7.728	x,y,1+z x,y,–1+z	–17.8	–8.9	–18.3	32.6	–12.5	I1···H4 = 2.94 Å & N7···H9 = 2.77 Å
C D	5.692	–1+x,y,z 1+x,y,z	–37.5	–17.4	–40.7	98.6	3.0	I1···H8C8/H9C9 = 2.98/3.07 Å & H3···H8 = 2.38 Å
E	5.242	2–x, 1–y,1–z	–25.4	–15.1	–31.2	71.6	–0.1	2 x N7···H3 = 2 x 2.88 Å & H4···H8 = 2 x 2.44 Å
F	6.474	3–x,–y,1–z	–24.3	–9.4	–18.5	34.0	–18.2	2 x N7···H8 = 2 x 2.50 Å
G H	10.292	–1+x,y,–1+z 1+x,y,1+z	–33.9	–13.7	–13.2	55.3	–5.6	I1···N7 = 2.928(10) Å

Table 3.4 Continued PIXEL calculated dimer energies of the phase II polymorph at 5.5 GPa, immediately above the phase transition. All energies are in kJ mol^{-1}.

Label	Centroid Distance (Å)	Symmetry	Coulombic	Polarization	Dispersion	Repulsion	Total	Contacts
I	8.287	1–x,1–y,–z	–14.9	–8.6	–23.8	41.1	–6.3	2 x I1···H3 = 2 x 3.09 Å
J	7.240	2–x,–y,–z	–29.8	–17	–31.1	72.6	–5.2	2 x I1···H9 = 2 x2.87 Å
K	4.894	2–x,1–y,–z	–70.5	–23.6	–56.8	172.5	21.6	2 x I1···Cg = 3.38(2) Å
L	3.337	2–x,–y,1–z	–59.6	–24.2	–57.7	188.3	46.7	Cg···Cg = 3.530(8) Å & I1···N7 = 3.33(2) Å
M	7.832	3–x,1–y,1–z	–1.8	–0.7	–2.6	0.6	–4.4	long N7···N7 = 4.10(4) Å
N	10.011	1–x,–y,–z	–4.6	–1.4	–7.3	11.8	–1.5	long I1···I1 = 4.241(7) Å

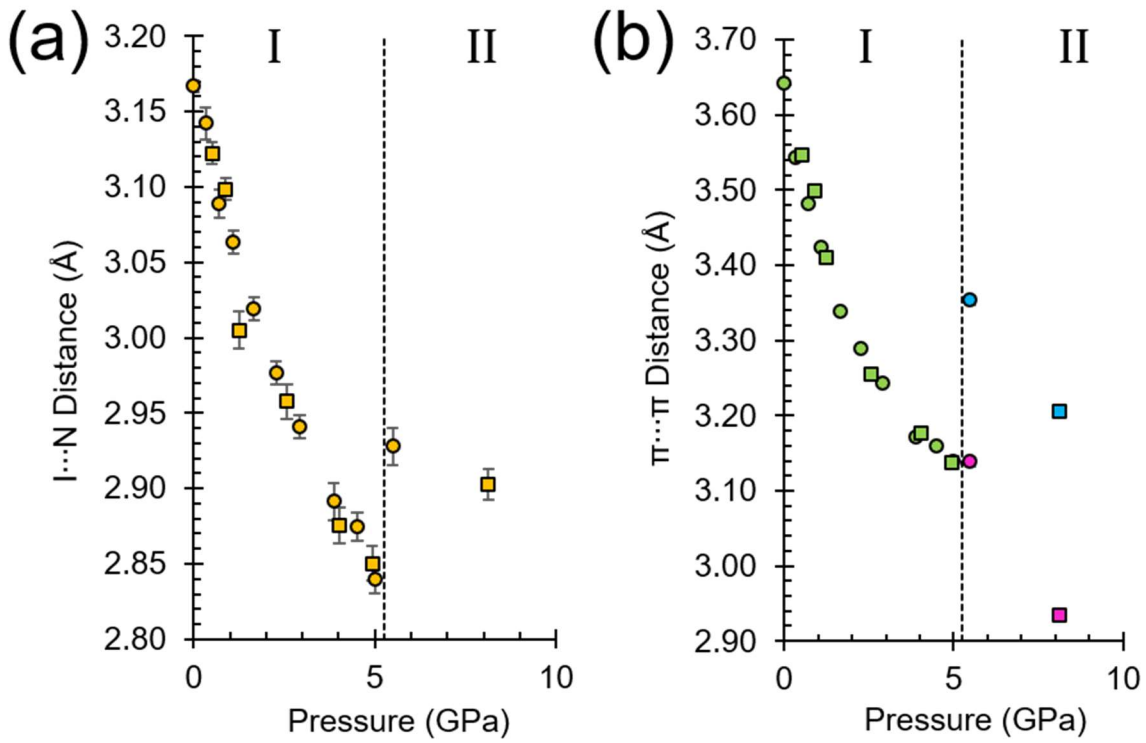

Figure 3.8 (a) Change in the axial I···N distance relating to contacts G and H as a function of pressure. Circles represent *ex-situ* data and squares represent *in-situ* data. The contacts remain related by symmetry in both phases. **(b)** The change in π···π stacking distances between the layers in contacts K and L as a function of pressure. Circles represent *ex-situ* collected data and squares *in-situ* collected data. K (blue) and L (purple) contacts split into two symmetry independent contacts in phase II.

3.3.3. Unit Cell Compression

The π···π offset stacking interactions (molecules K and L), which show the largest decrease in distance with pressure, are expressed along the *a*– and *c*–axes, which compress by 12.3 and 10.9 % up to 5.0 GPa. The least compressible interactions (I···N) are generated by lattice translations along **b**, and this axis compresses by only 3.3 % (**Figure 3.9(a)**). A fit of the variation of unit cell volume of phase I with pressure to a third order Birch-Murnaghan equation of state (EOS) is given in **Figure 3.9(b)** and yields a bulk modulus K_0 = 6.5(6) GPa, with a pressure derivative K' = 8.9(11).

A small bulk modulus (<10 GPa) is typical of soft materials where dispersion forces dominate intermolecular interactions *e.g.* tolazamide I, 6.4(3) GPa,[54] and aniline II, 5.4(2) GPa,[55] but can be higher if additional intermolecular interactions such as strong H–bonding are present, *e.g.* hydroquinone-formic acid clathrate has K_0 = 13.6(4) GPa.[56]

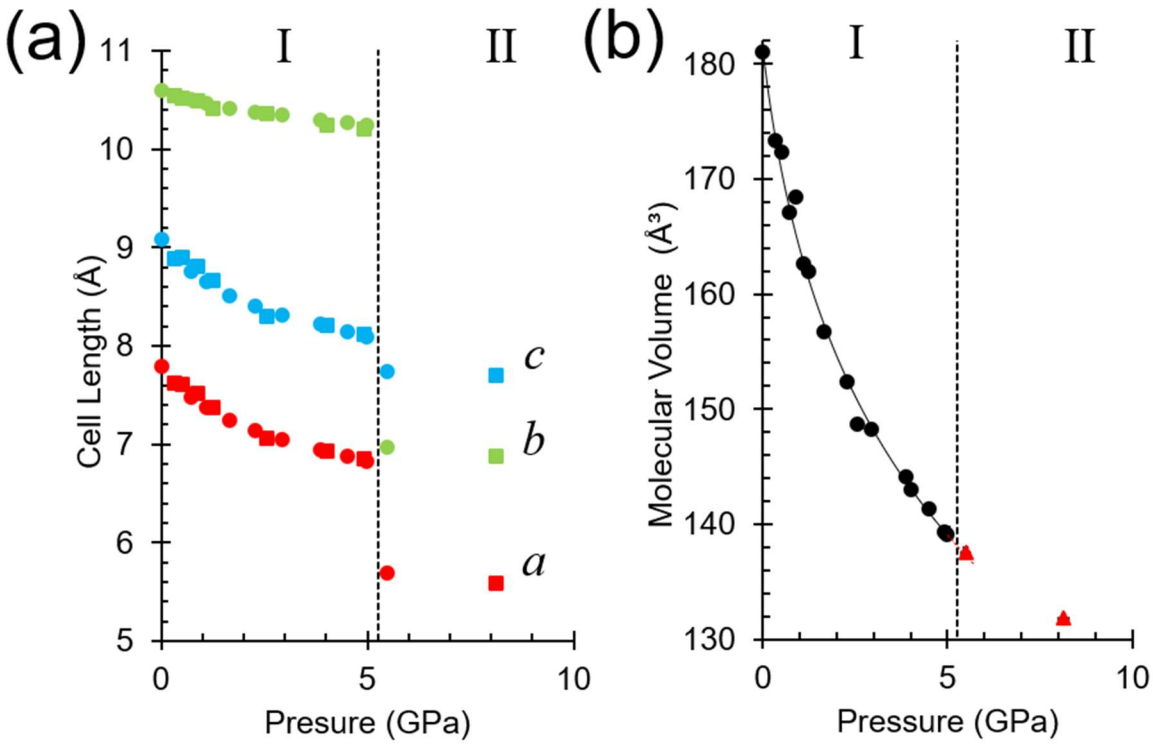

Figure 3.9 (a) Plot of unit cell parameters as a function of pressure. *Ex situ* crystal data are shown as circles and *in situ* crystal data are shown as squares **(b)** Molecular volume of all phase I data, black circles, fitted to a 3rd order Birch-Murnaghan EOS and extrapolated to 5.7 GPa (red-dashed line). Phase II data are shown as red triangles. Error bars are obscured by data markers and the phase boundary is indicated by a dashed line in both figures.

3.3.4. Formation of Phase II

Phase I transforms to a new high-pressure polymorph (phase II) at 5.5 GPa, with sharp discontinuities in the unit cell dimensions (**Figure 3.9**). Phase II is triclinic (*P*–1) with two molecules in the unit cell. The phase transition from phase I to II tended to lead to fragmentation of a single crystal of phase I. After some experimentation (see Section 3.2) a well-diffracting single crystal of phase II was obtained by *in situ* crystal growth in methanol-ethanol, followed by a rapid increase in pressure to 8.1 GPa; the structure of phase II was solved from this data set. This solution was used to model the data obtained from a fragmented crystal at 5.5 GPa.

The phase transition causes the crystal to darken in colour (**Figure 3.1(a)**), accompanied by a marked decrease in resistance (**Figure 3.10**). However, the UV-visible spectra shown in **Figure 3.11** indicate neither a considerable redshift of the absorption edge nor any new absorbance features between 300 and 800 nm up to 8 GPa. The only changes occur in the background, which is related to the presence of light scattering by the sample.

The creation of crystal domains, usual in reconstructive first order phase transitions involving anisotropic structures, gives rise to multiple scattering with the walls of the domains resulting in a clear darkening of the sample. Therefore, the sample darkening is not related to a change in band structure, but rather to formation of very small domains as the crystal passes through the phase transition. The change in microstructure reduces the transmittance of the sample by two orders of magnitude (**Figure 3.11**).

This conclusion is supported by the band structures of 4-iodobenzonitrile at 5, 5.5 and 8.1 GPa, shown in **Figure 3.12**. It is evident that each of the phases is an insulator, with calculated thermal bandgaps of 2.8 eV at 5 GPa, reducing to 2.5 eV at 8.14 GPa. These values will be underestimated compared to the true bandgap owing to the use of the PBE functional. Overall, the band structures show relatively flat bands, demonstrating that there is little

dispersion in the crystal and that the bands can be viewed as molecular orbitals. The projected densities of states illustrate this, showing that each atomic species is responsible for the makeup of the bands. Interestingly, upon increasing pressure, the contribution of iodine to the HOMO band is markedly increased.

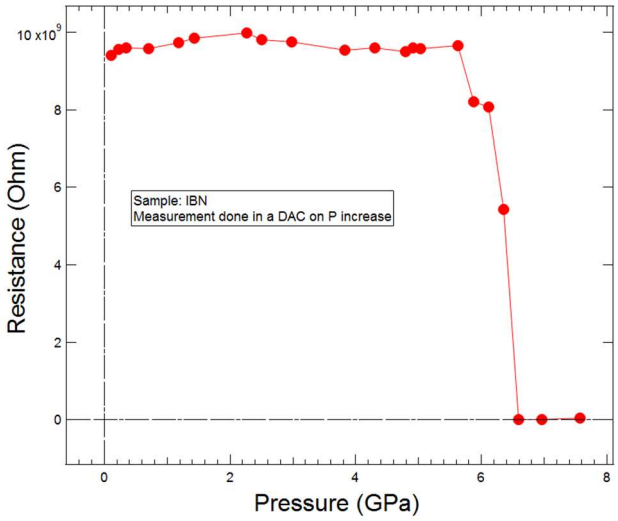

Figure 3.10 Resistance of polycrystalline 4-iodobenzonitrile as a function of pressure. A drop from 10^{10} to $8x10^9$ Ω occurs at the phase transition. The precipitous drop beyond 6 GPa comes from interference from the gasket.

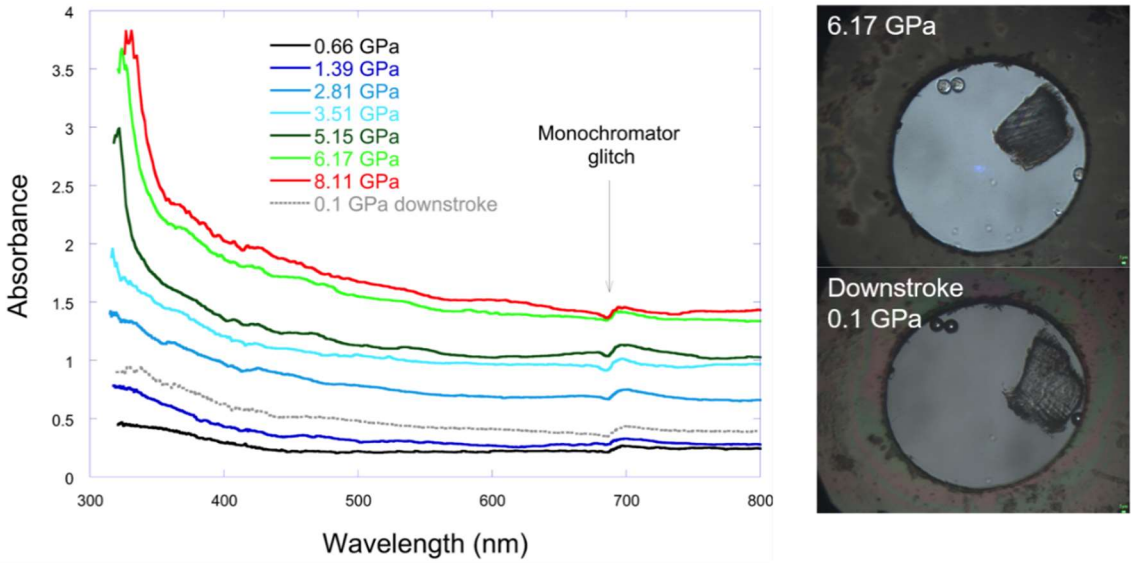

Figure 3.11 On the left: UV-Vis absorption spectra of 4-iodobenzonitrile as a function of pressure. On the right: Images of the hydrostatic chamber with the sample and ruby spheres. The crystal does not fully recover after pressure release.

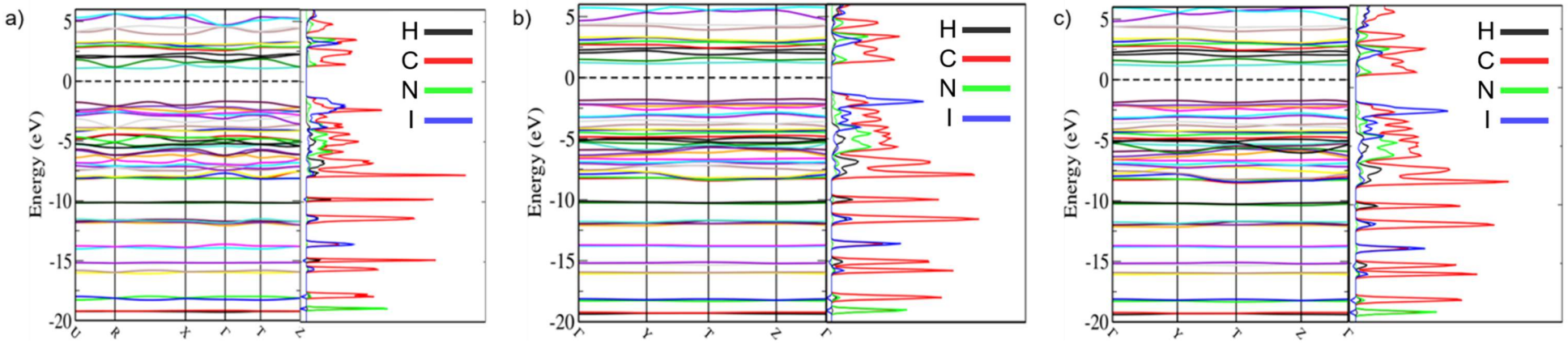

Figure 3.12 Band structure and electronic density of states of 4-iodobenzonitrile at (a) 5 GPa, (b) 5.5 GPa and (c) 8.14 GPa. The density of states are shown projected onto their atomic species where hydrogen – black, carbon – red, nitrogen – green and iodine – blue.

The clearest effect of the phase I → II transition on the Raman spectra (**Figure 3.4**) is an increase in intensity in the bands above 1500 cm^{-1} that correspond to a mixture of CC stretches and CCH bends in the phenyl group. The results of the DFT calculations indicate that a doubling of the intensity in this region would be expected, and the larger enhancement seen in the spectra in **Figure 3.4** may additionally reflect the influence of sample orientation. The changes below 250 cm^{-1} are more dramatic, with the whole-molecule rocking region now extending beyond 200 cm^{-1} (**Figure 3.5**). Three modes persist in the 250 cm^{-1} region, now all of the same symmetry (A_g). The calculated frequency values, 248 cm^{-1} (intensity 131 $Å^4\,amu^{-1}$), 254 (93) and 277 (33) agree within 10 cm^{-1} with the observed positions at 252, 263 and 282 cm^{-1}. Animations of the modes indicate that the C-I/I···N stretch remains localised in the first, and strongest, of these bands. The other two modes are in- and out-of plane oscillations which cause bending at the I···N interaction.

3.3.5. The Crystal Structure of Phase II

Restraints were applied to the intramolecular bond distances and angles, and so it is not possible to determine if there are major changes in these parameters with pressure. This said, the nitrile group appears to be quite non-linear at 5.5 GPa with <C5–C6–N7 = 169(2)°. The non-linearity persisted when the structure of phase II was optimised by periodic DFT, with a magnitude which is smaller (4.4°) and more similar to the value 4(3)° obtained at 8.1 GPa. It is possible that the larger experimental value at 5.5 GPa is a consequence of the relatively low data quality obtained from the fragmented sample (R_1 = 11.1 %).

Phase II exhibits the same four classes of short contact found in phase I (π···π, CH···I, CH···N and I···N) as well as some additional I···π and H···H contacts. The energetically most significant dimer interactions in are shown in **Figure 3.13**, with energies listed in **Table 3.4**. The contacts in **Table 3.4** are labelled so that molecule A in phase II occupies a similar position in the first

coordination sphere as molecule A in phase I *etc.* The contact labels in the two phases can thus be correlated directly (**Figure 3.6**).

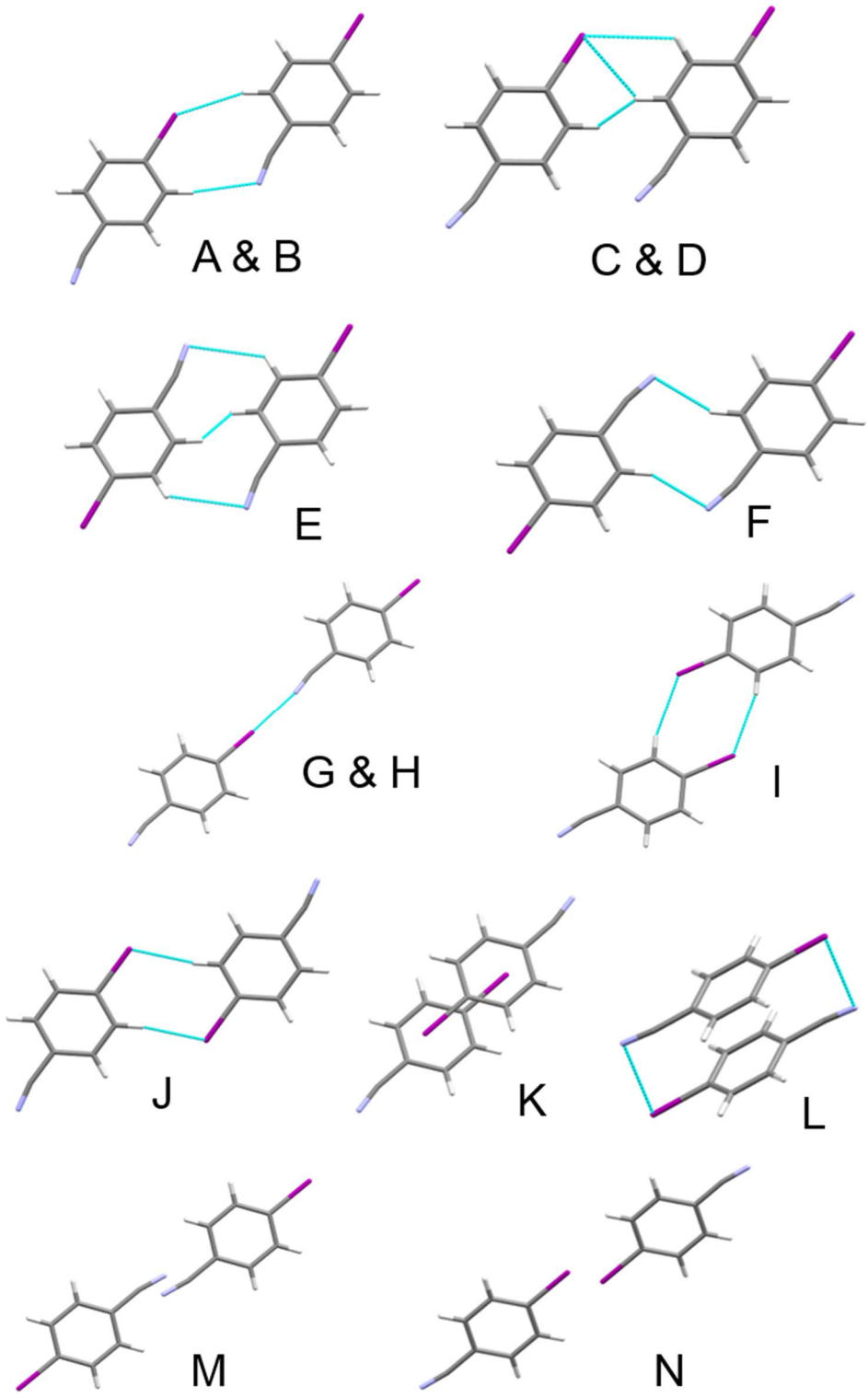

Figure 3.13 The most energetically significant dimers in the phase II structure of 4-iodobenzonitrile at 5.5 GPa.

Like phase I, the structure of phase II consists of chains of molecules which interact via I···N interactions (G and H). The chains are no longer strictly linear [<C2I1···N7 = 166.2(5)°] and the I···N distance increases over the course of the transition from 2.840(1) Å in phase I at 5.0 GPa to 2.928(10) Å in phase II at 5.5 GPa. Even at 8.1 GPa the distance is 2.90(2) Å (**Figure 3.8(a)**). The energy of the interaction does not change by much: –3.3 kJ mol^{-1} in phase I at 5.0 GPa and –5.6 kJ mol^{-1} in phase II at 5.5 GPa, figures which are lower than in a range of ambient-pressure structures with differing σ–hole strengths studied by Gavezzotti and Carlucci in which the I···N distances varied between 2.95 and 3.15 Å and the energies from –30.2 to –15.1 kJ mol^{-1}. [16] Consistent with the modest strengthening, the frequency of the I···N stretching mode is similar but slightly higher than at 4.3 GPa (252 versus 249 cm^{-1}).

Each chain is surrounded by six other chains (like in phase I *cf.* **Figure 3.7**). The four equivalent inter-chain interactions of phase I labelled A-D and mediated by short I···H and N···H contacts split in phase II into two pairs of contacts. The A/B pair is similar to phase I, but C and D become off-set stacking interactions with a shorter centroid-centroid distance and a slightly destabilising energy. The pair of antiparallel off-set stacking interactions E/F in phase I split into two inequivalent contacts in phase II. Contact E is similar to that in phase I, but interaction F becomes longer and more coplanar. The change in contact F is partly responsible for driving the phase transition (see below).

The degenerate pair of contacts I and J in phase I split into symmetry inequivalent interactions in phase II, but their character and energies are largely unaffected. The pair of antiparallel stacking contacts K/L in phase I, which become strongly destabilising in phase I at 5.0 GPa, split into two stacking interactions (**Figure 3.8(b)**). In contact K the C–I bond of one molecule moves above the phenyl ring of the other, with the slippage between the rings changing from 1.747 to 3.056 Å. The stacking distance increases from 3.139(4) to 3.353(6) Å, and the energy becomes less positive. In L the slippage is slightly

smaller (1.614 Å) with an unchanged stacking distance of 3.139(6) Å and the interaction becomes more destabilising.

Two new long contacts where the shortest distances are formed between pairs of iodine and nitrogen atoms also emerge as two additional molecules (M and N) enter the first coordination sphere. The interactions are long [N7···N7 = 4.10(4) Å in M and I1···I1 = 4.241(7) Å in N] and the energies are small but stabilising. The first coordination sphere in phase II thus contains fourteen molecules. It is like that of Phase I, with a central six molecule layer but now with four molecules above and four molecules below the central layer instead of three, resulting in a change of the underlying topology from pseudo cubic close packed in phase I to body centred cubic in phase II (**Figure 3.6(b)**).

3.3.6. The Driving Force of the Phase I-to-II Transition

The orientation matrices for the diffraction patterns obtained before and after the transition yield the following relationship between the basis vectors of phases I and II:

$$\begin{pmatrix} -0.478 & 0.403 & -0.423 \\ 0.470 & 0.421 & 0.917 \\ 0.512 & 0.499 & -0.189 \end{pmatrix}$$

The patterns were measured at different pressures (5.0 and 5.5 GPa), but the elements of this matrix are rather far from rational fractions, meaning that there is not a simple symmetrical relationship between the phases. This is further evidence that the phase transition is first order and reconstructive, supporting the conclusions made in Section 3.3.4.

The extrapolated molecular volume of phase I at 5.5 GPa is 137.3(3) Å^3. The observed value of the molecular volume at 5.5 GPa is the same, within error, at 137.6(3) Å^3. The negligible change in molecular volume at the phase transition is significant because it indicates that, unlike most high-pressure phase transitions, the dominating thermodynamic factor is not volume minimisation.

The volume in phase II at 8.1 GPa appears to lie on the same trendline as those in phase I, but with only two data points available it is not possible to determine an equation of state for phase II.

In order to identify the likely 'driving force' of the phase transition the intermolecular interaction energies in phase I were calculated using a structure in which the unit cell dimensions of phase I were extrapolated to 5.5 GPa using third-order Birch-Murnaghan equations of state (EoSFIT).[47] The estimated cell dimensions were a = 6.7923 Å, b = 10.2202 Å, c = 8.0533 Å and β = 100.7°. The structure was optimised by periodic DFT, and intermolecular energies calculated using PIXEL. Intermolecular energies were likewise calculated following optimisation of the experimentally determined phase II structure at the same pressure. The lattice energy of phase I was +4.1 kJ mol^{-1} and that of phase II –0.9 kJ mol^{-1}, reproducing the expected energetic ordering of phases I and II at the phase transition. The difference in DFT energies was –0.2 kJ mol^{-1}.

A comparison of contact energies within the first coordination sphere (**Table 3.5**; a more detailed listing is available in the ESI, **Table S3.3**) shows that overall the contacts in phase II are more stabilising by 12.9 kJ mol^{-1}. The largest stabilising changes over the course of the I to II transition occur for the contacts F and K. In both cases the stabilising components of the molecule-molecule energies become less negative, but at the same time the repulsion terms also become less positive (a full breakdown given in **Table S3.4** in the ESI). Both effects can be traced to the larger centroid-centroid separations for the contacts in phase II, contact F changing from 5.38 to 6.61 Å and K from 3.73 to 4.81 Å.

Table 3.5 Comparison of energies within the first coordination spheres in phases I and II at 5.5 GPa. Energies are in kJ mol^{-1} and distances are in Å. Both structures were optimised by periodic DFT and the energies calculated using PIXEL.

Phase I at 5.5 GPa			Phase II at 5.5 GPa			Δ(II-I)
Contact	Distance	Total Energy	Contact	Distance	Total Energy	
A	6.984	–13.8	A	7.728	–12.2	1.6
B	6.984	–13.8	B	7.728	–12.2	1.6
C	6.984	–13.5	C	5.692	1.2	14.7
D	6.984	–13.5	D	5.692	1.2	14.7
E	5.381	3.4	E	5.296	–4.9	–8.3
F	5.382	2.5	F	6.606	–18.6	–21.1
G	10.22	–0.1	G	10.292	–6.3	–6.2
H	10.22	–3.7	H	10.292	–6.3	–2.6
I	7.774	–5.3	I	8.145	–6.1	–0.8
J	7.774	–5.3	J	7.158	–4.9	0.4
K	3.729	33.1	K	4.805	16.8	–16.3
L	3.729	35.3	L	3.375	50.4	15.1
			M	7.962	–3.7	–3.7
			N	9.878	–2.0	–2.0
Totals		5.3			–7.6	–12.9

Both contacts F and K are destabilising in phase I at 5.5 GPa. After the transition F becomes stabilising, while K remains destabilising but less so than in phase I. The transition can thus be described as being driven by relief of interactions that had become destabilising on compression of phase I.

3.4. Conclusions

Taylor has compared the frequency of occurrence of intermolecular contacts in crystal structures to the frequency expected if determined solely by the exposed surface areas of atoms.[57] Highly preferred interactions occur much more often than would be expected on the basis of random packing arrangements, an effect which can be quantified with a metric R_F which adopts a value of > 1 if interactions are formed more frequently than would be expected by chance. Hydrogen bonds have the highest values of R_F, occupying 9 out of the top 10 highest-ranked interactions, for example H-bonds to Br^-, oxygen and sulfur are 10.9, 5.8 and 2.9, respectively. The I···N halogen bond, for which $R_F = 5.4$, is the only non-hydrogen bond to occur in Taylor's Top Ten, with a similar frequency to H-bonds involving oxygen and nitrogen.

4-Iodobenzonitrile is ideal for studying the mechanical properties of this, the most consistently-formed, halogen bond because it forms crystals in which I···N bonds are exactly aligned with the *b*-axis of its monoclinic unit cell. Symmetry, in the form of Neumann's Principle, demands that this direction must be one of the principal directions of anisotropic strain, so that comparing compression along **b** with that along **a** and **c** enables the response to pressure of the I···N halogen bond to be compared directly to that of interactions mediated by other common classes of interaction such as π-stacking and CH···N and CH···I contacts. The gradients of the lines in the 'phase I' panel of **Figure 3.9(a)** graphically illustrate the low compressibility of the I···N bonds compared to the other contacts in the crystal structure.

Even though the I···N interaction is the least compressible interaction, that does not mean that it is the strongest. PIXEL calculations show that molecule-molecule energy within the halogen-bonded chains is essentially the same as in the more compressible contacts (**Table 3.2**). The response of different contacts to pressure measures their deformability rather than their

strength (*i.e.* energy), characterising the shape of an intermolecular potential rather than its depth. Deep wells are not necessarily steep wells.

PIXEL calculations show that the Coulombic contribution to the I···N interaction is twice that of the dispersion term, and that this weighting increases with pressure. Dispersion is the largest term in the other contacts, but here too, the contribution of electrostatics increases with pressure. Interactions which are dominated by dispersion are often found to be deformable because dispersion imposes no directional restrictions, whereas there is usually a distinct orientational preference in electrostatic interactions, the linear geometry of the halogen bonding studied here, for example, being dictated by the spatial characteristics of the lone pair on N and σ-hole on I. However, the halogen bond remains linear up to 5 GPa and its incompressibility may simply reflect that at ambient pressure the I···N distance is already 0.36 Å within the sum of the van der Waals radii of I and N, a figure which rises to 0.69 Å at 5 GPa. There is thus less 'room for manoeuvre' than in the other interactions for which the minimum figure is 0.30 Å even at 5 GPa.

The I···N interaction remains stabilising (just) throughout the pressure range of this study. The same is not true of the N···H and π-stacking interactions, which have become destabilising at 5 GPa. On increase of pressure to 5.5 GPa the monoclinic phase 4-iodobenzonitrile undergoes a phase transition to a triclinic phase. The I···N-linked chains become less linear, but the PIXEL calculations show that the transition is driven by relief of the destabilising N···H and π-stacking interactions. The reduction in molecular volume which must occur at the transition is within the precision of our measurements, the apparent small increase is just statistical noise. Unlike most other high-pressure phase transitions the one in 4-iodobenzonitrile thus appears to be driven by the contribution of the intermolecular interactions to the free energy rather than the $P\Delta V$ term.

3.5. References

1. Putkonen, M.-L.; Feld, R.; Vettier, C.; Lehmann, M. S., Powder neutron diffraction analysis of the hydrogen bonding in deutero-oxalic acid dihydrate at high pressures. *Acta Crystallographica Section B* **1985,** *41* (1), 77-79.

2. Görbitz, C. H., Crystal structures of amino acids: from bond lengths in glycine to metal complexes and high-pressure polymorphs. *Crystallography Reviews* **2015,** *21* (3), 160-212.

3. Boldyreva, E., High-pressure diffraction studies of molecular organic solids. A personal view. *Acta Crystallographica Section A* **2008,** *64* (1), 218-231.

4. Moggach, S. A.; Parsons, S.; Wood, P. A., High-pressure polymorphism in amino acids. *Crystallography Reviews* **2008,** *14* (2), 143-184.

5. Katrusiak, A., High-pressure X-ray diffraction study on the structure and phase transition of 1,3-cyclohexanedione crystals. *Acta Crystallographica Section B* **1990,** *46* (2), 246-256.

6. Casati, N.; Macchi, P.; Sironi, A., Hydrogen migration in oxalic acid di-hydrate at high pressure? *Chemical Communications* **2009,** (19), 2679-2681.

7. Macchi, P.; Casati, N.; Marshall, W. G.; Sironi, A., The α and β forms of oxalic acid di-hydrate at high pressure: a theoretical simulation and a neutron diffraction study. *CrystEngComm* **2010,** *12* (9), 2596-2603.

8. Boldyreva, E. V., High-pressure studies of the anisotropy of structural distortion of molecular crystals. *Journal of Molecular Structure* **2003,** *647* (1), 159-179.

9. Politzer, P.; Murray, J. S.; Clark, T., Halogen bonding and other [sigma]-hole interactions: a perspective. *Physical Chemistry Chemical Physics* **2013,** *15* (27), 11178-11189.

10. Olejniczak, A.; Katrusiak, A., Structure–property relations in chloroacetonitriles. *CrystEngComm* **2011,** *13* (16), 5212-5219.

11. Podsiadło, M.; Olejniczak, A.; Katrusiak, A., Halogen···halogen contra C–H···halogen interactions. *CrystEngComm* **2014,** *16* (35), 8279-8285.

12. Wesela-Bauman, G.; Parsons, S.; Serwatowski, J.; Woźniak, K., Effect of high pressure on the crystal structure and charge transport properties of the (2-fluoro-3-pyridyl)(4-iodophenyl)borinic 8-oxyquinolinate complex. *CrystEngComm* **2014,** *16* (47), 10780-10790.

13. Tian, D.; Winter, S. M.; Mailman, A.; Wong, J. W. L.; Yong, W.; Yamaguchi, H.; Jia, Y.; Tse, J. S.; Desgreniers, S.; Secco, R. A.; Julian, S. R.; Jin, C.; Mito, M.; Ohishi, Y.; Oakley, R. T., The Metallic State in Neutral Radical Conductors: Dimensionality, Pressure and Multiple Orbital Effects. *Journal of the American Chemical Society* **2015,** *137* (44), 14136-14148.

14. Wilhelm, C.; Boyd, S. A.; Chawda, S.; Fowler, F. W.; Goroff, N. S.; Halada, G. P.; Grey, C. P.; Lauher, J. W.; Luo, L.; Martin, C. D.; Parise, J. B.; Tarabrella, C.; Webb, J. A.,

Pressure-Induced Polymerization of Diiodobutadiyne in Assembled Cocrystals. *Journal of the American Chemical Society* **2008,** *130* (13), 4415-4420.

15. Brinck, T.; Murray, J. S.; Politzer, P., Molecular surface electrostatic potentials and local ionization energies of Group V–VII hydrides and their anions: Relationships for aqueous and gas-phase acidities. *International Journal of Quantum Chemistry* **1993,** *48* (2), 73-88.

16. Carlucci, L.; Gavezzotti, A., A quantitative measure of halogen bond activation in cocrystallization. *Physical Chemistry Chemical Physics* **2017,** *19* (28), 18383-18388.

17. Politzer, P.; Murray, J. S.; Clark, T.; Resnati, G., The σ-hole revisited. *Physical Chemistry Chemical Physics* **2017,** *19* (48), 32166-32178.

18. Clark, T.; Hennemann, M.; Murray, J. S.; Politzer, P., Halogen bonding: the σ-hole. *Journal of Molecular Modeling* **2007,** *13* (2), 291-296.

19. Forni, A.; Metrangolo, P.; Pilati, T.; Resnati, G., Halogen Bond Distance as a Function of Temperature. *Crystal Growth & Design* **2004,** *4* (2), 291-295.

20. Alvarez, S., A cartography of the van der Waals territories. *Dalton Transactions* **2013,** *42* (24), 8617-8636.

21. Riggleman, B. M.; Drickamer, H. G., Approach to the Metallic State as Obtained from Optical and Electrical Measurements. *The Journal of Chemical Physics* **1963,** *38* (11), 2721-2724.

22. Poręba, T.; Ernst, M.; Zimmer, D.; Macchi, P.; Casati, N., Pressure-Induced Polymerization and Electrical Conductivity of a Polyiodide. *Angewandte Chemie* **2019,** *131* (20), 6697-6701.

23. Mao, H. K.; Bell, P. M.; Shaner, J. W.; Steinberg, D. J., Specific volume measurements of Cu, Mo, Pd, and Ag and calibration of the ruby R1 fluorescence pressure gauge from 0.06 to 1 Mbar. *Journal of Applied Physics* **1978,** *49* (6), 3276-3283.

24. Klotz, S.; Chervin, J. C.; Munsch, P.; Le Marchand, G., Hydrostatic limits of 11 pressure transmitting media. *Journal of Physics D, Applied Physics* **2009,** *42* (7), 7.

25. Parsons, S., ECLIPSE- Program for masking high-pressure diffraction images and conversion between CCD image formats. The University of Edinburgh. **2014**.

26. SAINT, Bruker, Bruker AXS Inc., Madison, Wisconsin, USA, 2014/15.

27. SADABS, Bruker, Bruker AXS Inc., Madison, Wisconsin, USA, 2014/15.

28. Sheldrick, G., SHELXT - Integrated space-group and crystal-structure determination. *Acta Crystallographica Section A* **2015,** *71* (1), 3-8.

29. David, W. I. F.; Shankland, K.; van de Streek, J.; Pidcock, E.; Motherwell, W. D. S.; Cole, J. C., DASH: a program for crystal structure determination from powder diffraction data. *Journal of Applied Crystallography* **2006,** *39* (6), 910-915.

30. Sheldrick, G., Crystal structure refinement with SHELXL. *Acta Crystallographica Section C* **2015,** *71* (1), 3-8.

31. Hubschle, C. B.; Sheldrick, G. M.; Dittrich, B., ShelXle: a Qt graphical user interface for SHELXL. *Journal of Applied Crystallography* **2011,** *44* (6), 1281-1284.

32. M. J. Frisch, G. W. T., H. B. Schlegel, G. E. Scuseria, M. A. Robb, J. R. Cheeseman, G. Scalmani, V. Barone, G. A. Petersson, H. Nakatsuji, X. Li, M. Caricato, A. Marenich, J. Bloino, B. G. Janesko, R. Gomperts, B. Mennucci, H. P. Hratchian, J. V. Ortiz, A. F. Izmaylov, J. L. Sonnenberg, D. Williams-Young, F. Ding, F. Lipparini, F. Egidi, J. Goings, B. Peng, A. Petrone, T. Henderson, D. Ranasinghe, V. G. Zakrzewski, J. Gao, N. Rega, G. Zheng, W. Liang, M. Hada, M. Ehara, K. Toyota, R. Fukuda, J. Hasegawa, M. Ishida, T. Nakajima, Y. Honda, O. Kitao, H. Nakai, T. Vreven, K. Throssell, J. A. Montgomery, Jr., J. E. Peralta, F. Ogliaro, M. Bearpark, J. J. Heyd, E. Brothers, K. N. Kudin, V. N. Staroverov, T. Keith, R. Kobayashi, J. Normand, K. Raghavachari, A. Rendell, J. C. Burant, S. S. Iyengar, J. Tomasi, M. Cossi, J. M. Millam, M. Klene, C. Adamo, R. Cammi, J. W. Ochterski, R. L. Martin, K. Morokuma, O. Farkas, J. B. Foresman, and D. J. Fox *Gaussian 09, Revision E.01.*, Gaussian, Inc.: Wallingford CT, 2016.

33. Gavezzotti, A., Calculation of lattice energies of organic crystals: The PIXEL integration method in comparison with more traditional methods. Zeitschrift für Kristallographie **2005,** 220, 499-510.

34. Gavezzotti, A., Non-conventional bonding between organic molecules. The 'halogen bond' in crystalline systems. *Molecular Physics* **2008,** *106* (12-13), 1473-1485.

35. Rocha, I. M.; Ribeiro da Silva, M. D. M. C.; Ribeiro da Silva, M. A. V., Thermodynamic and aromaticity studies for the assessment of the halogen···cyano interactions on Iodobenzonitrile. *The Journal of Chemical Thermodynamics* **2013,** *65*, 204-212.

36. Clark, S. J.; Segall, M. D.; Pickard, C. J.; Hasnip, P. J.; Probert, M. J.; Refson, K.; Payne, M. C., First principles methods using CASTEP. *Zeitschrift für Kristallographie* **2005,** *220* (5-6), 567-570.

37. Dassault Systèmes, BIOVIA, Materials Studio, San Diego, CA, USA. **2017**.

38. Perdew, J. P.; Burke, K.; Ernzerhof, M., Generalized Gradient Approximation Made Simple. *Physical Review Letters* **1996,** *77* (18), 3865-3868.

39. Monkhorst, H. J.; Pack, J. D., Special points for Brillouin-zone integrations. *Physical Review B* **1976,** *13* (12), 5188-5192.

40. Tkatchenko, A.; Scheffler, M., Accurate Molecular Van Der Waals Interactions from Ground-State Electron Density and Free-Atom Reference Data. *Physical Review Letters* **2009,** *102* (7), 073005.

41. Gonze, X.; Charlier, J. C.; Allan, D. C.; Teter, M. P., Interatomic force constants from first principles: The case of alpha-quartz. *Physical Review B* **1994,** *50* (17), 13035-13038.

42. Morris, A. J.; Nicholls, R. J.; Pickard, C. J.; Yates, J. R., OptaDOS: A tool for obtaining density of states, core-level and optical spectra from electronic structure codes. *Computer Physics Communications* **2014,** *185* (5), 1477-1485.

43. Yates, J. R.; Wang, X.; Vanderbilt, D.; Souza, I., Spectral and Fermi surface properties from Wannier interpolation. *Physical Review B* **2007,** *75* (19), 195121.

44. Dolomanov, O. V.; Bourhis, L. J.; Gildea, R. J.; Howard, J. A. K.; Puschmann, H., OLEX2: a complete structure solution, refinement and analysis program. *Journal of Applied Crystallography* **2009,** *42* (2), 339-341.

45. Macrae, C. F.; Edgington, P. R.; McCabe, P.; Pidcock, E.; Shields, G. P.; Taylor, R.; Towler, M.; van de Streek, J., Mercury: visualization and analysis of crystal structures. *Journal of Applied Crystallography* **2006,** *39* (3), 453-457.

46. Spek, A., Structure validation in chemical crystallography. *Acta Crystallographica Section D* **2009,** *65* (2), 148-155.

47. Angel, R., J.; Alvaro, M.; Gonzalez-Platas, J., EosFit7c and a Fortran module (library) for equation of state calculations. *Zeitschrift für Kristallographie* **2014,** *229* (5), 405.

48. Bruno, I. J.; Cole, J. C.; Kessler, M.; Luo, J.; Motherwell, W. D. S.; Purkis, L. H.; Smith, B. R.; Taylor, R.; Cooper, R. I.; Harris, S. E.; Orpen, A. G., Retrieval of Crystallographically-Derived Molecular Geometry Information. *Journal of Chemical Information and Computer Sciences* **2004,** *44* (6), 2133-2144.

49. Bruno, I. J.; Cole, J. C.; Edgington, P. R.; Kessler, M.; Macrae, C. F.; McCabe, P.; Pearson, J.; Taylor, R., New software for searching the Cambridge Structural Database and visualizing crystal structures. *Acta Crystallographica Section B* **2002,** *58* (3 Part 1), 389-397.

50. Groom, C. R.; Bruno, I. J.; Lightfoot, M. P.; Ward, S. C., The Cambridge Structural Database. *Acta Crystallographica Section B* **2016,** *72* (2), 171-179.

51. Schlemper, E. O.; Britton, D., The crystal structure of p-iodobenzonitrile. *Acta Crystallographica* **1965,** *18* (3), 419-424.

52. Desiraju, G. R.; Harlow, R. L., Cyano-halogen interactions and their role in the crystal structures of the 4-halobenzonitriles. *Journal of the American Chemical Society* **1989,** *111* (17), 6757-6764.

53. Merz, K., Substitution Effect on Crystal Packings of Iodobenzonitriles and Iodophenols. *Crystal Growth & Design* **2006,** *6* (7), 1615-1619.

54. Fedorov, A. Y.; Rychkov, D. A.; Losev, E. A.; Zakharov, B. A.; Stare, J.; Boldyreva, E. V., Effect of pressure on two polymorphs of tolazamide: why no interconversion? *CrystEngComm* **2017,** *19* (16), 2243-2252.

55. Funnell, N. P.; Dawson, A.; Marshall, W. G.; Parsons, S., Destabilisation of hydrogen bonding and the phase stability of aniline at high pressure. *CrystEngComm* **2013,** *15* (6), 1047-1060.

56. Espen, E.; K., T. M.; R., M. S.; Jacob, O.; A., S. M.; B., I. B., Structural Collapse of the Hydroquinone–Formic Acid Clathrate: A Pressure-Medium-Dependent Phase Transition. *Chemistry – A European Journal* **2016,** *22* (12), 4061-4069.

57. Taylor, R., Which intermolecular interactions have a significant influence on crystal packing? *CrystEngComm* **2014,** *16* (30), 6852-6865.

Chapter 4

High-Pressure Polymorphism in Pyridine

4.1. Introduction

Pyridine (C_5H_5N) is one of the simplest organic compounds, but its crystal structure at ambient pressure (phase I, $Pna2_1$), determined by Mootz & Wussow,[1] is unusually complicated, with four molecules in the asymmetric unit ($Z' = 4$). A further unusual feature is that it exhibits isotopic polymorphism.[2-4] Phase I is the thermodynamically stable form of isotopically normal pyridine (pyridine-h_5) between the melting point (231 K) and 5 K, and it can be cooled or heated within this range of temperature without undergoing any phase transitions. The same phase is formed by pyridine-d_5 on cooling the liquid below the melting point, and the phase can also be cooled to 5 K. However, on warming from 5 K the structure transforms to the simpler phase II ($P2_12_12_1$, $Z' = 1$) at 170 K. This phase can also be cooled to 5 K, but on warming above 215 K it transforms back to phase I. These observations, combined with calorimetry data, indicate that the thermodynamically stable form of pyridine-d_5 below 215 K is phase II. When phase I persists below this temperature it is metastable, the result of the sluggishness of the I-II transition.

Phase II has never been observed for pyridine-h_5 at ambient pressure, but because it has a smaller molecular volume than phase I, it can be formed at high pressure.[3] We have shown that crystal growth of pyridine-h_5 yields phase I at 0.80 and 1.03 GPa, but phase II at 1.09 GPa. In these experiments, single crystals of pyridine were grown by first compressing the liquid into a polycrystalline mass at the desired pressure using a diamond anvil cell (DAC). The sample was then heated to melt-back the sample to a single crystallite, which was then allowed to grow as the cell cooled back to room temperature (RT). These conditions are, at least approximately, isochoric, *i.e.* pressure is constant during crystal growth.

By contrast, Podsiadło, Jakobek & Katrusiak obtained phase I at 1.23 GPa by high pressure isothermal crystal growth.[5] In these experiments, a stable crystal-liquid equilibrium was established at 1.00 GPa and 295 K. The crystal

was then allowed to grow by carefully increasing the pressure, but holding the temperature constant at 295 K. The sample was found to undergo a phase transition on increasing the pressure to 2.00 GPa which destroyed the integrity of the single crystal.

The apparent difference between our and Podsiadło's pressure conditions is quite small in the context of the precision of the pressure measurements, typically 0.05 GPa, but the difference in the phases obtained is presumably a reflection of the isochoric versus isothermal crystal growth conditions. The crystal formed at 1.00 GPa in the isothermal experiment would have been phase I. Its persistence to 1.23 GPa is likely to be the result of the sluggishness of the phase I to II transition, which is referred to by Podsiadło, and also seen in the low temperature behaviour of pyridine-d_5 where phase I can be supercooled below the I-II transition temperature.[3]

The discoveries of isotopic polymorphism of pyridine at ambient pressure and formation of high-pressure phases of pyridine were first made using vibrational spectroscopy,[4] and the response of pyridine to high pressure has been the subject of a number of more recent infra-red and Raman studies. However, the overall picture that has emerged from these studies is a somewhat confusing one partly because of inconsistent phase numbering.

In their original high-pressure Raman study Heyns & Venter[6] obtained a phase which they referred to as 'phase I' for both the h_5 and d_5 isotopologues at *ca*. 1 GPa. On increasing the pressure they observed discontinuities in the trend of band frequencies versus pressure and the appearance of one new band in pyridine-h_5 and two in pyridine-d_5 which were taken to indicate that this phase transforms to a 'phase II' at 2 GPa.

Heyns and Venter argued that the spectra they obtained for their 'phase I' were too simple to be compatible with the $Z' = 4$, $Pna2_1$ crystal structure of pyridine which had been determined by Mootz & Wussow[1] a few years previously. They do not assign a number to Mootz's $Z' = 4$ phase, and they do

not claim that any of their spectra are consistent with it. In short, Heyns and Venter's paper mentions *three* crystalline phases: a low-temperature/ambient pressure form, another forming on crystallisation at 1 GPa which transforms to a third phase just below 2 GPa. They also mention a glassy form, which is characterised by broader Raman peaks. It seems likely that Heyns and Venter's 'phase I' was what is referred to as 'phase II' in the crystallographic work described above, meaning that their 'phase II' is a higher pressure form whose crystal structure has yet to be determined.

In a later study, Fanetti, Citroni & Bini[7] describe an investigation of pyridine to 25 GPa, showing that above 18 GPa the compound begins to undergo a rearrangement of the primary covalent bonds in which the carbon atoms become sp^3 hybridised. The same behaviour was noted by Zhuravlev and co-workers[8] above 22 GPa. At lower pressures, the phase they reproducibly obtained at between 1.2 and 1.3 GPa, which they label 'phase II', could be compressed up to 18 GPa. Careful peak deconvolution enabled frequencies and intensities to be extracted for 20 out of 21 external modes. The smooth trends in the frequencies of these modes with pressure do not support the phase transitions that had been proposed at 8, 11 and 16 GPa in Zhuravlev 's study.[8]

On decompression to around 1 GPa Fanetti[7] found that 'phase II' transformed to 'phase I'. However, although they define phases I and II to be the same as in the crystallographic work, they also say that the phases they studied had Raman spectra which closely resemble those of Heyns and Venter.[6] Therefore it seems the phases they were in fact studying must have been the two high-pressure forms of Heyns and Venter, *i.e.* the crystallographers' phase II and the structurally uncharacterised form.

We now describe the crystal structure of a second high-pressure form of pyridine, which we, and hopefully everyone else, will refer to as phase III. We go on to show that this phase was the one obtained along with phase II in the high-pressure Raman studies summarised above.

4.2. Experimental

4.2.1. Pyridine-h5-III: Single-Crystal X-Ray Diffraction at 1.69 GPa

Pyridine-h_5 (≥99%, Sigma Aldrich, used a received) was loaded into a Merrill-Bassett DAC[9] along with a ruby sphere. The cell contained 0.6 mm Boehler-Almax cut diamonds[9] and a pre-indented rhenium gasket with a laser-drilled hole of diameter 0.35 mm and height 0.10 mm. Pressures were determined by the ruby fluorescence method.[10]

Phase III was obtained by isochoric *in-situ* crystallisation. The DAC was pressurised to 1.55 GPa forming a polycrystalline solid. The cell was then heated using a hot plate to *ca.* 400 K and slowly cooled to room temperature. This process was repeated until only large single crystals filling the sample chamber remained (**Figure 4.1**). The crystal used for data collection, marked domain 1 in **Figure 4.1(a)**, accounted for about half of the sample volume and was collected at a pressure of 1.69 GPa after the pressure of the cell equilibrated.

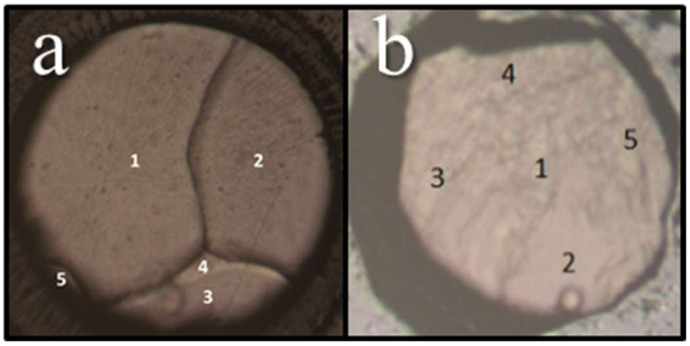

Figure 4.1 Images of the *in-situ* single crystals: a) phase III at 1.69 GPa; and b) phase II 1.09 GPa. The diameter of the gasket hole is 350 μm in (a) and 260 μm in (b).

Pyridine III can also be grown from methanol. The solution used for crystallisation consisted of a 1:1 molar ratio of pyridine (6 ml) and methanol (3 ml). A drop of this solution was placed in a DAC, and crystals were found to form on standing at room temperature and 1.98 GPa over the course of two days. The crystals were melted back to one seed at 423 K and the temperature then

reduced to 403 K at a rate of 2 K min^{-1} to initiate crystal growth. The temperature was then decreased to room temperature at a rate of 0.5 K min^{-1}. The heating and cooling cycles were accomplished using a Cambridge Reactor Design Polar Bear heater that had been adapted to accommodate a Merrill-Bassett DAC.

4.2.2. Pyridine-h_5-II: Single-Crystal X-Ray Diffraction at 1.09 GPa

Pyridine-h_5 was loaded into a Merrill-Bassett DAC as described in Section 4.2.1. The cell design was similar, except that the gasket hole (diameter 0.26 mm) was formed by spark-erosion. The cavity height was 0.10 mm. The sample solidified spontaneously into large single crystal domains on application of a pressure of 1.09 GPa at 293 K. X-ray diffraction data were collected on domain 2 shown in **Figure 4.1(b)**.

4.2.3. Data Collection, Processing and Structure Refinement

High-pressure single-crystal X-ray diffraction data were collected at 293 K on Beamline 12.2.2 at the Advanced Light Source on a custom-built diffractometer with silicon (111) monochromated synchrotron radiation, wavelength 0.4959 Å (E = 25 keV) and a Perkin Elmer amorphous silicon detector. Shutterless ϕ-scans were performed at narrow step widths of 0.25° and wide step widths of 1° in order to minimise overloads and optimize the number of reflections collected across the dynamic range of the detector. The incident beam spot size was 30 μm^2 and was used to probe area 1 in **Figure 4.1(a)** and area 2 in **Figure 4.1(b)**. Beamline calibrations were performed using a NIST single crystal ruby standard prior to high-pressure experiments.

Data were processed using the Bruker Apex suite of programs. Dynamic masks, generated by ECLIPSE,[11] were used to mask shaded areas of the detector and peaks integrated to 0.8 Å using SAINT.[12] Systematic errors, including

scaling, cell and sample absorption and gasket shading were treated using the multi-scan procedure SADABS.[13] Structures were solved using dual-space methods (SHELXT)[14] and refined by full-matrix least-squares on F^2 (SHELXL)[15] using the OLEX2 graphical user interface.[16] The C and N atoms were modelled with anisotropic displacement parameters. H atoms were located in Fourier difference maps, enabling the nitrogen atoms to be identified unambiguously, and constrained to geometrically reasonable positions during subsequent refinement. However, the Flack parameter[17] could not be reliably determined due to low completeness of the high-pressure diffraction experiments and the very small dispersion effects at the X-ray energy used for data collection. Full molecule geometries were checked using MOGUL[18] and structures were visualised using MERCURY,[19] DIAMOND[20] and XP[21]; application of geometric restraints was found to be unnecessary. Crystal and refinement data are listed in **Table 4.1.** Crystallographic Information Files (CIF) are available in the electronic supporting information (ESI).

4.2.4. Raman Spectroscopy

High-pressure Raman spectra were collected on the same samples as used for the single crystal data collections of pyridine-h_5 phases II and III using a Horiba LabRAM HR Evolution Raman Spectrometer equipped with a CCD detector. Raman spectra were measured using a 633 nm excitation laser, with 1200 lines mm^{-1} grating and a spectrometer focal length of 800 mm. Spectra were collected between 50 and 3400 cm^{-1}, with a resolution of 1 cm^{-1}. Raman spectra were collected from a *ca.* 2 micron spot size on static pressure samples at 293 K.

Spectra extracted from the literature were analysed using GetData Graph Digitizer. v2.26.

4.2.5. Decompression of Pyridine III Studied by Raman Spectroscopy

A single crystal of pyridine III was grown *in situ* at 2.50 GPa from a methanol solution and its Raman spectra collected at room temperature as the sample was decompressed to 2.44, 2.28, 1.97, 1.69 and 1.55 GPa. Measurements were performed using a Princeton Instruments Spectra Pro 2500i Raman spectrometer, capable of measuring low range frequencies. Raman spectra were collected between 0 and 500 cm^{-1}, using a 514.5 nm excitation laser, with power, 13 mV and a 1800 grooves mm^{-1} grating.

4.2.6. Equation of State Determinations by Neutron Powder Diffraction

A sample of pyridine-d_5 was loaded into a null-scattering TiZr capsule together with a 1:1 by volume mixture of CaF_2 and powdered silica. Pressure was applied at ambient temperature using a type V3b Paris-Edinburgh (P-E) press[22-23] in which the ram pressure was monitored and adjusted by means of a computer-controlled hydraulic system. The experiment was carried out on the PEARL instrument at the ISIS neutron spallation facility.[24] Pyridine is prone to texture effects, and the silica powder was included with the sample with the aim of minimising these. A phase pure sample of pyridine II was obtained by forming an amorphous solid at 2.7 GPa and then reducing the pressure to 0.942(9) GPa. Further neutron powder diffraction data sets were collected at pressures of 1.09(2), 1.22(3), 1.59(3), 1.83(6) and 2.52(5) GPa. The pattern was much weaker for the last two points, possibly because of the onset of partial amorphisation. The load was reduced and further patterns collected at 1.38(9) and 1.03(2) GPa, the original intensity of the pattern was re-established at the second of these points. Reduction of the pressure to 0.62(6) GPa produced a mixture of phases I and II, becoming pure phase I at 0.45(4) GPa. The contributions of the pyridine phases to the patterns obtained were modelled with the Pawley method, while

those of CaF_2 and the WC and Ni components of the anvils were modelled with the Rietveld method (TOPAS-Academic).[25] The refinements yielded unit cell volumes of CaF_2, which were used to determine the pressures quoted above by applying a third-order Birch-Murnaghan equation of state with values for the bulk modulus (K_0) and its pressure derivative (K') of 81.00 GPa and 5.220, respectively.

A sample consisting of pyridine-d_5 (CDN Isotopes), a small quantity of ground silica wool and a pellet of lead as a pressure marker were loaded into a TiZr capsule and pressure applied as described above on the POLARIS instrument at ISIS. A pattern of phase III was observed at 1.599(19) GPa. Patterns were then measured at 1.914(18), 2.202(14), 2.436(18) and 2.670(16) GPa. The sample was decompressed, with further patterns measured at 1.340(15) and 1.229(15) GPa. A pattern collected at 1.159(20) GPa was a mixture of phases II and III. Data processing was as described above, the K_0 and K' for Pb were taken to be 41.966 GPa and 5.7167.

Table 4.1 Crystal and refinement data. For all structures: C_5H_5N, M_r = 79.10, Z = 4. Experiments were carried out at 293 K with synchrotron radiation, λ= 0.4959 Å using a Perkin-Elmer a-Si Detector. H-atom parameters were constrained.

	Pyridine II at 1.09 GPa	Pyridine III at 1.69 GPa
Crystal data		
Crystal system, space group	Orthorhombic, $P2_12_12_1$	Tetragonal, $P4_12_12$
a, *b*, *c* (Å)	5.392 (3), 6.806 (3), 11.261 (5)	5.4053 (4), 5.4053 (4), 13.4853 (14)
α, β, γ (°)	90, 90, 90	90, 90, 90
V (Å^3)	413.2 (3)	394.00 (7)
μ (mm^{-1})	0.04	0.04
Crystal size (mm)	0.26 × 0.26 × 0.1	0.35 × 0.35 × 0.1
Data collection		
Absorption correction	Multi-scan	Multi-scan
T_{min}, T_{max}	0.484, 0.744	0.585, 0.745
No. of measured, independent and observed [$I > 2\sigma(I)$] reflections	1324, 411, 291	1328, 326, 297
R_{int}	0.033	0.061
$(\sin\theta/\lambda)_{max}$ (Å^{-1})	0.625	0.625
Refinement		
$R[F^2 > 2\sigma(F^2)]$, $wR(F^2)$, *S*	0.029, 0.060, 0.88	0.076, 0.196, 1.14
No. of parameters	56	30
Completeness	52%	77%
$\Delta\rangle_{max}$, $\Delta\rangle_{min}$ (e Å^{-3})	0.04, -0.05	0.25, -0.30
Absolute structure parameter	10.0 (10) [inconclusive]	-10.0 (10) [inconclusive]

4.2.7. PIXEL and Symmetry-Adapted Perturbation Theory Calculations

Molecular electron densities were obtained using the program GAUSSIAN09 revision A.02[26] at the MP2 level with the 6-31G** basis set. The electron density was then analysed using the PIXELc module of CLP program package which allows the calculation of dimer and lattice energies.[27-29] Symmetry-adapted perturbation theory calculations were carried out with the PSI-4 code (version Beta5) using the SAPT2+3 method[30-31] with the aug-cc-pVDZ basis set. δE_{HF} [32] corrections were applied to induction energies in all cases.

4.2.8. Periodic Density Functional Theory (DFT) Calculations

Geometry optimisations were carried-out using the plane-wave pseudopotential method in the CASTEP code[33] as incorporated into Materials Studio.[34] The PBE exchange-correlation functional was used with norm-conserving pseudopotentials and a basis set cut-off energy of 920 eV.[35] Brillouin zone integrations were performed with a Monkhorst-Pack **k**-point grid spacing of 0.07 $Å^{-1}$.[36] The starting coordinates were taken from the single-crystal diffraction studies of Sections 4.2.1 and 4.2.2 and optimised using the Tkatchenko-Scheffler correction for dispersion (DFT-D).[37] The cell dimensions were fixed to the experimental values, and the space group symmetry was retained. The energy convergence criterion was $1x10^{-8}$ eV/atom, with a maximum force tolerance of 0.001 eV $Å^{-1}$ and a maximum displacement of $1x10^{-5}$ Å; the SCF convergence criterion was $1x10^{-10}$ eV/atom. Frequencies were calculated[38] at the Γ-point only for the h_5 isotopologues as the results were intended for comparison with the experimental Raman spectra.

4.3. Results and Discussion

4.3.1. Formation of Pyridine III

Prior to this work pyridine was acknowledged to form crystalline phases I ($Pna2_1$ Z' = 4) and II ($P2_12_12_1$ Z'=1) as well as an amorphous form.[1, 4-8] The present results yield the structural and spectroscopic characterisation of a third crystalline form, designated phase III ($P4_12_12$, Z' = ½). Crystals of phases II and III were grown from pure pyridine-h_5 by *in situ* crystallisation at 1.09 and 1.69 GPa, respectively using the 'approximately isochoric' procedure described in Sections 4.2.1 and 4.2.2. Phase III can also be obtained by crystallisation of pyridine from a solution in methanol, though this procedure can also lead to formation of a methanol solvate.[5]

Dunitz and Schweizer [39-40] have drawn attention to the tendency for approximately hexagonal molecules with C_{2v} point symmetry to crystallise in space group $P4_12_12$ (or equivalently $P4_32_12$) with unit cell dimensions in the region of a = 6 Å and c = 14 Å. Examples include alloxan (a = 5.84 Å, c = 13.85 Å) and fluorobenzene (a = 5.80 and c =14.51 Å). Pyridine III conforms to this pattern, with a = 5.4053(4) and c = 13.44853(14) Å at 1.69 GPa. The X-ray powder pattern for a polymorph of benzene which exists between 1.4 and 4 GPa,[41] which seems somewhat elusive, is generally discussed only in computational studies,[42-43] and is often but not always referred to as phase II, can be indexed with a tetragonal unit cell of dimensions a = 5.29 and c = 14.29 Å at 3.1 GPa.[42]

The unusual characteristics of crystalline pyridine have inspired a number of crystal structure prediction studies.[44-47] In the most recent of these[44], Aina *et al*. generated a force field that was trained using energies calculated with symmetry adapted perturbation theory (SAPT) for gas-phase dimers. The results enabled them to identify the structure of phase III being reported here in an energy landscape calculated at 2 GPa.

4.3.2. The Crystal Structure of Pyridine III and its Relationship with Pyridine II

In phase III the 2-fold axis of the pyridine molecule is constrained to lie along the ..2-fold axis of the space group ($P4_12_12$), and only the orientation of the molecule about this axis is unconstrained by symmetry (**Figure 4.2(a)**). Relative to a Cartesian model with the 2-fold axis along **z** and the molecule in the **xz** plane the orientation in the unit cell is obtained by rotations of 90°, 136.9(3)° and –45° about **a**, **b** and **c**. Pyridine II crystallises in $P2_12_12_1$, which is a sub-group of $P4_12_12$. The cell dimensions are similar to phase III, a = 5.64735(2), b = 6.98010(3) and c = 11.46495(5) Å at ambient pressure and 195 K; corresponding values at RT and 1.38 GPa are 5.392(3), 6.806(3) and 11.261(5) Å. The molecular orientation parameters at 195 K are similar to those in phase III, 93.11(5)°, 130.09(3)° and –46.22(4)°. The rings in phase II are more perpendicular to the c axis, which is therefore shorter than in phase III (**Figure 4.2(b)**) so that pyridine can be said to display negative linear compression at the II/III phase boundary. There is no suggestion that pressure distorts the intramolecular geometry, as was the case for example in syn-1,6:8,13-biscarbonyl[14]annulene.[48]

Topological analysis indicates that phase II has 14 molecules in its first coordination sphere with 50 and 110 molecules in the second and third coordination spheres, respectively (Calculated using TOPOS-PRO).[49] This '14-50-110' coordination sequence is characteristic of body-centred cubic packing topology (*bcu-x* in the notation of Reticular Chemistry Structure Resource (RCSR) topological database).[50-51] Phase III is characterised by a coordination sequence of 12-42-92, which corresponds to cubic close packing (RCSR symbol *fcu*), indicating that the effect of higher pressure is to eject two molecules from the coordination sphere of phase II to generate a more close-packed topology (see **Figure 4.3**).

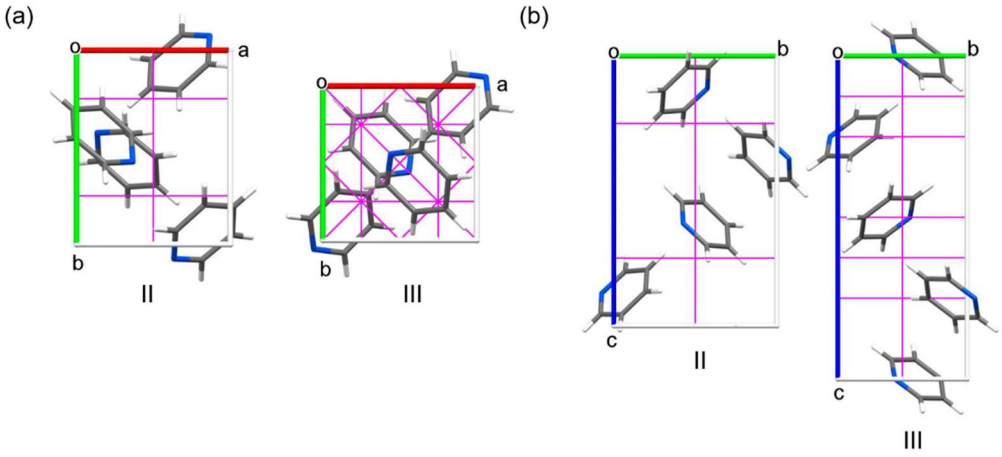

Figure 4.2 Crystal packing in pyridine II ($P2_12_12_1$) and III ($P4_12_12$) as viewed in (a) the *ab*-plane and (b) the *bc*-plane. Crystallographic 2-fold rotation axes are shown as pink lines.

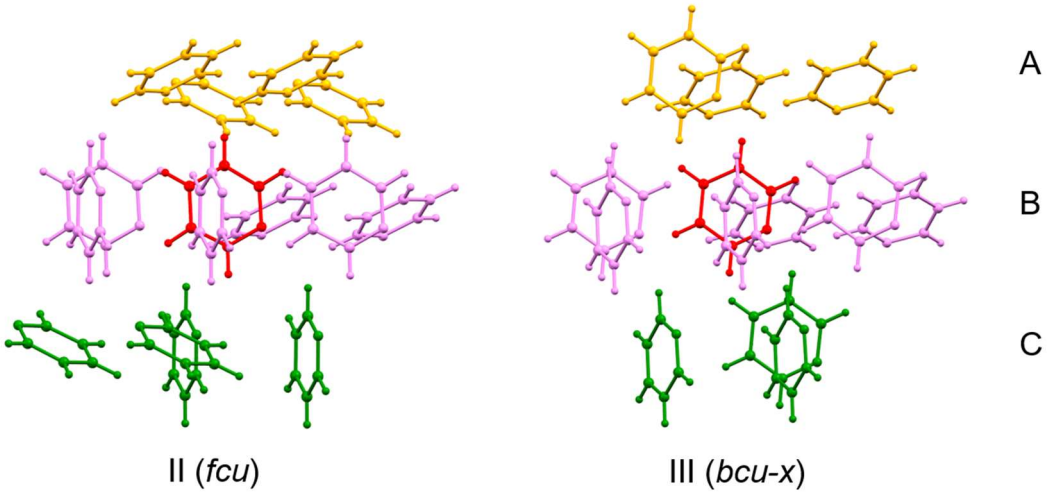

Figure 4.3 Pyridine II and III with different topology of molecular packings: (left) *fcu* with molecular coordination number (MCN) = 14; (right) *bcu-x* with MCN = 12. The central molecule is highlighted in red. The A layers are orange, B layers are violet and C layers are green.

Intermolecular interaction energies were calculated using the PIXEL method and symmetry-adapted perturbation theory at the SAPT2+3 level (**Tables 4.2** and **4.3**). The total contact energies obtained in the two sets of calculations are in excellent agreement, with the maximum difference being 1.3 kJ mol^{-1} for a CH···π contact in phase III. Aina[44] identified eight pyridine dimers as potential energy minima in the gas phase. The dimers are linked by CH···N, CH···π or stacking interactions and have energies in the range –14.31 to –16.56 kJ mol^{-1}. These energies are systematically more negative (i.e. more stabilising) than those listed in **Tables 4.2** and **4.3** because they are optimised potential energy minima for the isolated dimers in question. As Dunitz has pointed out,[39-40] the dimers observed in crystal structures are a compromise between all the interactions formed. The crystalline dimer geometries are distorted away from those of the ideal gas phase minima, and their energies are correspondingly more positive. This observation is surely even more pertinent for high-pressure crystal structures, and is even true of Aina *et al.*'s predicted crystal structures. Both the PIXEL and SAPT methods break down the total energies into electrostatic, polarisation, dispersion and repulsion terms, and while there is more variation between PIXEL and SAPT in the component energies than in the total energies, it is clear from both calculations that dispersion is the dominant term in all contacts. This finding is in agreement with Aina *et al.*'s and Gavezzotti's results.[44, 46]

The first coordination spheres of both phases II and III contain 12 molecules with centroid-centroid distances between *ca*. 4.5 and 6 Å. An additional pair of contacts form at distances of 6.8 Å in phase II and 7.1 Å in phase III. The increase in these longer contact distances for phase III is the reason the packing topology changes from *fcu* to *bcu-x*. Equivalent contacts in the two phases are correlated in **Figure 4.4(a)** and **(b)**, and **Tables 4.2** and **4.3**, where molecules in related positions in the two phases carry the same label. In **Figure 4.4(b)** (phase–III) the 12 contacts between 4.5 and 6 Å are labelled A-L, with the two longer (6.8 Å) interactions labelled M and N. In phase II

(**Figure 4.4(a)**) molecules M and N move into the first coordination sphere, lengthening the contacts to molecules I and L. The displacement of molecules I and L by molecules M and N is shown more clearly in the animation "*a*_axis.gif" in the ESI. The molecule coloured in red is the central molecule of the coordination spheres in **Figures 4.4 (a)** and **(b)**. The animation is generated from symmetry mode analysis of the phase III to II transition obtained on decompression (Section 4.3.5) with the assumption that the coefficients of the irreducible representations vary linearly over the course of the transition. The animation therefore should not be interpreted as the 'mechanism' for the transition. We did not observe a phase II to III phase transition directly during compression measurements.

The twelve strongest contacts comprise six pairs of symmetry-related contacts in phase II and three sets of four in phase III. The molecule-molecule energies range between –12.4 and –4.6 kJ mol^{-1} in phase II and –9.0 and –7.1 kJ mol^{-1} in phase III (SAPT values). Three classes of contacts are formed. One class (contacts E-H) is characterised by intermolecular CH···N interactions with H···N distances of between 2.58 and 2.76 Å and centroid-centroid distances near 6 Å. Dispersion is the largest term in these contacts, but the Coulombic contribution is also significant. A second (contacts A-D) consists of CH···π interactions with centroid-centroid distances of around 4.5 Å and CH···ring centroid distances of between 2.57 and 3.12 Å. The magnitudes of the Coulombic energies in these contacts are only about 20-30 % of the dispersion energies. A third set of interactions (I-L in phase III and J, K, M and N in phase II) with centroid-centroid distances of 5.39 to 5.86 Å, are dominated by dispersion with very little Coulombic energy and a lack of any distinctive atom-atom contacts. Note that the π···π contacts which potentially form stabilising gas-phase dimers (see above) do not occur in either phase.

In the transition between phases I and II CH···N contacts are replaced by CH···π interactions. By contrast, the correlations shown in the animation (*a*_axis.gif) and in **Figure 4.4** show that nature of each interaction remains

constant over the course of the transition between phases II and III, so that CH···N contacts in one phase transform in to CH···N contacts in the other *etc*., but the distances and energies change. The lack of a characteristic geometric signature for contacts I-L gives them a degree of flexibility allowing them to accommodate the biggest changes during the transition.

4.3.3. Equations of State of Pyridine II and III

The variation of unit cell volume with pressure for pyridine II and III, as determined using neutron powder diffraction, were fitted to third-order Birch-Murnaghan equations of state using the EoSFIT7 code,[52] and given in **Figure 4.5.** The number of points obtained is quite limited with pressures starting at *ca.* 1 GPa, and it was not possible to refine values of the zero-pressure cell volume (V_0), the bulk modulus (K_0) and its pressure derivative (K') simultaneously. V_0 was therefore fixed at 452 Å^3, the volume of pyridine II at 195 K. K_0 for phase II was found to be 6.4(3) GPa with K' = 8.7(10). Corresponding figures for phase III are 6.2(3) GPa and 8.1(9). The two sets of parameters are the same within their uncertainties. The consistently lower volume of phase III is consistent with it becoming the more stable phase at elevated pressure. The higher density of phase III is consistent with its more close-packed topology.

A small bulk modulus (<10 GPa) is typical of soft materials where dispersion forces dominate intermolecular interactions *e.g.* naphthalene and $Ru_3(CO)_{12}$ have values of 8.3(4) and 6.6 GPa, respectively.[53-54] Flexible intramolecular torsion angles can provide an additional mechanism for compression, as seen in the P and OP polymorphs of the prodigiously polymorphic compound 'ROY' (5-methyl-2-[(2-nitrophenyl)amino]-3-thiophenecarbonitrile), for which K_0 is 6.0(7) and 4.3(3) GPa, respectively.[55-56] It assumes a higher value if additional intermolecular interactions such as H–bonding is present, *e.g.* the value for hydroquinone-formic acid clathrate, melamine and L-alanine are 13.6(4) GPa,[57] 12.0(5)[58] and 13.4(7) GPa,[59]

respectively. Materials characterised by a mixture of dispersion and weaker H-bonds have correspondingly lower bulk moduli, *e.g.* aniline (phase II) is 5.4(2) GPa. [60]

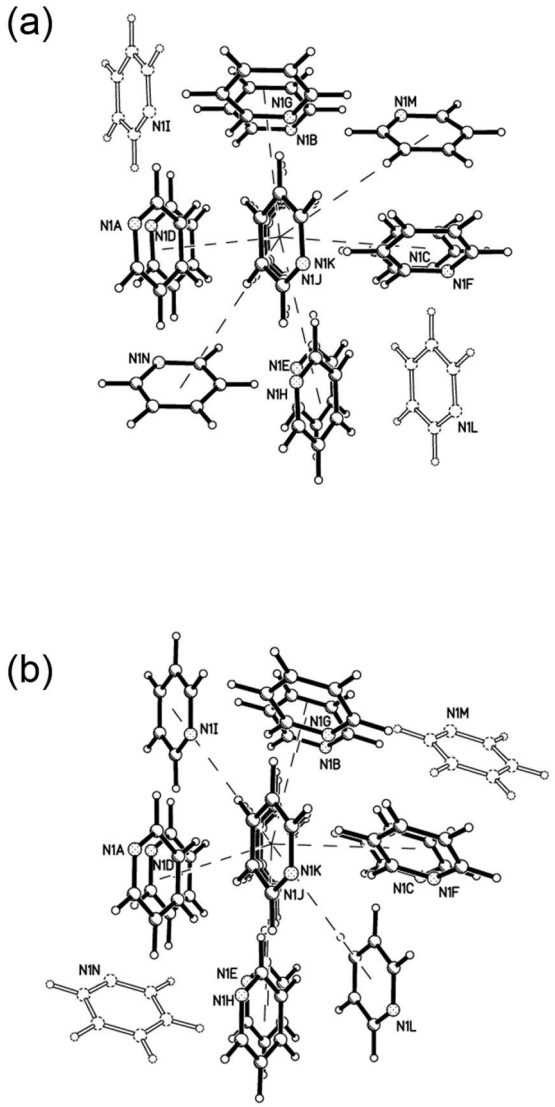

Figure 4.4 The first coordination spheres of **(a)** pyridine II at 1.09 GPa and **(b)** pyridine III at 1.69 GPa. Nitrogen atoms (NI) of each molecule are labelled A–N in order of increasing energy with energetic breakdowns given in **Tables 4.2** and **4.3.** The molecules described in the text as making long interactions are shown in outline.

Table 4.2 Intermolecular contacts in pyridine III. All energies are in kJ mol^{-1}. Intramolecular C-H and N-H distances were constrained to 1.09 and 1.05 Å, respectively in the H-normalised structures. All hydrogen contact distances given are those of the H-normalised structures.

Label	Centroid Distance (Å)	Symmetry		Coulombic	Polarization	Dispersion	Repulsion	Total	Contacts
A	4.466	x+1/2, –y+1/2, –z+3/4	PIXEL	–5.3	–3.5	–18.2	19.3	–7.7	C3H3···π = 2.57 Å
B		–x+1/2, y–1/2, –z+5/4	SAPT2+3	–8.4	–3.2	–23.7	26.2	–9	
C		–x+1/2, y+1/2, –z+5/4							
D		x–1/2, –y+1/2, –z+3/4							
E	6.094	x–1/2, –y+3/2, –z+3/4	PIXEL	–5.6	–3.8	–12	13.1	–8.3	C2H2···N1 = 2.69 Å
F		–x+3/2, y+1/2, –z+5/4	SAPT2+3	–6.8	–3	–13.8	16	–7.6	
G		–x+3/2, y–1/2, –z+5/4							
H		x+1/2, –y+3/2, –z+3/4							
I	5.410	x, y–1, z	PIXEL	–2.2	–1.5	–10	6.9	–6.9	Non–specific dispersion:
J		x+1, y, z	SAPT2+3	–4.7	–1.9	–13.4	12.9	–7.1	highly slipped stack, β=61°.
K		x–1 , y, z							Interplane distance = 2.64 Å
L		x, y+1, z							
M	7.111	–x+1, –y+1, z+1/2	PIXEL	0	–0.1	–1	0	–1	Long range dispersion,
N		–x+1, –y+1, z–1/2	SAPT2+3	0.1	–0.1	–1.5	0.1	–1.4	H···H = 4.23 Å

Table 4.3 Intermolecular contacts in pyridine II. All energies are in kJ mol^{-1}. Intramolecular C-H and N-H distances were constrained to 1.09 and 1.05 Å, respectively in the H-normalised structures. All hydrogen contact distances given are those of the H-normalised structures.

Label	Centroid Distance (Å)	Symmetry		Coulombic	Polarization	Dispersion	Repulsion	Total	Contacts
A	4.501	x+1/2, –y+1/2, –z	PIXEL	–3.5	–2.3	–15.1	12.9	–7.9	Long C3H3···π = 3.03 Å &
D		x–1/2, –y+1/2, –z	SAPT2+3	–6.4	–2.6	–20.3	21.1	–8.2	Long C4H4···π 3.12 Å
B	4.696	–x, y–1/2, –z+1/2	PIXEL	–5	–2.8	–15.7	13.7	–9.7	C5H5···π = 2.71 Å
C		–x , y+1/2, –z+1/2	SAPT2+3	–7.2	–2.6	–19.9	19.9	–9.8	
E	5.949	x–1/2, –y+3/2, –z	PIXEL	–7.9	–3.5	–12.2	12.5	–11.1	C2H2···N1 = 2.58 Å
H		x+1/2, –y+3/2, –z	SAPT2+3	–10.8	–3.5	–14.6	18.1	–10.8	
F	5.88	–x+1, y+1/2, –z+1/2	PIXEL	–7.1	–2.8	–10.7	8.5	–12.2	C6H6···N1 = 2.76 Å
G		–x+1, y–1/2, –z+1/2	SAPT2+3	–10	–2.7	–13.5	13.8	–12.4	
I	6.806	x, y–1, z	PIXEL	0	–0.1	–1.1	0	–1.2	Long range dispersion,
L		x, y+1, z	SAPT2+3	0	–0.1	–1.7	0.1	–1.8	H2···H5 = 4.75 Å
J	5.392	x+1, y, z	PIXEL	–1.2	–1.3	–9	5.4	–6.2	Highly offset stack. No overlap.
K		x–1, y , z	SAPT2+3	–3.3	–1.7	–12.6	11	–6.6	Shortest contact, H4···H6 = 2.74 Å
M	5.856	–x+1/2, –y+1, z+1/2	PIXEL	–0.6	–0.9	–8.6	4.7	–5.4	Non-specific dispersion, H2···H5 2.51 Å,
N		–x+1/2, –y+1, z–1/2	SAPT2+3	–1	–0.9	–9.6	6.9	–4.6	H6···H2 2.69 Å & H6···H3 2.62 Å

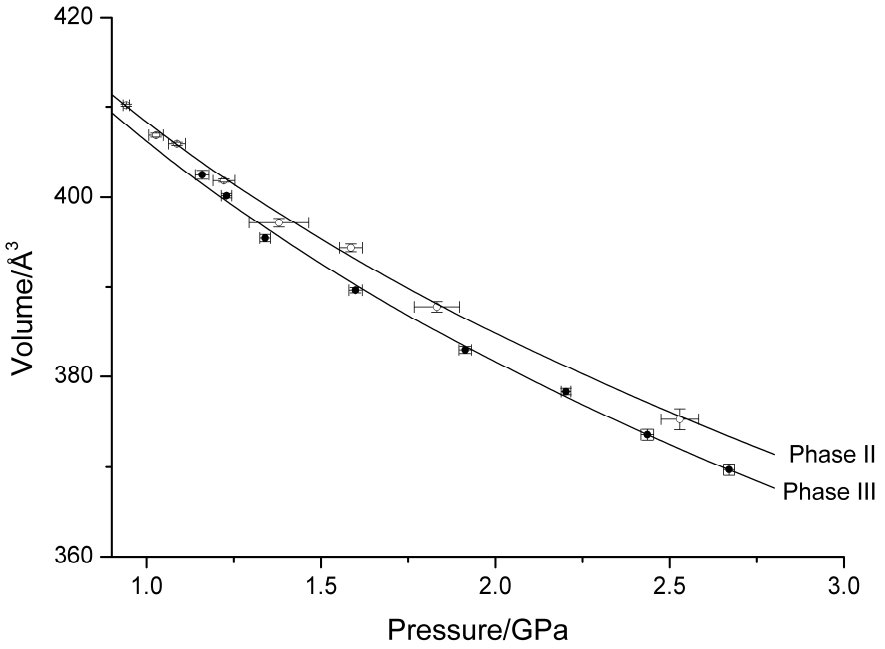

Figure 4.5 Variation of the unit cell volumes of pyridine-d_5 phases II (open circles) and III (closed circles) with pressure fitted to third order Birch-Murnaghan equations of state.

4.3.4. Raman Spectra

The inconsistencies in the literature regarding the assignment of Raman spectra of the different high-pressure forms of pyridine were described in Section 4.1. With the aim of resolving the ambiguities, Raman spectra were measured on the exact same samples of phases II and III as had been used for X-ray data collections. The region of the spectrum below 200 cm^{-1}, which contains the external or 'lattice' modes, has been discussed in earlier work, and the data obtained in this region in the present study are shown in **Figure 4.6** and compared to each other and to those found in the literature in **Table 4.4.**

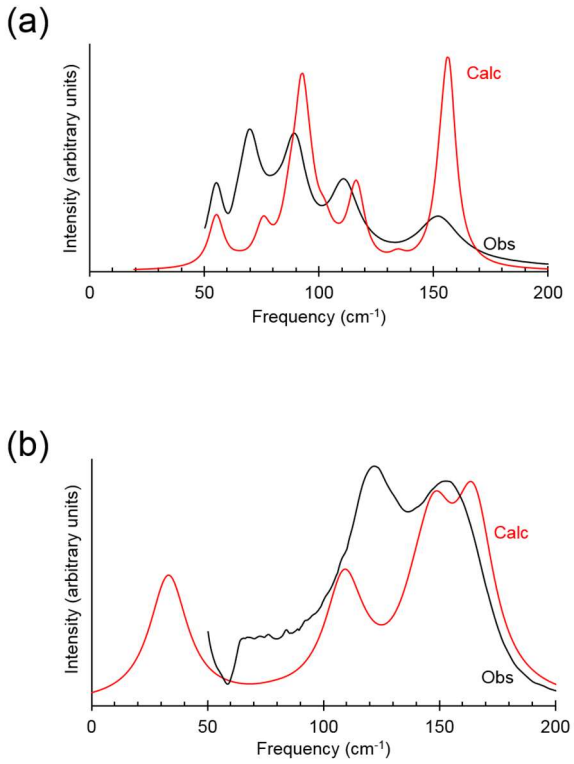

Figure 4.6 The Raman spectra in the lattice phonon region of (a) phase II at 1.09 GPa and (b) phase III at 1.69 GPa, collected on the same regions as the diffraction data. Observed data in black and DFT-calculated data in red.

The Raman spectrum of phase II ($P2_12_12_1$) has five bands below 200 cm^{-1} matching the spectrum collected at 1 GPa by Heyns & Venter, shown at the far left of Figure 1 in their paper.[6] The spectrum of Phase III ($P4_12_12$) is quite different, with two distinct bands matching the (quite broad) spectra measured at above 1.7 GPa by Fanetti *et. al.*,[7] at 2 GPa by Zhuravlev *et al.*,[8] and at 2.5 GPa by Heyns and Venter (Figure 1, far right spectrum in their paper).[6] The band below 50 cm^{-1}, is discussed in Section 4.3.5.

The frequencies of the Raman modes observed for phases II and III are reproduced to within 10 cm^{-1} in periodic DFT calculations without any need for frequency scaling. The intensities of the bands are more poorly reproduced, though discrepancies between calculated and experimental Raman spectra of molecular materials have been noted previously, *e.g.* for tetracene.[61] The

calculations enable the modes to be assigned to oscillations about axes lying in the planes of the pyridine molecules.

It is clear from these data that the 'phase I' of Heyns and Venter is actually the $Z' = 1$, $P2_12_12_1$ phase–II, while the 'phase II' of Fanetti *et al.* and Zhuravlev *et al.* is the $Z' = ½$, $P4_12_12$ phase III. Interestingly, the sharpest spectrum of pyridine-h_5 recorded at 2.5 GPa by Heyns & Venter contains additional bands between 57 and 108 cm^{-1} which are neither seen in Fanetti's and Zhuravlev's spectra nor by us in our experimental or calculated spectra. It is anomalous that an increase in crystallographic symmetry should give rise to a more complex Raman spectrum, and it seems possible that their sample was contaminated with phase II.

Table 4.4 Comparison of the Raman lattice modes in pyridine II and pyridine III in this study and in the literature.

Pressure/ GPa	Reference	Phase assigned by authors	Proposed phase	Lattice modes/cm^{-1}
1.0	Heyns and Venter[6] Table 3 (Fig.1 left panel)	I	II	60(-), 72(71), 85(89), 91(-), 111(110), 153(152)
1.09	This study, experimental	II	II	55, 70, 89, 111, 152
1.09	This study, DFT	II	II	56, 76, 93, 116, 136 (weak), 156
1.69	This study, experimental	III	III	123, 141 (sh), 154
1.69	This study, DFT	III	III	33, 110, 148, 164
1.7	Fanetti *et al.*[7] Fig. 1	II	III	126, 163
2.0	Zhuravlev *et al.*[8] Fig. 4	II	III	130, 165
2.5	Heyns and Venter [6] Table 3 (Fig. 1 left panel)	II	II/III mixture	57(57), 69(69), 87(88), 96(-), 108(108), 142(142), 187(187)

Lattice mode assignment was not reported consistently between Heyns and Venter's Table 3 and Figure 1 in reference [6]. The lattice modes given in brackets here are the values given by Heyns and Venter in their Figure 1.

4.3.5. Decompression of Pyridine III and Symmetry Mode Analysis

The unit cells of phase II and III characterise similar translational symmetry, but the structures differ in the relative orientations of the molecules (Section 4.3.2); the transition between phases III and II therefore occurs at the Γ-point of reciprocal space. Symmetry mode analysis (ISODISTORT)[62-63] indicates that the transition is governed by molecular rotations belonging to the totally symmetric Γ_1 (A_1 in Mulliken notation) and the Γ_2 (B_1 or B_2 depending on axis definitions) irreducible representations. The A_1 mode rotates the pyridine molecules about their two-fold axes, and activation of this mode does not lower the space group symmetry. The B_2 mode causes the two-fold molecular axes to deviate from the crystallographic ..2-fold axes (see Section 4.3.2) and causes the space group of the crystal structure to drop from $P4_12_12$ to $P2_12_12_1$.

The lowest Γ-point vibrational frequencies in pyridine III have the same symmetries and mode characteristics. The DFT calculations of **Figure 4.6** indicate that the A_1 vibrational mode can be observed by Raman spectroscopy in phase III at 33 cm^{-1}. The B_2 mode (52 cm^{-1}), though formally Raman active, is predicted to have zero intensity. Neither mode is observable by infrared spectroscopy.

A single crystal of pyridine III was grown by high-pressure *in-situ* crystal growth from methanol and Raman measurements were performed in the region below 200 cm^{-1} on decompression from 2.50 to 1.69 GPa (**Figure 4.7**). All of the spectra have high luminescence backgrounds, which becomes more prominent on decreasing pressure, and are still present after background corrections and spectral averaging.

The spectrum collected at 2.50 GPa is that of pyridine III. There is a single strong band at 57 cm^{-1}, which, on the basis of the DFT calculations is assigned to the A_1 mode described above. The frequency is somewhat higher than had been calculated for the structure at 1.69 GPa (33 cm^{-1}, **Table 4.4**), but is

in very good agreement with a frequency calculation based on the cell dimensions measured at 2.67 GPa (60 cm^{-1}).

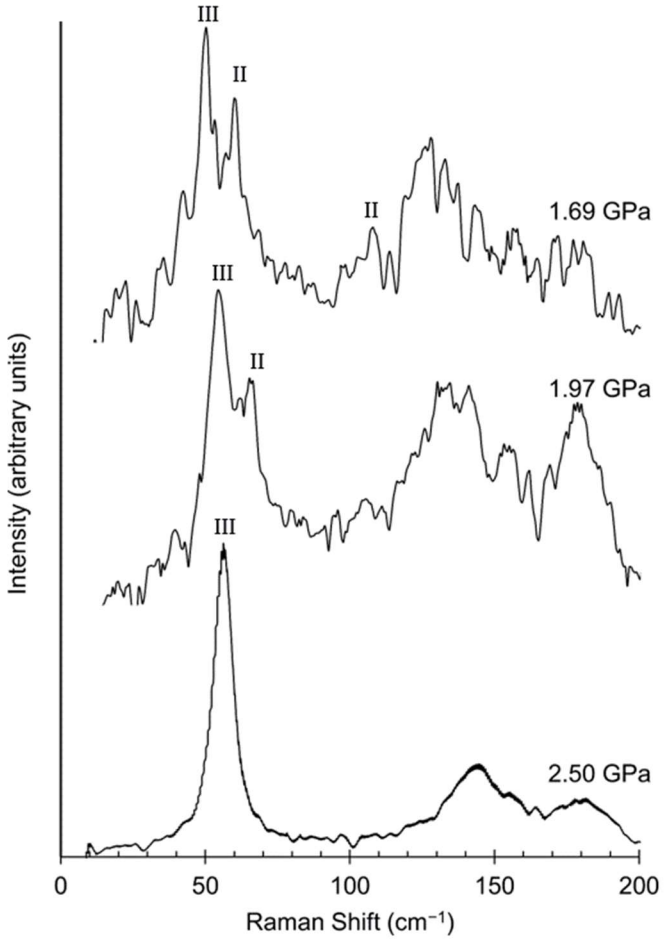

Figure 4.7 Raman spectra of the decompression of pyridine III to a pyridine III/II mixture.

The onset of the pyridine III to II phase transition can been seen on decompression from 2.50 to 1.97 GPa from the emergence of the phase II band at 71 cm^{-1} (*cf.* **Table 4.4**). The intensity of this band increases at 1.69 GPa and an additional band beginning to grow-in at 100 cm^{-1} is also consistent with the formation of phase II. Further decompression (to 1.55 GPa) led to dissolution of the pyridine in the methanol and a noisy luminescence spectrum from which no discernible Raman data could be extracted. These data show that the transition between phases III and II does not occur sharply, but gradually occurs

as pressure is reduced, an observation that is consistent with the sluggishness of the transition between phases I and II in pyridine-d_5 as a function of temperature. The mixture of phases is also consistent with the spectrum of phase III obtained by Heyns and Venter (see above).[6]

The B_2 vibration is expected to act as a soft mode, but since it is not observable by optical spectroscopy its frequency has been calculated using periodic DFT using cell dimensions observed for phase III at selected pressures, with three extra points at 0, 0.25 and 0.50 GPa inferred from the equation of state. The variation (**Figure 4.8**) shows a rapid softening of the mode as pressure is reduced. The transition pressure calculated to occur at about 1 GPa lower than observed experimentally. The difference may of course be related to approximations in the calculations, for example the assumption of harmonic behaviour. Alternatively, it may imply that the transition initiates at crystal defects, where the local pressure would be expected to be lower, and proceeds via the nucleation and growth mechanism usually associated with reconstructive transitions.

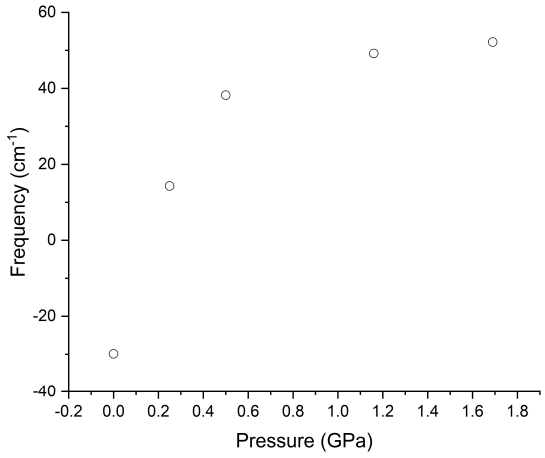

Figure 4.8 Variation of the frequency of the of the B_2 symmetry-breaking lattice mode as a function of pressure. Frequencies calculated by periodic DFT.

4.4. Conclusions

The Cambridge Database[64] (established 1965) just celebrated its millionth entry. Of these, about 5000 structures resemble pyridine I in having four molecules in the asymmetric unit. Only around 1200 have *Z*' greater than this. Steed and Steed[65] have identified a number of factors that may promote formation of crystal structures with more than one molecule in the asymmetric unit. While the phenomenon is slightly more common in small molecules than in larger ones,[66-67] in the case of pyridine I it appears that the reason lies in the energetic competitiveness of CH···N and CH···π interactions.[3, 44] Chains of molecules in pyridine I are formed by a mixture of these interactions.[3] A small amount of pressure, of the order of 1 GPa, is enough to convert the CH···π into CH···N contacts, forming *Z*' = 1 phase II.

Phase II has a lower molar volume than phase I and the transition between the two is driven by the influence of the pressure × volume contribution to free energy, which favours efficient packing. A similar feature was observed in methyl 2-(carbazol-9- yl)benzoate, where a *Z*' = 8 ambient pressure form converts to a *Z*'= 2 form at 5.3 GPa by selection of lower-volume molecular conformations.[68] In isopropanol the same factor applies, but in this case it leads to an *in*crease in *Z*' from 3 to 4 at 1.1 GPa as the structure sacrifices H-bond linearity to improved packing efficiency.[69]

Increasing the crystallisation pressure from 1.1 GPa to 1.7 GPa leads to the formation of pyridine III. The underlying close-packed topology of this polymorph gives it a yet lower volume than pyridine II, which has a body-centred cubic topology. Fanetti *et al.*'s Raman data[7] show that phase III persists all the way to 18 GPa; the additional phases proposed by Zhuravlev *et al.*[8] were not reproduced in Fanetti's work.

In the light of our combined crystallographic and Raman data obtained both Heyns and Venter's, Fanetti *et al.*'s and Zhuravlev *et al.*'s phases I and II are phases II and III, respectively. Phase I does not feature in any of these papers.

There is no rational geometric relationship between the crystal structures of pyridine I and II, and there is no group-subgroup relationship between their space groups ($Pna2_1$ and $P2_12_12_1$). The transition between the two can be studied thermally provided the perdeuterated isotopologue is used, but the transition causes a single crystal of phase I to break into fragments. The only crystallographically verified report of phase I being formed at high pressure is in Podsiadło's study, in which it was formed by isothermal crystal growth at 1.2 GPa and room temperature.[5] Increasing the pressure on this sample to 2 GPa caused it to break up. It was assumed at the time that phase II had formed, but the pressure implies that it could have been phase III.

Phases II and III are geometrically much more closely related than phases I and II, and a group-subgroup relationship exists between their space groups ($P2_12_12_1$ and $P4_12_12$). The transition between phase III to II is displacive and governed by mode-softening. The soft mode cannot be observed experimentally by Raman or infrared spectroscopy, but it was inferred by a combination of symmetry mode analysis of the crystal structures and periodic DFT calculations. However, the transition is not concerted, and it may proceed via nucleation at defects.

The transition between phase III and II can be reproducibly observed by releasing pressure: in this work its onset was observed as pressure was reduced from 2.5 to 1.97 GPa (**Figure 4.7**), in Fanetti's work it was observed at 1 GPa. The expected transition from phase II to phase III on pressure increase is less reproducibly observed. Both Heyns and Venter, and Zhuravlev *et al.* observed it. However, Fanetti *et al.* were able to compress phase II to 9.4 GPa, while in this work we compressed a sample of the deuterated isotopologue to 2.5 GPa, albeit with some reversible amorphisation.

The variability of the transition pressures and sequences quoted above indicate that kinetics are an important factor in the phase behaviour of pyridine, and authors frequently remark on the sluggishness of its phase transitions. This

even extends to the melting transition. Although the melting pressure of pyridine is 0.55 GPa, crystallisation is only ever observed at around 1 GPa or above.[5, 7] Crystal growth often has to be induced by increasing pressure in small increments or with thermal annealing, and pyridine is highly susceptible to the formation of glassy or amorphous phases. Fanetti's paper illustrates featureless Raman spectra up to 1.6 GPa, while we failed to see any evidence of crystalline diffraction at pressures as high as 2.7 GPa, the sample only crystallising on release of pressure. Similar features characterise the phase behaviour of benzene.[5, 41, 70-71]

To summarise, phase II and III can both be accessed reproducibly by crystal growth directly from the liquid phase. Phase II can also be accessed by decompression of phase III or from decompression of a pressure-amorphised sample. The sequence of phases I → II → III has never been observed at high pressure in a single sample.

4.5. References

1. Mootz, D.; Wussow, H. G., Crystal structures of pyridine and pyridine trihydrate. *The Journal of Chemical Physics* **1981,** *75* (3), 1517-1522.

2. Merz, K.; Kupka, A., Deuterium Perturbs the Molecular Arrangement in the Solid State. *Crystal Growth & Design* **2015,** *15* (4), 1553-1558.

3. Crawford, S.; Kirchner, M. T.; Blaeser, D.; Boese, R.; David, W. I. F.; Dawson, A.; Gehrke, A.; Ibberson, R. M.; Marshall, W. G.; Parsons, S.; Yamamuro, O., Isotopic polymorphism in pyridine. *Angewandte Chemie, International Edition* **2009,** *48* (4), 755-757.

4. Castellucci.E; Sbrana, G.; Verderame, F. D., Infrared spectra of crystalline and matrix isolated pyridine and pyridine-d5. The *Journal of Chemical Physics.* **1969,** *51* (9), 3762-&.

5. Podsiadło, M.; Jakobek, K.; Katrusiak, A., Density, freezing and molecular aggregation in pyridazine, pyridine and benzene. *CrystEngComm* **2010,** *12* (9), 2561-2567.

6. Heyns, A. M.; Venter, M. W., Effect of pressure on the Raman spectra of solids. 2. Pyridine. *The Journal of Physical Chemistry* **1985,** *89* (21), 4546-4549.

7. Fanetti, S.; Citroni, M.; Bini, R., Structure and reactivity of pyridine crystal under pressure. The *Journal of Chemical Physics.* **2011,** *134* (20), 204504/1-204504/9.

8. Zhuravlev, K. K.; Traikov, K.; Dong, Z.; Xie, S.; Song, Y.; Liu, Z., Raman and infrared spectroscopy of pyridine under high pressure. *Physical Review B: Condensed Matter and Materials Physics* **2010,** *82* (6), 064116/1-064116/8.

9. Merrill, L.; Bassett, W. A., Miniature diamond anvil pressure cell for single crystal x-ray diffraction studies. *Review of Scientific Instruments* **1974,** *45* (2), 290-294.

10. Forman, R. A.; Piermarini, G. J.; Barnett, J. D.; Block, S., Pressure Measurement Made by the Utilization of Ruby Sharp-Line Luminescence. *Science* **1972,** *176* (4032), 284.

11. Parsons, S. *ECLIPSE- Program for masking high-pressure diffraction images and conversion between CCD image formats. The University of Edinburgh*, 2014.

12. Tu, M.; Wiktor, C.; Rosler, C.; Fischer, R. A., Rapid room temperature syntheses of zeolitic-imidazolate framework (ZIF) nanocrystals. *Chemical Communications* **2014,** *50* (87), 13258-13260.

13. *SADABS, Bruker, Bruker AXS Inc., Madison, Wisconsin, USA*, 2014/15.

14. Sheldrick, G., SHELXT - Integrated space-group and crystal-structure determination. *Acta Crystallographica Section A* **2015,** *71* (1), 3-8.

15. Sheldrick, G., Crystal structure refinement with SHELXL. *Acta Crystallographica Section C* **2015,** *71* (1), 3-8.

16. Dolomanov, O. V.; Bourhis, L. J.; Gildea, R. J.; Howard, J. A. K.; Puschmann, H., OLEX2: a complete structure solution, refinement and analysis program. *Journal of Applied Crystallography* **2009,** *42* (2), 339-341.

17. Flack, H. D., On enantiomorph-polarity estimation. *Acta Crystallographica* **1983,** *A39*, 876-81.

18. Bruno, I. J.; Cole, J. C.; Kessler, M.; Luo, J.; Motherwell, W. D. S.; Purkis, L. H.; Smith, B. R.; Taylor, R.; Cooper, R. I.; Harris, S. E.; Orpen, A. G., Retrieval of Crystallographically-Derived Molecular Geometry Information. *Journal of Chemical Information and Computer Sciences* **2004,** *44* (6), 2133-2144.

19. Macrae, C. F.; Bruno, I. J.; Chisholm, J. A.; Edgington, P. R.; McCabe, P.; Pidcock, E.; Rodriguez-Monge, L.; Taylor, R.; van de Streek, J.; Wood, P. A., Mercury CSD 2.0 - new features for the visualization and investigation of crystal structures. *Journal of Applied Crystallography* **2008,** *41* (2), 466-470.

20. Bradenburg, K. *DIAMOND.* , Crystal Impact GbR, Bonn, Germany: 1999.

21. Sheldrick, G. M. *SHELXTL-XP version 6.01*, University of Göttingen, Germany and Bruker-AXS: Göttingen, Germany and Madison, Wisconsin, USA, 2001.

22. Besson, J. M.; Nelmes, R. J., New developments in neutron-scattering methods under high pressure with the Paris-Edinburgh cells. *Physica B: Condensed Matter* **1995,** *213&214* (1-4), 31-6.

23. Besson, J. M.; Nelmes, R. J.; Halem, G.; Loveday, J. S.; Weill, G.; Hull, S., Neutron powder diffraction above 10 GPa. *Physica B: Condensed Matter* **1992,** *180-181* (Pt. B), 907-10.

24. Bull, C. L.; Funnell, N. P.; Tucker, M. G.; Hull, S.; Francis, D. J.; Marshall, W. G., PEARL: the high pressure neutron powder diffractometer at ISIS. *High Pressure Research* **2016,** *36* (4), 493-511.

25. Coelho, A., TOPAS and TOPAS-Academic: an optimization program integrating computer algebra and crystallographic objects written in C++. *Journal of Applied Crystallography* **2018,** *51* (1), 210-218.

26. Frisch, M. J.; Trucks, G. W.; Schlegel, H. B.; Scuseria, G. E.; Robb, M. A.; Cheeseman, J. R.; Scalmani, G.; Barone, V.; Petersson, G. A.; Nakatsuji, H.; Li, X.; Caricato, M.; Marenich, A.; Bloino, J.; Janesko, B. G.; Gomperts, R.; Mennucci, B.; Hratchian, H. P.; Ortiz, J. V.; Izmaylov, A. F.; Sonnenberg, J. L.; Williams-Young, D.; Ding, F.; Lipparini, F.; Egidi, F.; Goings, J.; Peng, B.; Petrone, A.; Henderson, T.; Ranasinghe, D.; Zakrzewski, V. G.; Gao, J.; Rega, N.; Zheng, G.; Liang, W.; Hada, M.; Ehara, M.; Toyota, K.; Fukuda, R.; Hasegawa, J.; Ishida, M.; Nakajima, T.; Honda, Y.; Kitao, O.; Nakai, H.; Vreven, T.; Throssell, K.; Jr., J. A. M.; Peralta, J. E.; Ogliaro, F.; Bearpark, M.; Heyd, J. J.; Brothers, E.; Kudin, K. N.; Staroverov, V. N.; Keith, T.; Kobayashi, R.; Normand, J.; Raghavachari, K.; Rendell, A.; Burant, J. C.; Iyengar, S. S.; Tomasi, J.; Cossi, M.; Millam, J. M.; Klene, M.; Adamo, C.; Cammi, R.; Ochterski, J. W.; Martin, R. L.; Morokuma, K.; Farkas, O.; Foresman, J. B.; Fox, D. J. *Gaussian 09, Revision E.01.*, Gaussian, Inc.: Wallingford CT, 2016.

27. Gavezzotti, A., Calculation of lattice energies of organic crystals: The PIXEL integration method in comparison with more traditional methods. *Zeitschrift für Kristallographie* **2005,** *220*, 499-510.

28. Gavezzotti, A., *Molecular Aggregation - Structure Analysis and Molecular Simulation of Crystals and Liquids*. lst ed.; Oxford University Press: New York, 2007; p 425.

29. Gavezzotti, A., Efficient computer modeling of organic materials. The atom–atom, Coulomb–London–Pauli (AA-CLP) model for intermolecular electrostatic-polarization, dispersion and repulsion energies. *New Journal of Chemistry* **2011,** *35* (7), 1360-1368.

30. Hohenstein, E. G.; Sherrill, C. D., Density fitting of intramonomer correlation effects in symmetry-adapted perturbation theory. *The Journal of Chemical Physics* **2010,** *133* (1), 014101.

31. Hohenstein, E. G.; Sherrill, C. D., Efficient evaluation of triple excitations in symmetry-adapted perturbation theory via second-order Moller–Plesset perturbation theory natural orbitals. *The Journal of Chemical Physics* **2010,** *133* (10), 104107.

32. Gonze, X.; Charlier, J. C.; Allan, D. C.; Teter, M. P., Interatomic force constants from first principles: The case of alpha-quartz. *Physical Review B* **1994,** *50* (17), 13035-13038.

33. Clark, S. J.; Segall, M. D.; Pickard, C. J.; Hasnip, P. J.; Probert, M. J.; Refson, K.; Payne, M. C., First principles methods using CASTEP. *Zeitschrift für Kristallographie* **2005,** *220* (5-6), 567-570.

34. *Dassault Systèmes, BIOVIA, Materials Studio, San Diego, CA, USA*. **2017**.

35. Perdew, J. P.; Burke, K.; Ernzerhof, M., Generalized Gradient Approximation Made Simple. *Physical Review Letters* **1996,** *77* (18), 3865-3868.

36. Monkhorst, H. J.; Pack, J. D., Special points for Brillouin-zone integrations. *Physical Review B* **1976,** *13* (12), 5188-5192.

37. Tkatchenko, A.; Scheffler, M., Accurate Molecular Van Der Waals Interactions from Ground-State Electron Density and Free-Atom Reference Data. *Physical Review Letters* **2009,** *102* (7), 073005.

38. Refson, K.; Tulip, P. R.; Clark, S. J., Variational density-functional perturbation theory for dielectrics and lattice dynamics. *Physical Review B* **2006,** *73*, 155114.

39. Dunitz, J. D.; Schweizer, W. B., Molecular Pair Analysis: C–H···F Interactions in the Crystal Structure of Fluorobenzene? And Related Matters. *Chemistry - A European Journal* **2006,** *12* (26), 6804-6815.

40. Dunitz, J. D.; Schweizer, W. B., Alloxan: Is it really a problem structure? *CrystEngComm* **2007,** *9* (4), 266-269.

41. Thiery, M. M.; Leger, J. M., High-Pressure Solid-Phases of Benzene .1. Raman and X-Ray Studies of C_6H_6 at 294 K up to 25 GPa. The *Journal of Chemical Physics.* **1988,** *89* (7), 4255-4271.

42. van Eijck, B. P.; Spek, A. L.; Mooij, W. T. M.; Kroon, J., Hypothetical crystal structures of benzene at 0 and 30 kbar. *Acta Crystallographica Section B-Structural Science* **1998,** *54*, 291-299.

43. Wen, X.-D.; Hoffmann, R.; Ashcroft, N. W., Benzene under High Pressure: a Story of Molecular Crystals Transforming to Saturated Networks, with a Possible Intermediate Metallic Phase. *Journal of the American Chemical Society* **2011,** *133* (23), 9023-9035.

44. Aina, A. A.; Misquitta, A. J.; Price, S. L., From dimers to the solid-state: Distributed intermolecular force-fields for pyridine. The *Journal of Chemical Physics* **2017,** *147* (16).

45. Anghel, A. T.; Day, G. M.; Price, S. L., A study of the known and hypothetical crystal structures of pyridine: why are there four molecules in the asymmetric unit cell? *CrystEngComm* **2002,** *4*, 348-355.

46. Gavezzotti, A., Towards a realistic model for the quantitative evaluation of intermolecular potentials and for the rationalization of organic crystal structures. Part II. Crystal energy landscapes. *CrystEngComm* **2003,** *5*, 439-446.

47. van de Streek, J.; Neumann, M. A., Crystal-structure prediction of pyridine with four independent molecules. *CrystEngComm* **2011,** *13* (23), 7135-7142.

48. Casati, N.; Kleppe, A.; Jephcoat, A. P.; Macchi, P., Putting pressure on aromaticity along with in situ experimental electron density of a molecular crystal. *Nature Communications.* **2016,** *7,* 8.

49. Blatov, V. A.; Shevchenko, A. P.; Proserpio, D. M., Applied Topological Analysis of Crystal Structures with the Program Package ToposPro. *Crystal Growth & Design* **2014,** *14* (7), 3576-3586.

50. Peresypkina, E. V.; Blatov, V. A., Topology of molecular packings in organic crystals. *Acta Crystallographica Section B-Structural Science Crystal Engineering and Materials* **2000,** *56*, 1035-1045.

51. O'Keeffe, M.; Peskov, M. A.; Ramsden, S. J.; Yaghi, O. M., The Reticular Chemistry Structure Resource (RCSR) Database of, and Symbols for, Crystal Nets. *Accounts of Chemical Research* **2008,** *41* (12), 1782-1789.

52. Angel Ross, J.; Alvaro, M.; Gonzalez-Platas, J., EosFit7c and a Fortran module (library) for equation of state calculations. In *Zeitschrift für Kristallographie - Crystalline Materials*, 2014; Vol. 229, p 405.

53. Likhacheva, A. Y.; Rashchenko, S. V.; Chanyshev, A. D.; Inerbaev, T. M.; Litasov, K. D.; Kilin, D. S., Thermal equation of state of solid naphthalene to 13 GPa and 773 K: In situ X-ray diffraction study and first principles calculations. The *Journal of Chemical Physics* **2014,** *140* (16), 8.

54. Slebodnick, C.; Zhao, J.; Angel, R.; Hanson, B. E.; Song, Y.; Liu, Z. X.; Hemley, R. J., High pressure study of Ru-3(CO)(12) by x-ray diffraction, Raman, and infrared spectroscopy. *Inorgic Chemistry.* **2004,** *43* (17), 5245-5252.

55. Harty, E. L.; Ha, A. R.; Warren, M. R.; Thompson, A. L.; Allan, D. R.; Goodwin, A. L.; Funnell, N. P., Reversible piezochromism in a molecular wine-rack. *Chemical Communications* **2015,** *51* (53), 10608-10611.

56. Funnell, N. P.; Bull, C. L.; Ridley, C. J.; Capelli, S., Structural behaviour of OP-ROY at extreme conditions. *CrystEngComm* **2019,** *21* (30), *4473-4483*.

57. Eikeland, E.; Thomsen, M. K.; Madsen, S. R.; Overgaard, J.; Spackman, M. A.; Iversen, B. B., Structural Collapse of the Hydroquinone–Formic Acid Clathrate: A Pressure-Medium-Dependent Phase Transition. *Chemistry – A European Journal* **2016,** *22* (12), 4061-4069.

58. Fortes, A. D.; Funnell, N. P.; Bull, C. L., Thermoelastic properties of deuterated melamine, C3N6D6, between 4.2-320 K at 5 kPa and between 0.1-5.0 GPa at 295 K from neutron powder diffraction and DFT calculations. *High Pressure Research* **2019,** *39* (1), 160-178.

59. Funnell, N.; Dawson, A.; Francis, D.; Lennie, A. R.; Marshall, W. G.; Moggach, S.; Warren, J.; Parsons, S., *The effect of pressure on the crystal structure of L-alanine*. *CrystEngComm*, **2010**, 12, 2573-2583

60. Funnell, N. P.; Dawson, A.; Marshall, W. G.; Parsons, S., Destabilisation of hydrogen bonding and the phase stability of aniline at high pressure. *CrystEngComm* **2013,** *15* (6), 1047-1060.

61. Mayami, A.; Keith, R.; Richard, H. F.; Peter, D. H., A first-principles study of the vibrational properties of crystalline tetracene under pressure. *Journal of Physics: Condensed Matter* **2015,** *27* (37), 375402.

62. Campbell, B. J.; Stokes, H. T.; Tanner, D. E.; Hatch, D. M., ISODISPLACE: a web-based tool for exploring structural distortions. *Journal of Applied Crystallography* **2006,** *39* (4), 607-614.

63. *H. T. Stokes, D. M. Hatch, and B. J. Campbell, ISODISTORT, ISOTROPY Software Suite, iso.byu.edu.*

64. Groom, C. R.; Bruno, I. J.; Lightfoot, M. P.; Ward, S. C., The Cambridge Structural Database. *Acta Crystallographica Section B* **2016,** *72* (2), 171-179.

65. Steed, K. M.; Steed, J. W., Packing Problems: High Z' Crystal Structures and Their Relationship to Cocrystals, Inclusion Compounds, and Polymorphism. *Chemical Reviews* **2015,** *115* (8), 2895-2933.

66. Anderson, K. M.; Probert, M. R.; Goeta, A. E.; Steed, J. W., Size does matter-the contribution of molecular volume, shape and flexibility to the formation of co-crystals and structures with Z ' > 1. *CrystEngComm* **2011,** *13* (1), 83-87.

67. Gavezzotti, A., Structure and energy in organic crystals with two molecules in the asymmetric unit: causality or chance? *CrystEngComm* **2008,** *10* (4), 389-398.

68. Johnstone, R. D. L.; M. Ieva; A.R. Lennie; H. McNab; E. Pidcock; Warren, J.; Parsons, S., Pressure as a tool in crystal engineering: inducing a phase transition in a high-Z' structure. *CrystEngComm* **2010,** 12(9), 2520-2523).

69. Ridout, J.; Probert, M. R., Low-temperature and high-pressure polymorphs of isopropyl alcohol. *CrystEngComm* **2014,** *16* (32), 7397-7400.

70. Chanyshev, A. D.; Litasov, K. D.; Rashchenko, S. V.; Sano-Furukawa, A.; Kagi, H.; Hattori, T.; Shatskiy, A. F.; Dymshits, A. M.; Sharygin, I. S.; Higo, Y., High-Pressure-High-Temperature Study of Benzene: Refined Crystal Structure and New Phase Diagram up to 8 GPa and 923 K. *Crystal Growth & Design* **2018,** *18* (5), 3016-3026.

71. Cansell, F.; Fabre, D.; Petitet, J. P., Phase Transitions and Chemical-Transformations of Benzene up to 550 °C and 30 GPa. The *Journal of Chemical Physics* **1993,** *99* (10), 7300-7304.

Chapter 5

Pressure-Induced Porosity in Molecular Solids: Inclusion of Neon in Cu_2 Pacman at 4.7 GPa

5.1. Introduction

Schiff-base calixpyrrole or porphyrin type ligands can organise two metals to be proximate within a cleft which is also capable of accommodating small molecules. This arrangement has led to these systems being described as Pacman complexes.[1-3] The Schiff-base calixpyrrole (L) type Pacman complexes [M_2(L)] are characterised by two metals (M) centred in distorted square planar N_4-pyrrole-imine donor environments. The MN_4 environments, the macrocycle pockets, are hinged by two phenyl groups to give the wedge-shaped Pacman geometry (**Figure 5.1**). The Pacman cleft can be tuned to some extent by ligand modification so that the cleft opens. For example, in [Cu_2(L)], replacing the phenyl hinge group with larger anthracene units; and substituting methyl groups on the *meso*-carbon with bulky pentafluorophenyl groups results in a larger cleavage with increased metal separation distances.[3]

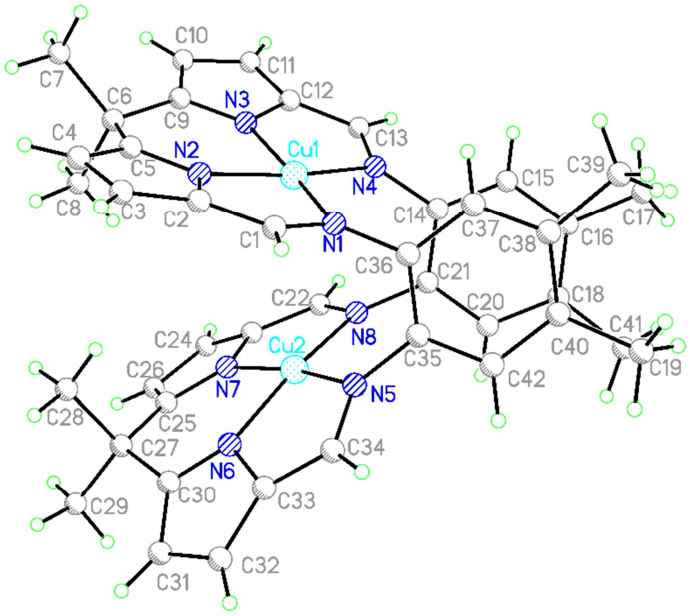

Figure 5.1 The Cu-Pacman molecule at ambient conditions and the numbering scheme used.

The Pacman complexes have been shown to catalyse various reactions of small molecules. The highly controlled arrangement of small molecules contained in the cleft leads to changes in redox activity of the metals, as in the double-pillared cobalt Pacman complex that has been shown to catalyse the 4-electron reduction of dioxygen to water;[1] and recently, Pankhurst *et. al* have used a dinuclear Cu^{II} pyrrolic Schiff-base macrocycle activated with ferric chloride as a cooperative catalyst for the oxygenation of π-activated benzylic substrates.[3] The Pacman complexes represent possible alternatives to conventional and expensive precious-metal-based catalysts; or even as less harmful alternatives to toxic catalytic species such as chromium or manganese.

The catalytic properties of the Pacman complexes make them ideal systems of study in the search for new sustainable processes for activation of small molecules. We are interested in mediating small molecule uptake in a solid Pacman complex by high-pressure, a technique that has already been shown to induce guest-uptake in various porous materials like the metal-organic-frameworks (MOF),[5] but also in seemingly nonporous solids, for example helium inclusion occurs at pressures above 3 GPa in the nonporous molecular solid, arsenolite.[6]

The Pacman geometry and conformation are quite flexible, and potentially susceptible to modification by variation of externally applied conditions. To date, only one of the Pacman complexes, a Schiff-base calixpyrrole type, augmented with two chromium (II) metal centres, $[Cr_2(L)]$, has been investigated at high-pressure.[4] Pressure induces slippage of the $Cr–N_4$ macrocycle pockets but it has no appreciable effect on the metal-metal distance or bite angle; at least to the modest pressure of 3 GPa.

3 GPa is a relatively modest pressure in the context of modern extreme conditions research, and in this chapter, we aim to investigate the effect of higher pressures, which may ultimately provide a strategy, for example to control activity about the metal centres. The dinuclear Cu^{II} pyrrolic Schiff-base

analogue ([Cu_2(L)]) has already been shown to be catalytically active and was therefore chosen as the complex of interest in this compression study. Neon was chosen as a probe molecule for studying guest-uptake not only because of its inertness and small size but also because it is an excellent pressure transmitting medium (PTM) providing hydrostatic conditions to 15 GPa.[7] We go on to show that neon is a penetrating medium and a neon-Pacman co-crystal forms at *ca.* 5 GPa. Pressure mediated neon inclusion has already very recently been shown to occur in molecular ammonium metal formates,[8] and the MOFs: PCN-220 and NiMOF-74.[9]

5.2. Experimental

5.2.1. Recrystallisation of Dicopper Pacman

The dicopper Pacman complex was synthesised by reported procedures and obtained from the Love group at the University of Edinburgh.[2] Single crystals of dicopper pacman were then recrystallised by slow evaporation in dichloromethane to give large black, rod shaped crystals.

5.2.2. Ambient Pressure Single Crystal X-ray Diffraction

A single crystal measuring 50 x 50 x 100 μm³ was cut from a larger crystal. Single-crystal diffraction data were collected at ambient pressure and at room temperature and 100 K using synchrotron radiation (E = 16.5 keV) on Beamline 11.3.1 at the Advanced Light Source.[10]

5.2.3. High Pressure Single Crystal X-ray Diffraction

An irregular block shaped crystal was cut from the bulk sample measuring *ca.* 70 x 80 x 90 μm³ and loaded into a BX90 type diamond anvil cell (DAC)

along with a ruby sphere for pressure determination. The cell was constructed using Boehler-Almax diamonds with a 500 μm culet set in tungsten-carbide backing seats. The gasket material forming the sample chamber was rhenium; its initial diameter was 320 μm and its initial thickness was *ca.* 110 μm. The cell was then gas loaded with neon gas as a hydrostatic medium.

High-pressure single crystal diffraction data were collected on compression of the sample in steps of *ca.* 0.8 GPa from 1.30 to 8.13 GPa using synchrotron radiation (E = 25 keV) on Beamline 12.2.2 at the Advanced Light Source.[11] Pressure measurements were performed by the ruby fluorescence method.[12]

Decompression of the sample resulted in degradation of the single crystal into multiple domains, and no discernible diffraction data could be obtained.

5.2.4. Structure Solutions and Refinements

All diffraction data were processed using the Bruker suite of programs.[13] Data reduction was performed by SAINT[14] and dynamic masks generated by ECLIPSE[15] were used to mask shaded detector regions from the cell body in the high-pressure data sets. Absorption and systematic error corrections were applied using SADABS[16] and space group determinations by analysis of systematic absences were performed using XPREP.[17] The ambient pressure-temperature and low temperature structures were solved by direct methods (SHELXT)[18] and all data refined against $|F|^2$ using SHELXL[19] as part of the OLEX2 graphical user interface.[20]

The 3D coordinates of the ambient pressure-temperature structure were used as a starting model in the first high-pressure structure refinement; all subsequent structures were then modelled using the coordinates of the preceding pressure structure. Non-hydrogen and non-metal bond distances in the high-pressure structures were restrained to be similar to those of the

ambient temperature and pressure structure. Methyl hydrogen atoms were located in 'circular' difference syntheses carried out about the locus of their possible positions; the orientation of the group was allowed to refine while holding the CH distances and HCH angles fixed to ideal values. Other hydrogen atoms were placed in ideal positions and treated with a riding model.

All non-hydrogen atoms in the ambient pressure structures were refined with anisotropic displacement parameters. Only copper atoms were refined anisotropically in the high-pressure structures to reduce the number of refined parameters and improve the low data to parameter ratio. For the structures at 4.67 GPa and above a non-standard unit cell setting is used (with $\beta < 90°$) to facilitate structural comparisons with the structures determined at lower pressure. Full crystallographic details are given in **Table 5.1.**

5.2.5. Calculation of Molecular Volumes

The molecular volumes of the pacman complexes were calculated via void volumes obtained using MERCURY.[21] Neon atoms were removed prior to calculations in the neon-containing co-crystal structures. The calculations employed the contact surface algorithm which maps the entire void surface regardless of probe accessibility. The probe radius was 0.2 Å with a grid spacing of 0.1 Å (the minimum values allowed by the program). A chemically meaningful probe radius of 1.2 Å, representative of the radius of a molecule of H_2, was also tested but resulted in zero accessible volume. The interstitial void volumes reported here are not solvent accessible. The void volumes enable the molecular volumes of the pacman complex to be calculated according to [total unit cell volume – void volume]/*Z*. Void and molecular volumes are given in **Table 5.2.**

5.2.6. Other Programs Used

PIXEL packing energy calculations were carried out using CLP-PIXEL.[22-23] Molecular electron densities were calculated using GAUSSIAN09[24] with the B3LYP/6-31G** level of theory and basis set. CH distances were reset to 1.083 Å prior to the electron density calculations. The electron density was calculated in steps of 0.08 Å, with a condensation level of 5 used for the energy calculations. Equations-of-state (EOS) were determined using EOSFit-7,[25] and strain tensor calculations were performed using the program STRAIN.[26-27] Geometries were measured using DIAMOND[28] and PLATON.[29]

Table 5.1 Experimental details. All structures are monoclinic, C2/c with Z = 8. H-atom parameters were constrained. Measurements at 2.01 and 2.52 GPa contain unit cell information only. Detector saturation problems degraded the quality of the intensity measurements in these cases. T = 298 K unless otherwise specified. λ = 0.7749 and 0.4959 Å for the ambient and high-pressure collections, respectively.

Pressure (GPa)	**0.00**	**0.00 (*T* = 100 K)**	**1.30**	**2.01**	**2.52**	**3.46**
Chemical formula	$C_{42}H_{40}Cu_2N_8$	$C_{42}H_{40}Cu_2N_8$	$C_{42}H_{40}Cu_2N_8$	$C_{42}H_{40}Cu_2N_8$	$C_{42}H_{40}Cu_2N_8$	$C_{42}H_{40}Cu_2N_8$
M_r	783.90	783.90	783.90	783.90	783.90	783.90
a, *b*, *c* (Å)	25.3657 (15), 9.9388 (6), 29.1779 (17)	25.1863 (18), 9.9249 (7), 28.570 (2)	24.808 (6), 9.6971 (12), 27.648 (3)	24.557 (3), 9.5814 (8), 27.013 (2)	24.4289 (17), 9.5291 (4), 26.7021 (10)	24.281 (3), 9.4519 (6), 26.2355 (15)
β (°)	92.788 (2)	91.745 (3)	92.073 (4)	91.877 (2)	91.748 (1)	91.553 (2)
V (Å^3)	7347.2 (8)	7138.5 (9)	6646.7 (19)	6352.4 (11)	6213.0 (6)	6018.8 (8)
μ (mm^{-1})	1.51	1.55	0.50	0.53	1.78	0.56
Crystal size (mm)	0.10 × 0.05 × 0.05	0.1 × 0.05 × 0.05	0.09 × 0.08 × 0.07	0.09 × 0.08 × 0.07	0.09 × 0.08 × 0.07	0.09 × 0.08 × 0.07
T_{min}, T_{max}	0.643, 0.746	0.644, 0.747	0.430, 0.744	0.6454, 0.7438	0.585, 0.744	0.619, 0.744
No. of measured, independent and observed [$I > 2\sigma(I)$] reflections	37975, 6712, 5654	64755, 14237, 11627	10411, 2283, 1617	7264, 1396, 1214	11548, 2468, 1896	12029, 2374, 2067
R_{int}	0.104	0.090	0.171	0.042	0.046	0.041
$(\sin\theta/\lambda)_{max}$ (Å^{-1})	0.603	0.781	0.588	0.500	0.625	0.625
$R[F^2 > 2\sigma(F^2)]$, $wR(F^2)$, *S*	0.076, 0.195, 1.03	0.054, 0.148, 1.05	0.099, 0.283, 1.04	N/A	N/A	0.048, 0.134, 1.10
No. of parameters	478	478	227	N/A	N/A	228
No. of restraints	0	0	52	N/A	N/A	52
$\Delta\rho_{max}$, $\Delta\rho_{min}$ (e Å^{-3})	0.77, -0.65	0.92, -0.76	0.52, -0.71	N/A	N/A	0.67, -0.44

Table 5.1 Experimental details continued

Pressure (GPa)	**3.46**	**4.67**	**5.17**	**5.81**	**6.90**	**8.13**
Chemical formula	$C_{42}H_{40}Cu_2N_8$	$C_{42}H_{40}Cu_2N_8{\cdot}Ne_{3.5}$	$C_{42}H_{40}Cu_2N_8{\cdot}Ne_{3.5}$	$C_{42}H_{40}Cu_2N_8{\cdot}Ne_{3.5}$	$C_{42}H_{40}Cu_2N_8{\cdot}Ne_{3.5}$	$C_{42}H_{40}Cu_2N_8{\cdot}Ne_{3.5}$
M_r	783.90	854.53	854.53	854.53	854.53	854.53
a, *b*, *c* (Å)	24.281 (3), 9.4519 (6), 26.2355 (15)	24.259 (6), 9.2882 (15), 26.841 (4)	24.215 (6), 9.2391 (16), 26.599 (5)	24.115 (4), 9.2099 (11), 26.461 (3)	23.997 (3), 9.1398 (8), 26.1160 (18)	23.811 (7), 9.0709 (19), 25.766 (5)
β (°)	91.553 (2)	84.039 (8)	84.042 (8)	83.888 (7)	83.750 (5)	83.532 (7)
V (Å^3)	6018.8 (8)	6015 (2)	5919 (2)	5843.5 (13)	5693.8 (9)	5530 (2)
μ (mm^{-1})	0.56	0.57	0.58	0.59	0.60	0.62
Crystal size (mm)	0.09 × 0.08 × 0.07	0.09 × 0.08 × 0.07	0.09 × 0.08 × 0.07	0.09 × 0.08 × 0.07	0.09 × 0.08 × 0.07	0.09 × 0.08 × 0.07
T_{min}, T_{max}	0.619, 0.744	0.463, 0.744	0.227, 0.744	0.647, 0.744	0.595, 0.744	0.187, 0.744
No. of measured, independent and observed [$I > 2\sigma(I)$] reflections	12029, 2374, 2067	7250, 1840, 1294	10068, 2208, 1477	11494, 2463, 1778	11829, 2325, 1623	10611, 2272, 1285
R_{int}	0.041	0.118	0.072	0.105	0.093	0.104
$(\sin\theta/\lambda)_{max}$ (Å^{-1})	0.625	0.588	0.625	0.625	0.625	0.625
$R[F^2 > 2\sigma(F^2)]$, $wR(F^2)$, *S*	0.048, 0.134, 1.10	0.080, 0.191, 1.09	0.050, 0.117, 0.95	0.070, 0.189, 0.98	0.079, 0.211, 0.96	0.065, 0.162, 0.92
No. of parameters	228	241	240	240	240	240
No. of restraints	52	52	52	52	52	52
$\Delta\rho_{max}$, $\Delta\rho_{min}$ (e Å^{-3})	0.67, -0.44	0.48, -0.49	0.43, -0.38	0.58, -0.75	0.77, -0.76	0.46, -0.38

Table 5.2 Molecular volumes, unit cell volumes and their respective void contents, of Cu-Pacman complexes at different pressures.

Complex	Pressure (GPa)	V_{cell} (Å³)	V_{void} (Å³)	% Void	V_{mol}	Temperature (K)
[Cu2(L)]	**0.00**	7138.5(9)	2171.55	30.4	620.85	100
	0.00	7347.2(8)	2412.46	32.8	616.84	298
	1.30	6646.7(19)	1665.61	25.1	622.65	298
	3.46	6018.8(8)	1068.7	17.8	618.65	298
[Cu2(L)]·$Ne_{3.5}$	**4.67**	6015(2)	1127.51	18.7	610.96	298
	5.17	5919(2)	1053.94	17.8	608.96	298
	5.81	5843.5(13)	998.13	17.1	605.67	298
	6.90	5693.8(9)	886.76	15.6	600.90	298
	8.13	5530(2)	771.24	13.9	594.81	298

5.3. Results and Discussion

5.3.1. Compression of [Cu_2(L)] in Neon

The crystal structure of [Cu_2(L)] at ambient pressure and 298 K contains layers of molecules oriented with their longest inertial axes perpendicular to the layer. Within the layer each molecule is surrounded by six others (see **Figure 5.2(a)**) with centroid···centroid distances in the range 8.7 to 9.9 Å and energies, calculated by the PIXEL method, to be between –56.6 and –26.5 kJ mol^{-1}. The interactions, which are dominated by dispersion, take the form of stacking and other contacts between the macrocyclic parts of the ligands. The strongest of these (labelled A in **Figure 5.2(a)**) involves two inversion-related moieties based on Cu2 and the pyrrole rings containing N6 and N7 where the interplanar spacing is 3.60(2) Å. The methyl groups are positioned on the top and bottom surfaces of the layers, which are stacked along the *a*-direction (**Figure 5.2 (b)**). Three contacts are formed to the layers above and below with centroid···centroid distances between 13.6 and 14.9 Å and energies between –21.0 and –1.0 kJ mol^{-1}. The overall coordination number of each molecule is thus 12, and the structure has an approximately underlying hexagonal close packed topology.

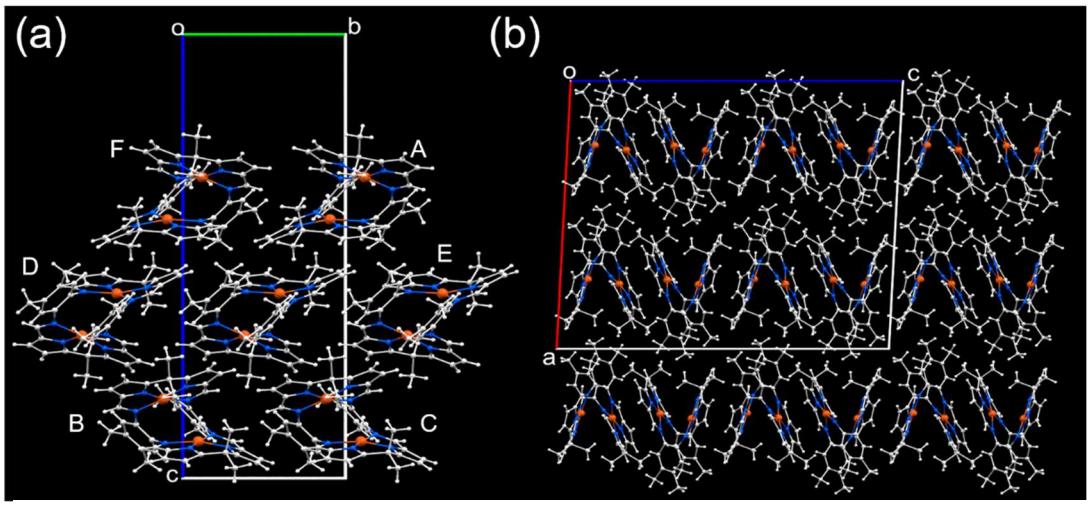

Figure 5.2 (a) layering formed in the *bc*-plane as viewed down the longest inertial axes of the molecules. The six strongest molecular contacts surrounding the central reference molecule are labelled A–F and **(b)** layered stacking along **a**.

The maximum pressure reached in this study was 8.13 GPa, which is much higher than had been achieved in the previous study on the related chromium system. The unit cell parameters and the molecular volume of the pacman complex are plotted as a function of pressure in **Figures 5.3 (a)** and **(b)**. There are two distinct compression regimes, the first from ambient pressure to 3.46 GPa, and the second from 3.46 to 8.13 GPa.

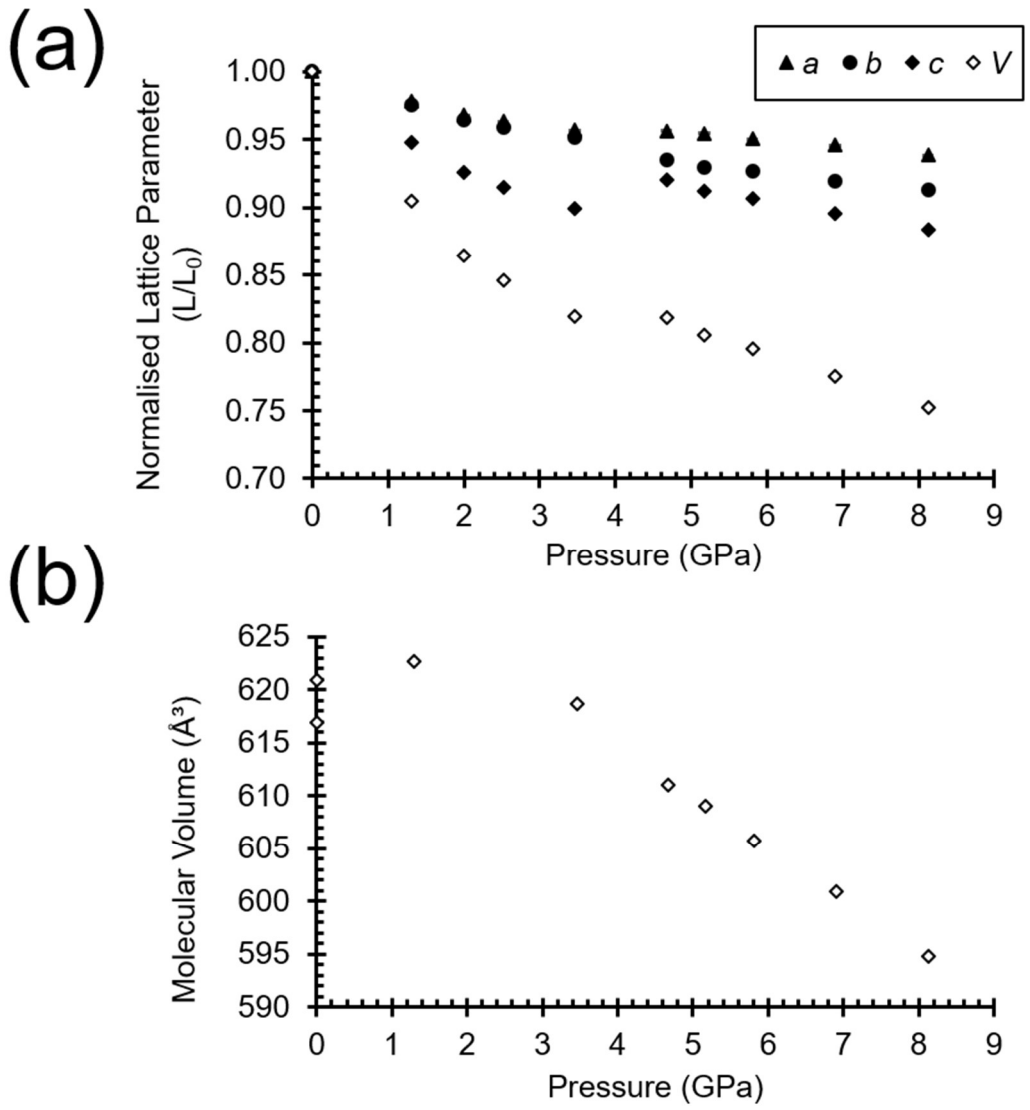

Figure 5.3 (a) normalised lattice parameters and **(b)** molecular volume as a function of pressure.

Up to 3.46 GPa the *a* and *b*-axes reduce by similar amounts, (4.3 and 4.9 %), while the largest compression (10.1%) occurs in the *c*-axis. The principal directions of the strain tensor[27] also align quite closely with the unit cell axes, with the largest (X_1) making an angle of 8.4° with **c** and the smallest (X_3) making an angle of 11.2° with **a**. The middle value (X_2) lies exactly along **b** by symmetry. These data indicate that the macrocycle contacts within the layers are more compressible than the methyl-methyl contacts between the layers, even though they are stronger. For example, the stacking interaction described above shortens almost 0.5 Å from 3.60(2) Å at ambient pressure to 3.12(3) Å at 3.46 GPa.

The compressibility of these interactions can be contrasted with the behaviour of hydrogen bonds, which have similar energies but are much less compressible. For example, an OH···O hydrogen bond in L-threonine (interaction energy –60 kJ mol^{-1} at ambient pressure) shortens from 1.87 to 1.77 Å between 0 and 4.0 GPa.[30] Halogen bonds are also less compressible, and the CN···I halogen bond in 4-iodobenzonitrile (interaction energy –11 kJ mol^{-1} at ambient pressure) shortens from 3.168(4) to 2.895(8) Å between 0 and 3.9 GPa.[31] The bulk modulus, obtained using the third order Birch-Murnaghan equation-of-state is 8.4(11) GPa [K' = 7.4(19)]. The low value of K_0 is characteristic of compressible molecular systems dominated by dispersion interactions, *e.g.* naphthalene (K_0=8.4 GPa),[32] and aniline-II (K_0=5.4 GPa);[33] hydrogen-bonded solids have higher values, *e.g.* 15.23(8) GPa for L-threonine.[30]

Above 3.46 GPa neon becomes intercalated into the structure, giving a co-crystal of stoichiometry $[Cu_2(L)]\cdot Ne_{3.5}$. The incorporation of neon leads to an increase in the physical size of the crystal (**Figure 5.4**) and causes a discontinuity in the cell dimensions and volume (see **Table 5.2** and **Figure 5.3(a)**). The rates of compression in the *a* and *b*-axes begin to diverge, while there is a 2.0 % *increase* in the length of the *c*-axis. The space group remains

unchanged. Beyond 4.67 GPa, the unit cell volume decreases monotonically, indicating that no more neon is incorporated into the structure.

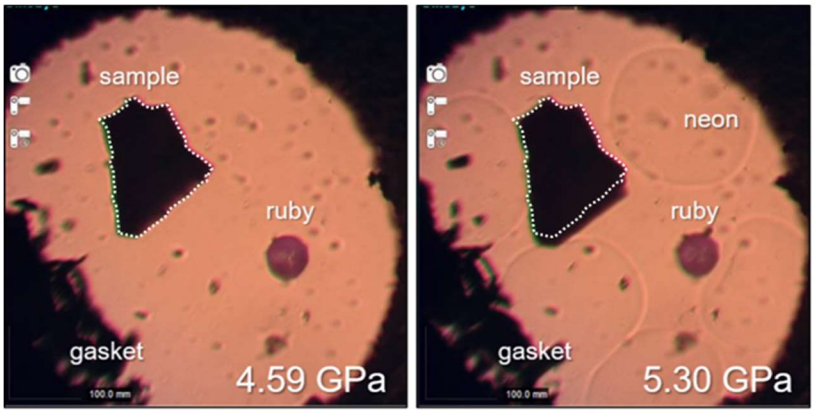

Figure 5.4 The contents of the DAC before and after neon freezing. The outline of the crystal prior to neon freezing (white dashed line) is superimposed on the post neon freezing image to highlight the change in crystal size and shape.

5.3.2. The Crystal Structure of $[Cu_2L]\cdot Ne_{3.5}$

The four new neon sites are located on three general positions (Ne2-4) and one inversion centre (Ne1). Ne1, 2 and 4 reside between the layers described above, forming contacts with methyl groups (**Figure 5.5**). At 4.67 GPa Ne···C distances span the range 2.70 (Ne4···C40) – 3.18 Å (Ne4···C10), which imply Ne···H distances of between 2.27 and 2.71 Å. The Ne···C distances shorten to 2.65 – 3.03 Å at 8.13 GPa.

Ne3 is located within the layers. At 4.67 GPa it is adjacent to the cleft of the pacman ligand, which flexes in response (**Figure 5.6(a) and (b)**). The shortest Ne···N contact is made to N3 (3.03 Å at 4.67 GPa and 2.92 Å at 8.13 GPa), while the shortest Ne3···C contacts are between 2.76 Å (C24) and 2.85 Å (C22) (**Figure 5.6(c)**). These shorten to 2.68 and 2.75 Å at 8.13 GPa.

The neon positions persist on compression between 4.67 and 8.13 GPa, bridging angles and methyl-neon angles changing by only a few degrees. Animations showing the path of compression are available in the electronic supplementary information.

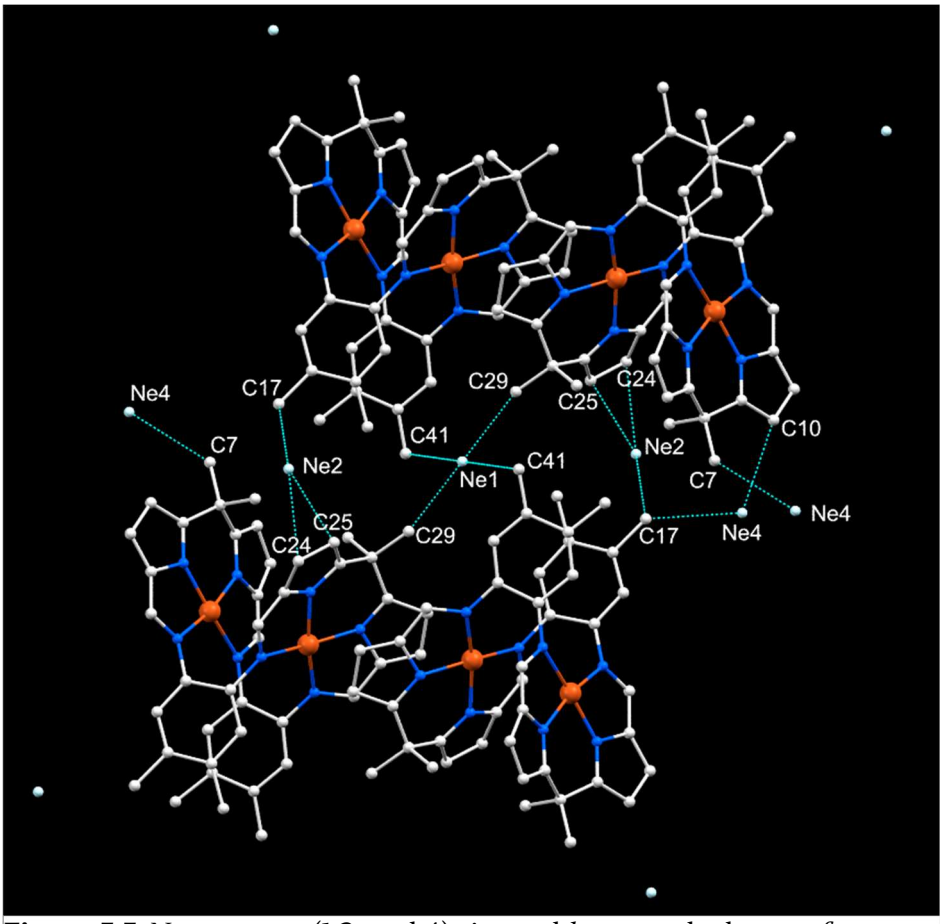

Figure 5.5 Neon atoms (1,2, and 4) situated *between* the layers of pacman molecules at 4.67 GPa. Hydrogen atoms are omitted for clarity.

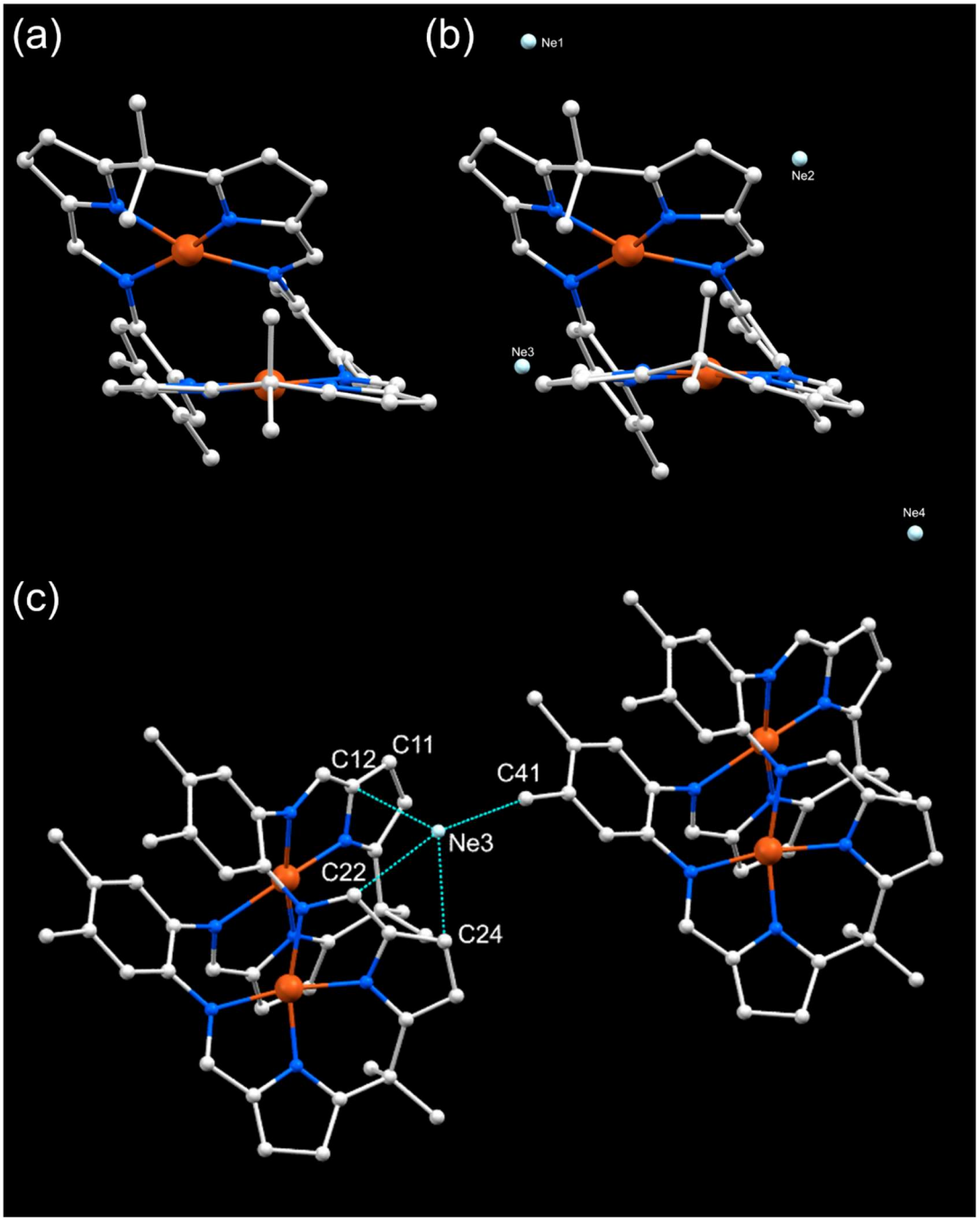

Figure 5.6 (a) view of the pacman complex before the phase transition at 3.46 GPa and **(b)** just after the transition at 4.67 GPa showing flexing of the Pacman ligand. Inset **(c)** shows the Ne3···C shortest contacts (less than 3 Å) *within* the macrocyclic layers at 4.67 GPa. Hydrogen atoms are omitted for clarity.

5.3.3. The Mechanism of Neon Uptake

Pressure-driven incorporation of hydrostatic media has been observed in metal-organic frameworks[5] such as in ZIF-8, UiO-67 and UiO-abdc [abdc=4,4'azobenzene dicarboxylate].[34-35] In the case of [Cu_2L] the mechanism of neon incorporation is less obvious. The crystal structure of [Cu_2L] at ambient pressure consists of approximately 30 % empty interstitial void space. This figure is typical of non-porous molecular solids. None of this volume is solvent-accessible and inspection of Fourier difference maps indicates that it contains no electron density at ambient pressure and 100 K. At 3.46 GPa the proportion of void space reduces to 18 %.

Figure 5.3(b) shows that between ambient pressure and 3.46 GPa the molecular volume of the pacman complex is relatively constant but following the transition it begins to drop steadily with pressure. The necessary space for neon uptake is thus created by the internal conformational flexibility of the complex. The conformational change is illustrated in **Figures** 5.**6(a)** and **(b)**, and an animation is available in the ESI.

Conformational changes in Schiff-base calixpyrrole type Pacman complexes can be parameterised using two parameters (ϕ and θ) as defined by Givaja *et. al.* (2007).[2] The twist angle, ϕ, is a measure of lateral slipping of the two macrocycle pockets; and the bite angle , θ, is a measure of the bite angle of the Pacman cleft (**Figure 5.7(a)** and **(b)**). The variation of these parameters with pressure is shown in **Figure 5.8**. In addition, the angles between the two pyrrole-based halves of the macrocyclic binding pockets for Cu1 and Cu2 are shown in **Figure 5.9**.

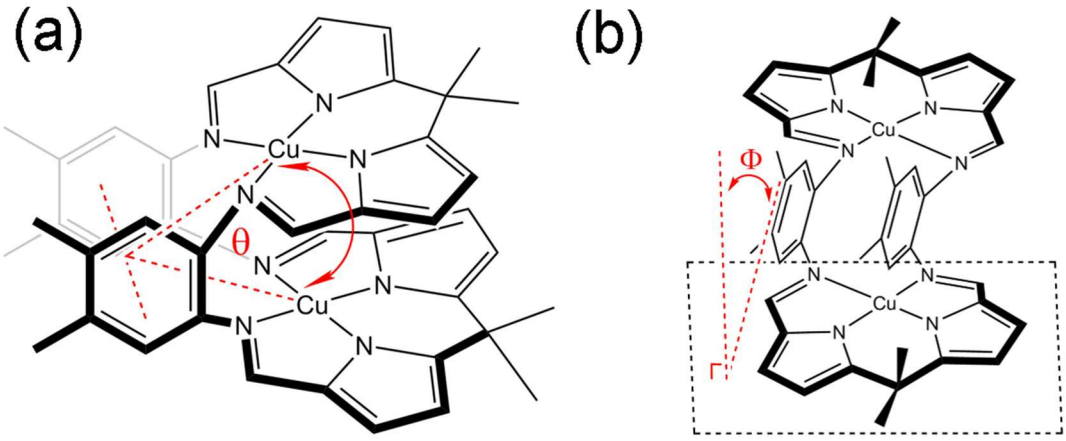

Figure 5.7 (**a**) the bite angle Θ and (**b**) the twist angle Φ. Figure adapted from Stevens et al.[4]

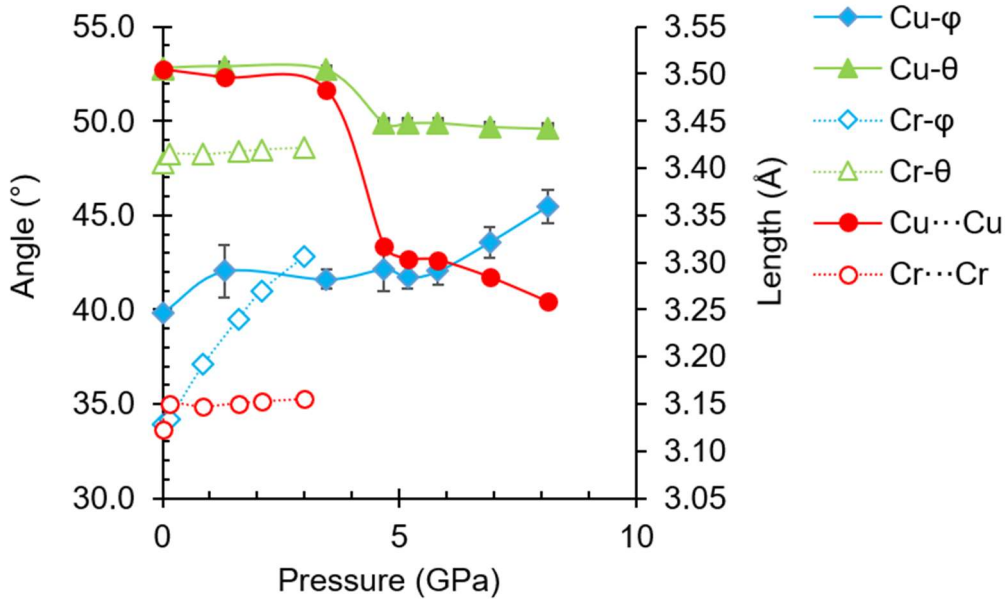

Figure 5.8 Variations of the structural parameters (ϕ=twist angle, θ=bite angle) of [Cu_2(L)] (filled markers) and [Cr_2(L)] (open markers) with pressure. [Cr2(L)] data taken from Stevens et.al (2016) are shown for comparison.[4]

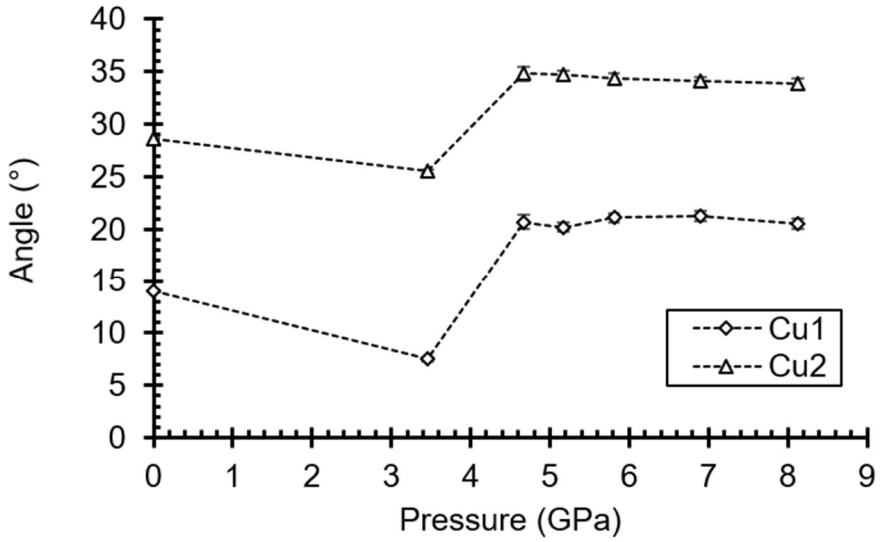

Figure 5.9 Variations in the angles between the macrocyclic pockets

As was the case for the related Cr pacman complex, the bite angle and metal-metal separation are quite unresponsive to pressure up to *ca.* 3.5 GPa. On increasing pressure to 4.67 GPa there is a sudden decrease in bite angle (θ) of *ca.* 3° decreasing the Cu(1)···Cu(2) separation distance abruptly from 3.4826(7) to 3.317(3) Å as the macrocycle cleft closes. The bite angle becomes relatively inflexible to further compression while the Cu separation distance continues to decrease steadily, adopting a value of 3.258(2) Å at 8.13 GPa.

Compression of $[Cr_2L]$ to 3.0 GPa led to an increase in the twist angle, ϕ, from 33.9 to 42.8°. In the Cu complex ϕ is rather insensitive to this pressure range, though it does begin to increase after the transition. More notable is that as the bite angle closes at 4.67 GPa, Ne3 is accommodated at the cleft by a 'butterfly wing' effect in the angle between the two halves of the macrocycles, the interplanar angle changing from 7.5(2) to 20.7(7)° about Cu1 and from 25.5(2) to 34.8(7)° about Cu2. Both angles remain steady on further compression.

The porosity of the crystal towards neon at 4.67 GPa is seen to be the result of a combination of a bite-angle reduction and a change in the planarity of the macrocyclic fragments.

5.4. Conclusions

In this chapter we have described the effect of compression of the pacman complex [Cu_2L] using neon as a hydrostatic medium leading to the formation of a neon-containing co-crystal. The effect of pressure on molecular materials is usually studied using hydrostatic media such as methanol-ethanol, pentane-isopentane or fluorinert, which are effective for the regime between 0 and 10 GPa. Noble gases are used for accessing pressures in excess of 10 GPa, but relatively little work had been carried out at such pressures on complex molecular systems using this technique. There is growing interest in the interplay of noble gases with molecular crystals, as demonstrated for example by very recent work on 4-hydroxycanobenzene where helium insertion led to two phase transitions.[36] In contrast with the present study, neon insertion was not observed.

The idea that porosity can be induced with pressure sounds somewhat counter-intuitive. Indeed, the effect of pressure on molecular solids has often been described in terms of compression of intermolecular void space, which naturally hinders guest inclusion. [Cu_2L] is, according to the usual criteria, a non-porous material under ambient conditions with no solvent accessible void space. Below 3.46 GPa the path of compression is essentially similar to other molecular materials, closing up interstitial voids and shortening intermolecular contacts. The pressure-induced porosity that occurs at 4.67 GPa is triggered by a change in the conformation of the pacman ligand that creates the space needed to incorporate neon.

The conformational flexibility of the pacman complex is an essential component in the mechanism of neon inclusion, a feature that is reminiscent of the gate-opening transition in the framework material ZIF-8 at 1.47 GPa which also led to an increase in guest inclusion.[34, 37-38] A related effect is responsible for the low bulk moduli [6.0(7) and 4.3(3) GPa] of the P and OP polymorphs of the 5-methyl-2-[(2-nitrophenyl)amino]-3-thiophenecarbonitrile), where conformational flexibility provides an additional means for a solid to accommodate pressure.[39-40]

Pacman complexes have been shown to activate water, dioxygen and carbon dioxide by incorporating these molecules into the cleft in close proximity to redox active metal centres. A particularly intriguing feature of the uptake of neon by $[Cu_2L]$ is the location of one neon atom (Ne3) in the vicinity of the pacman cleft. Incorporation of neon at this site is facilitated by the flexing of the copper-bound macrocycles, which is presumably a snapshot of the pathway through which small molecules approach the cleft during catalysis.

5.5. References

1. Devoille, A. M. J.; Love, J. B., Double-pillared cobalt Pacman complexes: synthesis, structures and oxygen reduction catalysis. *Dalton Transactions* **2012,** *41* (1), 65-72.

2. Givaja, G.; Volpe, M.; Leeland, J. W.; Edwards, M. A.; Young, T. K.; Darby, S. B.; Reid, S. D.; Blake, A. J.; Wilson, C.; Wolowska, J.; McInnes, E. J. L.; Schröder, M.; Love, J. B., Design and Synthesis of Binucleating Macrocyclic Clefts Derived from Schiff-Base Calixpyrroles. *Chemistry - A European Journal* **2007,** *13* (13), 3707-3723.

3. Pankhurst, J. R.; Curcio, M.; Sproules, S.; Lloyd-Jones, G. C.; Love, J. B., Earth-Abundant Mixed-Metal Catalysts for Hydrocarbon Oxygenation. *Inorganic Chemistry* **2018,** *57* (10), 5915-5928.

4. Stevens, C. J.; Prescimone, A.; Tuna, F.; McInnes, E. J. L.; Parsons, S.; Morrison, C. A.; Arnold, P. L.; Love, J. B., Inter- versus Intramolecular Structural Manipulation of a Dichromium(II) Pacman Complex through Pressure Variation. *Inorganic Chemistry* **2016,** *55* (1), 214-220.

5. McKellar, S. C.; Moggach, S. A., Structural studies of metal-organic frameworks under high pressure. *Acta Crystallographica Section B* **2015,** *71* (6), 587-607.

6. Guńka, P. A.; Dziubek, K. F.; Gładysiak, A.; Dranka, M.; Piechota, J.; Hanfland, M.; Katrusiak, A.; Zachara, J., Compressed Arsenolite As4O6 and Its Helium Clathrate As4O6·2He. *Crystal Growth & Design* **2015,** *15* (8), 3740-3745.

7. Klotz, S.; Chervin, J. C.; Munsch, P.; Marchand, G. L., Hydrostatic limits of 11 pressure transmitting media. *Journal of Physics D: Applied Physics* **2009,** *42* (7), 075413.

8. Collings, I. E.; Bykova, E.; Bykov, M.; Petitgirard, S.; Hanfland, M.; Paliwoda, D.; Dubrovinsky, L.; Dubrovinskaia, N., Neon-Bearing Ammonium Metal Formates: Formation and Behaviour under Pressure. *Chemical Physics and Physical Chemistry* **2016,** *17* (21), 3369-3372.

9. Wood, P. A.; Sarjeant, A. A.; Yakovenko, A. A.; Ward, S. C.; Groom, C. R., Capturing neon – the first experimental structure of neon trapped within a metal–organic environment. *Chemical Communications* **2016,** *52* (65), 10048-10051.

10. Thompson, A. C.; Padmore, H. A.; Oliver, A. G.; Teat, S. J.; Celestre, R. S.; Clark, S. M.; Domning, E. E.; Franck, K. D.; Morrison, G. Y., A Simple High Performance Beamline for Small Molecule Chemical Crystallography. *AIP Conference Proceedings* **2004,** *705* (1), 482-485.

11. Kunz, M.; MacDowell, A. A.; Caldwell, W. A.; Cambie, D.; Celestre, R. S.; Domning, E. E.; Duarte, R. M.; Gleason, A. E.; Glossinger, J. M.; Kelez, N.; Plate, D. W.; Yu, T.; Zaug, J. M.; Padmore, H. A.; Jeanloz, R.; Alivisatos, A. P.; Clark, S. M., A beamline for high-pressure studies at the Advanced Light Source with a superconducting bending magnet as the source. *Journal of Synchrotron Radiation* **2005,** *12* (5), 650-658.

12. Mao, H.; Xu, J.-A.; Bell, P., Calibration of the ruby pressure gauge to 800 kbar under quasi-hydrostatic conditions. *Journal of Geophysical Research: Solid Earth* **1986,** *91* (B5), 4673-4676.

13. *Apex 3, Bruker, Bruker AXS Inc., Madison, Wisconsin, USA*, 2017.

14. Tu, M.; Wiktor, C.; Rosler, C.; Fischer, R. A., Rapid room temperature syntheses of zeolitic-imidazolate framework (ZIF) nanocrystals. *Chemical Communications* **2014,** *50* (87), 13258-13260.

15. Parsons, S., ECLIPSE- Program for masking high-pressure diffraction images and conversion between CCD image formats. The University of Edinburgh. **2014**.

16. *SADABS, Bruker, Bruker AXS Inc., Madison, Wisconsin, USA*, 2014/15.

17. Sheldrick, G. M. *XPREP*, 2008/2; Bruker, Bruker AXS Inc.: Madison, Wisconsin, USA, 2008.

18. Sheldrick, G., SHELXT - Integrated space-group and crystal-structure determination. *Acta Crystallographica Section A* **2015,** *71* (1), 3-8.

19. Sheldrick, G., Crystal structure refinement with SHELXL. *Acta Crystallographica Section C* **2015,** *71* (1), 3-8.

20. Dolomanov, O. V.; Bourhis, L. J.; Gildea, R. J.; Howard, J. A. K.; Puschmann, H., OLEX2: a complete structure solution, refinement and analysis program. *Journal of Applied Crystallography* **2009,** *42* (2), 339-341.

21. Macrae, C. F.; Bruno, I. J.; Chisholm, J. A.; Edgington, P. R.; McCabe, P.; Pidcock, E.; Rodriguez-Monge, L.; Taylor, R.; van de Streek, J.; Wood, P. A., Mercury CSD 2.0 - new features for the visualization and investigation of crystal structures. *Journal of Applied Crystallography* **2008,** *41* (2), 466-470.

22. Gavezzotti, A., Calculation of lattice energies of organic crystals: The PIXEL integration method in comparison with more traditional methods. *Zeitschrift für Kristallographie* **2005,** *220*, 499-510.

23. Gavezzotti, A., Efficient computer modeling of organic materials. The atom–atom, Coulomb–London–Pauli (AA-CLP) model for intermolecular electrostatic-polarization, dispersion and repulsion energies. *New Journal of Chemistry* **2011,** *35* (7), 1360-1368.

24. Frisch, M. J.; Trucks, G. W.; Schlegel, H. B.; Scuseria, G. E.; Robb, M. A.; Cheeseman, J. R.; Scalmani, G.; Barone, V.; Petersson, G. A.; Nakatsuji, H.; Li, X.; Caricato, M.; Marenich, A.; Bloino, J.; Janesko, B. G.; Gomperts, R.; Mennucci, B.; Hratchian, H. P.; Ortiz, J. V.; Izmaylov, A. F.; Sonnenberg, J. L.; Williams-Young, D.; Ding, F.; Lipparini, F.; Egidi, F.; Goings, J.; Peng, B.; Petrone, A.; Henderson, T.; Ranasinghe, D.; Zakrzewski, V. G.; Gao, J.; Rega, N.; Zheng, G.; Liang, W.; Hada, M.; Ehara, M.; Toyota, K.; Fukuda, R.; Hasegawa, J.; Ishida, M.; Nakajima, T.; Honda, Y.; Kitao, O.; Nakai, H.; Vreven, T.; Throssell, K.; Jr., J. A. M.; Peralta, J. E.; Ogliaro, F.; Bearpark, M.; Heyd, J. J.; Brothers, E.; Kudin, K. N.; Staroverov, V. N.; Keith, T.; Kobayashi, R.; Normand, J.; Raghavachari, K.; Rendell, A.; Burant, J. C.; Iyengar, S. S.; Tomasi, J.; Cossi, M.; Millam, J. M.; Klene, M.; Adamo, C.; Cammi, R.; Ochterski, J. W.; Martin, R. L.; Morokuma, K.; Farkas, O.; Foresman, J. B.; Fox, D. J. *Gaussian 09, Revision E.01.*, Gaussian, Inc.: Wallingford CT, 2016.

25. Angel, R. J.; Alvaro, M.; Gonzalez-Platas, J., EosFit7c and a Fortran module (library) for equation of state calculations. *zkri* **2014,** *229* (5), 405.

26. Parsons, S. *STRAIN: Calculation of Strain Tensor*, 10; The University of Edinburgh, 2003.

27. Ohashi, Y.; Burnham, C. W., Clinopyroxene lattice deformations. Roles of chemical substitution and temperature. *American Mineralogist* **1973,** *58* (9-10), 843-849.

28. Bradenburg K., B. M. *DIAMOND Version 2.1. Crystal Impact GbR, Bonn, Germany*, 2001.

29. Spek, A., Structure validation in chemical crystallography. *Acta Crystallographica Section D* **2009,** *65* (2), 148-155.

30. Giordano, N.; Beavers, C. M.; Kamenev, K. V.; Marshall, W. G.; Moggach, S. A.; Patterson, S. D.; Teat, S. J.; Warren, J. E.; Wood, P. A.; Parsons, S., High-pressure polymorphism in l-threonine between ambient pressure and 22 GPa. *CrystEngComm* **2019**, *21* (30), 4444-4456.

31. Giordano, N.; Afanasjevs, S.; Beavers, C. M.; Hobday, C. L.; Kamenev, K. V.; O'Bannon, E. F.; Ruiz-Fuertes, J.; Teat, S. J.; Valiente, R.; Parsons, S., The Effect of Pressure on Halogen Bonding in 4-Iodobenzonitrile. *Molecules* **2019,** *24* (10), 2018.

32. Likhacheva, A. Y.; Rashchenko, S. V.; Chanyshev, A. D.; Inerbaev, T. M.; Litasov, K. D.; Kilin, D. S., Thermal equation of state of solid naphthalene to 13 GPa and 773 K: In situ X-ray diffraction study and first principles calculations. *The Journal of Chemical Physics* **2014,** *140* (16), 164508.

33. Funnell, N. P.; Dawson, A.; Marshall, W. G.; Parsons, S., Destabilisation of hydrogen bonding and the phase stability of aniline at high pressure. *CrystEngComm* **2013,** *15* (6), 1047-1060.

34. Hobday, C. L.; Woodall, C. H.; Lennox, M. J.; Frost, M.; Kamenev, K.; Düren, T.; Morrison, C. A.; Moggach, S. A., Understanding the adsorption process in ZIF-8 using high pressure crystallography and computational modelling. *Nature Communications* **2018,** *9* (1), 1429.

35. Hobday, C. L.; Marshall, R. J.; Murphie, C. F.; Sotelo, J.; Richards, T.; Allan, D. R.; Düren, T.; Coudert, F.-X.; Forgan, R. S.; Morrison, C. A.; Moggach, S. A.; Bennett, T. D., A Computational and Experimental Approach Linking Disorder, High-Pressure Behavior, and Mechanical Properties in UiO Frameworks. *Angewandte Chemie International Edition* **2016,** *55* (7), 2401-2405.

36. Collings, I. E.; Hanfland, M., Packing Rearrangements in 4-Hydroxycyanobenzene Under Pressure. *Molecules* **2019,** *24* (9), 1759.

37. Moggach, S. A.; Bennett, T. D.; Cheetham, A. K., The Effect of Pressure on ZIF-8: Increasing Pore Size with Pressure and the Formation of a High-Pressure Phase at 1.47 GPa. *Angewandte Chemie International Edition* **2009,** *48* (38), 7087-7089.

38. Fairen-Jimenez, D.; Moggach, S. A.; Wharmby, M. T.; Wright, P. A.; Parsons, S.; Düren, T., Opening the Gate: Framework Flexibility in ZIF-8 Explored by Experiments and Simulations. *Journal of the American Chemical Society* **2011,** *133* (23), 8900-8902.

39. Harty, E. L.; Ha, A. R.; Warren, M. R.; Thompson, A. L.; Allan, D. R.; Goodwin, A. L.; Funnell, N. P., Reversible piezochromism in a molecular wine-rack. *Chemical Communications* **2015,** *51* (53), 10608-10611.

40. Funnell, N. P.; Bull, C. L.; Ridley, C. J.; Capelli, S., Structural behaviour of OP-ROY at extreme conditions. *CrystEngComm* **2019,** *21* (30), 4473-4483.

Chapter 6

Concluding Remarks

6.1. Concluding Remarks

The general overarching theme of this thesis has been the compression of molecular crystals to pressure extremes. The underlying causes of phase transitions in these materials have been defined. Crystallographic work was supported by computational methods, which not only corroborates structural information at high-pressures but also rationalises any phase transitions in energetic terms.

The work on threonine in Chapter 2 is perhaps the most impactful result in this thesis, as the highest-pressure structure for any complex organic molecule at 22 GPa is reported. However, we expect this record to be surpassed as more studies combine experimental and computational approaches. The chapter supports and expands upon previous spectroscopic works to 27 GPa, while mechanisms of the three known phase transitions of threonine are proposed based on structural data. Our methodological approach to high-quality high-pressure sample loadings and data collection and validation of crystal structures by computational methods will hopefully set precedent in other structural studies as more extreme-pressure structures of amino acids, or other complex organic molecules are sought.

In Chapter 3 we expand on the studies of intermolecular interactions at high-pressure by investigating the halogen-bonding present in 4-iodobenzonitrile. 4-iodobenzonitrile undergoes a reconstructive phase transition driven by relief of strain in π···π contacts rather than by the minimisation of molar volume, as is seen in other phase transitions investigated in this thesis. This chapter represents the most technically challenging investigation as we turn to various crystal growth techniques to obtain diffraction quality single-crystals of the high-pressure phase that tended to degrade. We used rapid compression of an *in-situ* grown crystal to obtain diffraction data suitable for structure solution by simulated annealing. We

envisage that such techniques could be applied in the studies of other reconstructive phase transitions or difficult to obtain samples.

In Chapter 4 the crystal structure of pyridine III was conclusively determined for the first time by single-crystal X-ray diffraction. We propose a mechanism for the phase II to III transition by studying compression and decompression behaviour over phase boundaries by a range of experimental and computational techniques. The phase transitions are sluggish in nature and the boundary conditions still defy a precise definition. We present our work in the context of a comprehensive review of the literature and present compelling evidence for the unambiguous assignment of the high-pressure phases that hopefully others will adopt moving forward.

Chapter 5 is a short study on neon-intercalation in a Cu-Pacman macrocycle. The work is novel in that this is the first Pacman-neon co-crystal ever reported. Indeed, it is the first example of any intercalation in the solid-state of the pacman complexes. The study shows that pressure can induce porosity in a seemingly non-porous structure as the macrocyclic ligands flex to accommodate the neon pressure transmitting medium.

Synchrotron radiation sources and optimised high-pressure crystallography beamlines have been paramount in obtaining quality structural data in this thesis.